Mössbauer Spectroscopy of Linear Chain Systems

A thesis
submitted in partial fulfilment
of the requirements for the Degree
of
Doctor of Philosophy in Physics
in the
University of Canterbury
by
Nicholas I. Sheen

Department of Physics and Astronomy
University of Canterbury
1994

Abstract

Since the prediction by Villain in 1975 of moving magnetic domain walls (or solitons) in 1–dimensional Ising–like antiferromagnets, there has been interest in compounds with these properties. Mössbauer spectra of $CsCo_{0.99}Fe_{0.01}Cl_3$ in the magnetically ordered phases below $T_{N_1} = 21.2$ K were analysed by Ward *et al* (1987) assuming that only the two lowest energy electronic states of the $^{57}Fe^{2+}$ ion were significantly occupied (the 2–level relaxation model). This assumption is unreliable above approximately 18 K because it was estimated that the third lowest–lying electronic state of Fe^{2+} was significantly occupied at those temperatures. Nevertheless, it was found that two relaxation processes were present, one attributed to moving domain walls, and the other to transitions between the low–lying electronic states of the Fe^{2+} ion.

In this work the 2–level relaxation model was extended to include the third lowest–lying electronic state of the Fe^{2+} ion. A further extension, the combined relaxation model, enables Mössbauer spectra to be fitted when both 3–level electronic relaxation and relaxation due to moving domain walls occur with similar rates at the same $^{57}Fe^{2+}$ site. The quasi 1–dimensional Ising–like antiferromagnetic salt NH_4CoCl_3 doped with less than 1 atomic % $^{57}Fe^{2+}$ was synthesised, and Mössbauer spectra were taken at temperatures between 1.3 and 250 K. The Mössbauer spectra of both $CsCo_{1-x}Fe_xCl_3$ and $NH_4Co_{1-x}Fe_xCl_3$ in the magnetically ordered phases were analysed using the 2–level, 3–level and combined relaxation models. Although good fits to the Mössbauer spectra of $CsCo_{1-x}Fe_xCl_3$ and $NH_4Co_{1-x}Fe_xCl_3$ were obtained using all the relaxation models, the combined relaxation model was the most satisfactory since the assumptions of this model were not invalidated by the parameters obtained from the fits. The soliton relaxation rates obtained were much slower than those predicted theoretically and found from other experiments on $CsCoCl_3$.

One reason for this which is examined in this thesis is that the determined rates are unduly affected by the approximations made in the relaxation models. Another possible explanation of the discrepancy is that the presence of iron in the cobalt chains changes the soliton dynamics.

In order to study the effect of doping NH_4CoCl_3 with Fe^{2+}, the isomorphous crystal NH_4FeCl_3 was grown. The magnetic structure of NH_4FeCl_3 is expected to be governed by ferromagnetic intra–chain interactions and weaker antiferromagnetic inter–chain interactions. The linewidth broadening of the Mössbauer spectra of NH_4FeCl_3 at temperatures up to 10 K is evidence for the existence of magnetic correlations above the Néel temperature (1.7 K). The 4.2 and 1.3 K spectra show that a distribution of magnetic hyperfine fields B are present, possibly due to incommensurate magnetic ordering. At 4.2 K the main components of the Mössbauer spectrum are approximately 79 % with $B = 0$ and 21 % with $B = 5.32$ T. At 1.3 K the main components of the Mössbauer spectrum are approximately 72 % with $B = 5.2$ T and 28 % with $B = 0$. The non–magnetic subspectrum at 1.3 K may be caused by cancellation between the different components of the magnetic hyperfine field.

Contents

List of Tables

List of Figures

Chapter 1

Introduction

1.1 Solitons in $CsCo_{1-x}Fe_xCl_3$ and $NH_4Co_{1-x}Fe_xCl_3$.

Quasi 1–dimensional magnetic crystals provide model systems for the study of non–linear excitations. In a quantum theory describing Ising–like antiferromagnetic chains, Villain (1975) showed that the spin dynamics of these systems are dominated by moving domain walls. In this thesis these moving domain walls are felicitously referred to as solitons, although the link to true solitons (for example, large amplitude solutions to the sine–Gordon equation) has only been established for classical magnetic systems (Mikeska 1980).

In a review of soliton dynamics in magnetic chains, Boucher *et al* (1987) described 3 compounds; $CsNiF_3$, $(CH_3)_4NMnCl_3$ (TMMC) and $CsCoCl_3$. $CsNiF_3$ and TMMC are examples of XY–like compounds, whose spins lie perpendicular to the chain axis. The small single–ion anisotropy compared to the isotropic Heisenberg exchange, and the high spin (S=1 for $CsNiF_3$ and S=5/2 for TMMC) of the magnetic ion in these compounds means that the solitons are approximately 10 to 30 spins wide and can be considered as classical solitons with continuously varying spin. The prediction by Mikeska (1978) of sine–Gordon solitons in $CsNiF_3$ was verified by Kjems and Steiner (1978) using neutron inelastic scattering (NIS). Solitons in TMMC were detected by Boucher and Renard (1980) using nuclear spin–lattice relaxation of ^{15}N, and a quantitative analysis was made by Boucher *et al* (1982) using NIS. Because of its high spin and the values of its exchange constants, TMMC has emerged as the preferred 1–dimensional XY–like antiferromagnet for the study of sine–Gordon

solitons.

$CsCoCl_3$ is a good example of a 1–dimensional Ising–like antiferromagnet, with the easy axis along the chain direction and spin S=1/2. In this compound the soliton is "narrow", extending over just 1 lattice spacing, and is described by the quantum theory of Villain (1975). The presence of solitons in $CsCoCl_3$ was verified using NIS by Boucher *et al* (1985). Other experimental work on $CsCoCl_3$ has been performed using magnetic susceptibility (Achiwa 1969), neutron diffraction (Mekata and Adachi 1978), ^{133}Cs nuclear magnetic resonance (Adachi *et al* 1979), and optical birefringence (Iio *et al* 1980). The Mössbauer research group at Canterbury University has studied $CsCo_{0.99}Fe_{0.01}Cl_3$ by Mössbauer spectroscopy (Ward *et al* 1987). The aim of this research is to enable reliable determination of soliton relaxation rates from the Mössbauer spectra of $CsCo_{1-x}Fe_xCl_3$ and $NH_4Co_{1-x}Fe_xCl_3$.

Mössbauer spectroscopy has also been used to study a variety of 1–dimensional systems, several of which are given in a review by Johnson (1984).

The crystal structure of $CsCoCl_3$ is perovskite, consisting of chains of trigonally distorted $CoCl_6^{4-}$ octahedra in a triangular lattice separated by the large Cs^+ ions, as shown in figures 1.1 and 1.2. The space group is $P6_3/mmc$, with lattice parameters $a = (7.2019 \pm 0.0004)$ Å and $c = (6.0315 \pm 0.0005)$ Å (Soling 1968).

There are two main exchange interactions present between the Co^{2+} ions in $CsCoCl_3$. One is the antiferromagnetic superexchange interaction via an intervening Cl^- ion between two nearest Co^{2+} neighbours within the chain, with exchange constant J. The other is the antiferromagnetic superexchange interaction between Co^{2+} ions on neighbouring chains, with exchange constant J', which is much less than J because the superexchange bridge for J' involves two Cl^- ions. From a Raman experiment, J'=0.45 to 0.89 K depending on the analysis (Shiba 1980, Lehmann *et al* 1981). Another value of J'=1.44 K can be found from neutron diffraction (Nagler *et al* 1983) and magnetic susceptibility measurements (Mekata *et al* 1987), while the electron paramagnetic resonance work of Ohta *et al* (1993) suggests that J' may be as high as 1.7 K.

In paramagnetic $CsCoCl_3$, the ground state of the Co^{2+} ions in the trigonally distorted cubic crystal field is a Kramers doublet (Euler and Garrett 1981). Within the chains, the nearest neighbour Co^{2+} spins interact according to the effective

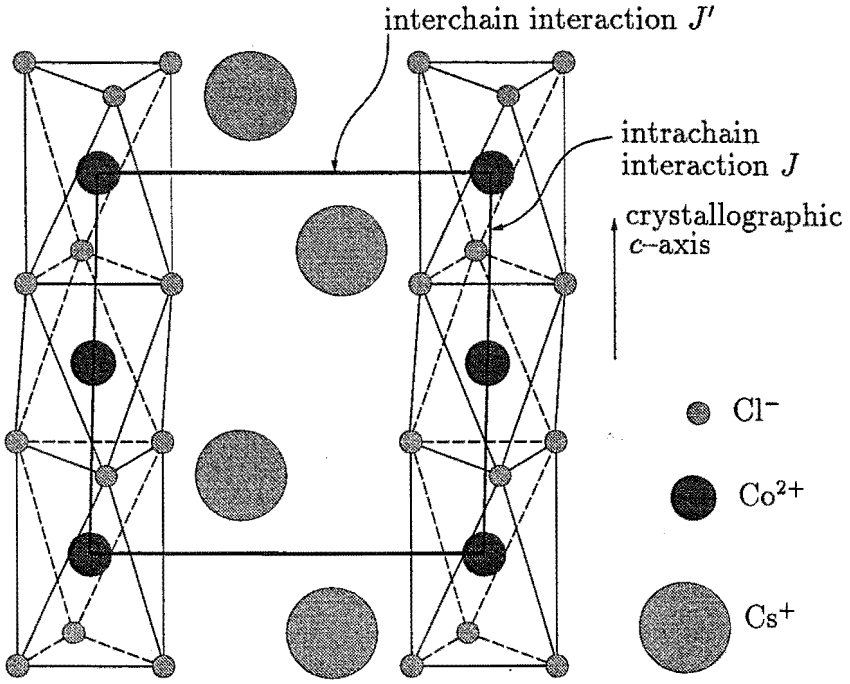

Figure 1.1: A diagram of the crystal structure of $CsCoCl_3$ showing the chains of trigonally distorted $CoCl_6^{4-}$ octahedra.

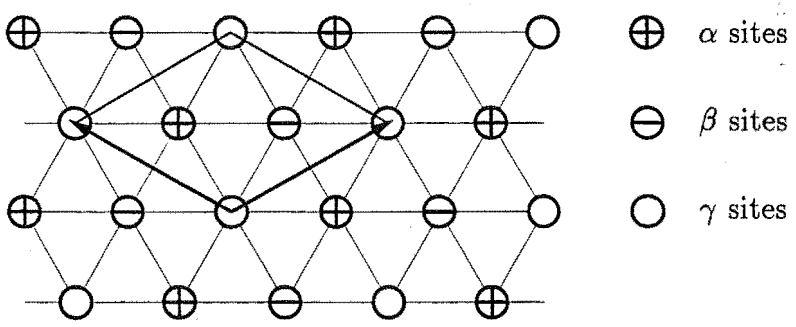

Figure 1.2: A diagram of the triangular spin structure of the Co^{2+} ions perpendicular to the crystallographic c axis. The a and b axes of the magnetic unit cell are depicted by the bold arrows. The α sites are all spin up (or down), and the β sites have the opposite spin to the α sites. Above T_{N_2} the γ sites are uncorrelated with each other. Below T_{N_2} they are all spin up (or down).

$S = 1/2$ Hamiltonian

$$\mathcal{H} = 2J \sum_i [S_i^z S_{i+1}^z + \varepsilon(S_i^x S_{i+1}^x + S_i^y S_{i+1}^y)] \tag{1.1}$$

where the sum is over the spins i within the chain. J and ε have been determined to be 75 K and 0.12 respectively (Achiwa 1969, Tellenbach 1978, and Yoshizawa *et al* 1981). The positive sign of J in this Hamiltonian signifies that the intra-chain exchange interaction is antiferromagnetic. The low value of ε means that the Hamiltonian is Ising–like, and so has soliton solutions as shown by Villain. These solutions are ordered domains separated by domain walls which move at constant velocity until they meet another domain wall.

Within the effective $S = 1/2$ Hamiltonian (1.1) a soliton can be thought of in a semi–classical model as "flipping the spin" of successive spins along the chain of Co^{2+} ions. This is illustrated in figure 1.3. After the passage of a soliton, a

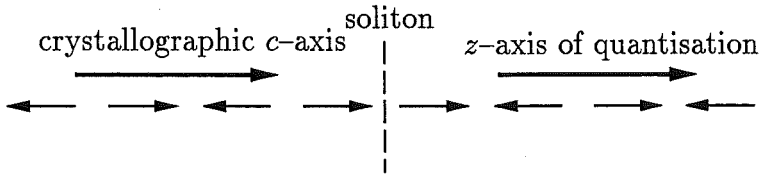

Figure 1.3: A diagram of a chain of Co^{2+} spins in $CsCoCl_3$ or NH_4CoCl_3.

spin in the chain experiences an intra–chain exchange with its neighbours which is exactly the same as if the direction of the z–axis had been reversed. Due to energy considerations the Co^{2+} ion must be in the ground state in this new environment, and so the signs of the z components of $\boldsymbol{L}$ and $\boldsymbol{S}$ are reversed. Hence the only effect on the Co^{2+} ion of the passage of a soliton is an effective reversal of the z axis of quantisation, and the soliton is a "topological" excitation.

Due to the large ratio of the intra to inter–chain exchange interactions, short–range antiferromagnetic order along the chains of Co^{2+} spins develops before the onset of 3–dimensional ordering. In $CsCoCl_3$ the transition from paramagnetism to short–range order occurs at $\approx$75 K (Boucher *et al* 1985). Below 75 K the intrachain correlation length gradually increases until the transition to the partially disordered phase at T_{N_1} is reached. Three measurements (Melamud *et al* 1974, Mekata and

Adachi 1978, and Yoshizawa and Hirakawa 1979) of the first Néel temperature can be combined to give T_{N_1}=21.2 K.

In the partially disordered phase below T_{N_1} the Co^{2+} ions are arranged in a triangular lattice within the $a-b$ plane. No consistent arrangement of the spins can be found in which each spin has anti-parallel nearest neighbours. The spin configuration which minimises the antiferromagnetic interchain exchange energy is shown in figure 1.2. In this configuration the chains of spins marked γ are frustrated, with each spin interacting with an equal number of spin up and spin down nearest interchain neighbours. The complete interactions of the spins in the frustrated chains are thus well approximated by the nearest neighbour Hamiltonian of equation (1.1). It follows from the work of Villain that solitons as described above are expected in the frustrated chains.

At temperatures below $T_{N_2} \simeq 8-9$ K (Mekata and Adachi 1978, Yoshizawa and Hirakawa 1979) the second nearest neighbour inter–chain exchange interaction is important, and full 3–dimensional ferrimagnetic ordering occurs. In this phase all spins in the frustrated chains are ferromagnetically correlated with the second nearest interchain neighbours (the nearest frustrated chains).

The range of temperatures over which the soliton dynamics may be followed can be extended by studying NH_4CoCl_3. $NH_4Co_{1-x}Fe_xCl_3$ is particularly suitable for study by Mössbauer spectroscopy because the low atomic mass of the NH_4^+ ion results in minimal scattering of the Mössbauer gamma–rays, allowing good quality spectra to be collected quickly. The crystal structure of NH_4CoCl_3 is very similar to that of $CsCoCl_3$, with the large NH_4^+ ion acting as a spacer between a triangular arrangement of trigonally distorted $CoCl_6^{4-}$ octahedra. At 25 °C NH_4CoCl_3 has the same space group as $CsCoCl_3$, with lattice parameters $a = (6.967 \pm 0.001)$ Å and $c = (6.010 \pm 0.001)$ Å (Swanson *et al* 1968).

NH_4CoCl_3 and $CsCoCl_3$ have similar crystal structures and bond angles within the chains, and so these salts are expected to have the same magnetic phases. The smaller lattice parameter a of NH_4CoCl_3 is expected to result in a slightly stronger interchain exchange interaction in NH_4CoCl_3 than in $CsCoCl_3$. T_{N_1} for NH_4CoCl_3 is found approximately from the Mössbauer spectra taken by Asch *et al* (1973), and from the work in this thesis to be (27 ± 4) K. This value is higher than T_{N_1} of $CsCoCl_3$, as expected in the presence of stronger interchain exchange interactions

in the NH_4CoCl_3 salt. By the same reasoning, the second Néel temperature T_{N_2} for NH_4CoCl_3 is also expected to be larger than that of $CsCoCl_3$. From this thesis, $T_{N_2} \simeq (11 \pm 2)$ K.

To enable ^{57}Fe Mössbauer spectra to be taken of $CsCoCl_3$ and NH_4CoCl_3, these crystals were grown with a low concentration (less than 1 atomic %) of ^{57}Fe dopant. It was hoped that the $^{57}Fe^{2+}$ ion probes do not significantly interfere with the magnetic ordering or soliton dynamics in these salts. It has been reported by Elmassalami *et al* (1989) in a Mössbauer study of solitons in the anisotropic Ising–like ferromagnet $M_xFe_{1-x}Cl_2(NC_5H_5)_2$ where M = Fe, Cd, or Mn, that the magnetic Mn^{2+} ions participate in the magnetic ordering of the chains, and do not alter the soliton dynamics, while doping with non–magnetic Cd^{2+} increases the number of free chain ends, and hence alters the soliton dynamics.

It is assumed that the soliton passes unimpeded past the Fe^{2+} ion in the chain of frustrated Co^{2+} spins. Under this assumption the effect of the passage of the soliton on the Fe^{2+} ion is to reverse the exchange field which the Fe^{2+} ion experiences with its nearest neighbours. Since the soliton passes unimpeded, the occupation of the initial and final electronic energy levels of the Fe^{2+} ion must be the same. By the same argument as for the Co^{2+} ions, the final exchange field is the reverse of the initial exchange field, so the axis of quantisation of the Fe^{2+} ion is reversed.

In their study of the Mössbauer spectra of $CsCo_{1-x}Fe_xCl_3$, Ward *et al* (1987) observed slow (0.5 to 40 MHz) paramagnetic relaxation between the lowest 2 electronic states of Fe^{2+} in the α and β sites (see figure 1.2) at temperatures between T_{N_2} and T_{N_1}, as well as in the γ sites at temperatures below T_{N_2} in the magnetically ordered host $CsCoCl_3$. This relaxation was reported to be thermally activated with an activation energy of (42 ± 8) K, much lower than the activation energy of 75 K reported for solitons in pure $CsCoCl_3$ by Boucher *et al* (1985). It appears that the "electronic" relaxation in the Fe^{2+} ion dopant is similar to that of a paramagnetic ion in a magnetically dilute crystal, caused by interactions between the ion and the phonon bath. It is unusual to observe slow paramagnetic relaxation in the Mössbauer spectra of a magnetically ordered crystal. This unusual relaxation is presumably associated with the intra–chain Fe–Co exchange interaction being weaker than the interaction of one chain of Co^{2+} spins with its neighbours. In this case 3–dimensional order may occur between chains while the Fe^{2+} ion exhibits relaxation,

as observed in the Mössbauer spectra taken by Ward *et al* (1987).

Because the magnetic exchange interactions of $CsCoCl_3$ and NH_4CoCl_3 are expected to be similar, the Mössbauer spectra of $NH_4Co_{1-x}Fe_xCl_3$ are also expected to exhibit electronic relaxation. In order to study some of the effects of doping NH_4CoCl_3 with Fe^{2+}, a crystal of pure NH_4FeCl_3 was grown. If Fe^{2+} substituted unevenly into NH_4CoCl_3, the $^{57}Fe^{2+}$ ions with Fe^{2+} nearest neighbours may be expected to exhibit similar Mössbauer spectra to those of pure NH_4FeCl_3.

Above 400 K NH_4FeCl_3 has the same crystal structure as NH_4CoCl_3 ($P6_3/mmc$). Two structural phase changes to lower symmetry occur in NH_4FeCl_3 at 400 K and in the range 10 K to 30 K (Visser and Harrison 1992, and Harrison 1993). In the distorted structures the Fe^{2+} ions are not equivalent so the structural changes may be observable by Mössbauer spectroscopy, although the structural phase change at (90±10) K was not observed in the Mössbauer spectra of NH_4FeBr_3 (Snodgrass 1993). Presumably this structural phase change in NH_4FeBr_3 does not alter the local environment of the Fe^{2+} ions sufficiently to be observed in the Mössbauer spectra.

NH_4FeCl_3 becomes magnetically ordered at (1.7 ± 0.2) K (Visser and Harrison 1992). Its magnetic structure has yet to be determined, but is expected to be similar to that of $RbFeCl_3$, due to the similar size of Rb^+ and NH_4^+, and the similar bond angles within the chains along the hexagonal c–axis. For $RbFeCl_3$, the exchange interactions between the Fe^{2+} ions within the chains are ferromagnetic, and are much stronger than the antiferromagnetic interchain interactions (Eibschutz *et al* 1975).

Within the planes perpendicular to the c–axis (the basal plane) the antiferromagnetically coupled spins of Fe^{2+} ions in $RbFeCl_3$ are arranged in a triangular lattice structure. This arrangement leads to frustration in the magnetic order of $RbFeCl_3$, where no consistent arrangement can be found in which all neighbouring spins are aligned antiferromagnetically. In $RbFeCl_3$ competition between the interchain dipole–dipole and exchange interactions leads to several magnetic phases at low temperature (Shiba 1982). Two incommensurate phases occur with transition temperatures of 2.5 K and 2.35 K, and a transition to commensurate 120° antiferromagnetic order in the basal plane occurs at 1.95 K (Wada *et al* 1982).

In previous work (Asch *et al* 1973) the Mössbauer spectra of NH_4FeCl_3 were recorded at 4.2 K and above 77 K. For this thesis the Mössbauer spectra of NH_4FeCl_3

have been recorded between 1.3 K and 250 K to investigate the low temperature structural and magnetic phase changes, and to enable comparison with the Mössbauer spectra of $NH_4Co_{1-x}Fe_xCl_3$.

1.2 Mössbauer Spectroscopy

The emission or absorption of gamma–rays without loss of energy due to the creation (or annihilation) of phonons is known as the Mössbauer effect. "Recoilless" (or zero phonon) emission and absorption allows the emitted gamma–ray produced from a nuclear transition between two states to be absorbed by a transition between the same two states. Wertheim (1964) is a concise introductory text to the Mössbauer effect. A more detailed account is given in Greenwood and Gibb (1971).

In crystals a significant fraction of the gamma–ray emissions and absorptions are recoilless. The recoil–free fraction f is related to the energy of the emitted (or absorbed) gamma–ray, E_γ, by

$$f = \exp\left[\frac{-E_\gamma^2 < x^2 >}{(\hbar c)^2}\right]$$

where $< x^2 >$ is the mean square vibrational amplitude of the emitting (absorbing) nucleus in the direction of the gamma–ray wave–vector (Greenwood and Gibb 1971). Thus f is greatest for low energy gamma–rays, and for small $< x^2 >$, which decreases for firmly bound atoms at low temperature.

The absence of phonon broadening means that the linewidth of the recoilless emission or absorption profile is caused by the uncertainty in the energy of the excited state, due to the Heisenberg uncertainty principle. For a transition from an excited state to the ground state, the full width of the emission profile at half maximum intensity is

$$\Gamma = \hbar/\tau_N \tag{1.2}$$

where τ_N is the mean lifetime of the excited state. For the 14.36 keV ^{57}Fe gamma–ray, τ_N=143 ns (*Mössbauer Effect Data Index* 1976), and so $\Gamma = 4.7 \times 10^{-9}$ eV. This near monochromaticity of the Mössbauer effect gamma–ray makes it possible to use Mössbauer spectroscopy to observe subtle changes in the chemical and magnetic environment of the absorbing nucleus.

In performing transmission Mössbauer spectroscopy, the source atoms are substituted into a rigid matrix which is chosen so that the source emits a single line. The excited and ground states of the absorber are split and shifted relative to the source states by the interaction of the nuclear charge and magnetic moment with the surrounding electro-magnetostatic potential. The energy of the emitted gamma–ray from the source is Doppler shifted according to

$$E(v) - E_\gamma = E_\gamma v/c$$

where v is the velocity imparted to the source by the spectrometer drive, c is the speed of light, and $E(v)$ is the energy of the Doppler shifted gamma–ray. A Mössbauer spectrum can be collected by scanning with the source velocity, and recording the change in count–rate as the source gamma–rays move in and out of resonance with the nuclear transitions in the absorber. The natural units of energy for the Mössbauer spectrum are the source velocity. Thus for ^{57}Fe, the Heisenberg limit of the source linewidth is, from equation (1.2),

$$\begin{aligned} v &= \Gamma c/E_\gamma \\ &= 4.6 \times 10^{-9} \text{ eV} \times 3 \times 10^{11} \text{ mm s}^{-1}/14.36 \times 10^{3} \text{ eV} \\ &= 0.096 \text{ mm s}^{-1} . \end{aligned}$$

In this laboratory typical ranges of energy accessible by Mössbauer spectroscopy are ± 10 mm s^{-1}, with a precision of approximately ± 0.01 mm s^{-1} at best.

The Hamiltonian describing the energy of the nucleus may be written as (Blatt and Weisskopf 1952, Jackson 1969)

$$\mathcal{H} = \mathcal{H}_0 + \mathcal{H}_{\text{IS}} + \mathcal{H}_{\text{QS}} + \mathcal{H}_{\text{M}} . \tag{1.3}$$

$\mathcal{H}_0$ represents all interactions other than the hyperfine interactions of the nucleus with the nuclear environment. The main contribution to $\mathcal{H}_0$ arises from intra–nuclear forces, giving rise to quantised nuclear states with nuclear spin quantum number I. In ^{57}Fe, the separation of the I=1/2 ground state from the I=3/2 first excited state is 14.36 keV (*Mössbauer Effect Data Index* 1976).

$\mathcal{H}_{\text{IS}}$ describes the electric monopole interaction of the nuclear charge with the electrostatic potential produced by the chemical environment of the absorbing atom. The resultant shift in the absorption lines of the Mössbauer spectrum is called the

isomer shift (IS). Generally, the chemical environment of the absorbing atom is different from that of a reference, so the s electron density at the nucleus will be different, and hence the absorber will have a different IS. $\mathcal{H}_{\rm IS}$ does not result in splitting of the nuclear substates, and is not affected by the passage of a soliton, or by electronic relaxation, and so $\mathcal{H}_{\rm IS}$ is of little interest in this work.

$\mathcal{H}_{\rm QS}$ refers to the interaction of a non–spherical nuclear charge with the electric field gradient (EFG) tensor. The components of the EFG tensor are

$$\nabla_i E_j = -V_{ij} = -\frac{\partial^2 V}{\partial x_i \partial x_j}$$

where V is the electrostatic potential at the nucleus. By suitable choice of the nuclear axes, V_{ij} may be reduced to a diagonal tensor, with V_{zz} the largest component. The charge density of the s electrons at the nucleus of the ^{57}Fe atom is non–zero, but is spherically symmetric, and so does not contribute to $\mathcal{H}_{\rm QS}$. Excluding the s electrons, the charge density at the nucleus is zero. In this case the Laplace equation requires that

$$V_{zz} + V_{yy} + V_{xx} = 0\,,$$

so the EFG is completely specified by two parameters, the principal component $-V_{zz}$, and the asymmetry parameter η where η is defined by

$$\eta = \frac{V_{xx} - V_{yy}}{V_{zz}}$$

with $|V_{zz}| > |V_{yy}| \geq |V_{xx}|$.

Symmetry considerations may further reduce the number of parameters needed to specify the EFG. A 3–fold rotation axis, as in the case of Fe^{2+} in $CsCo_{1-x}Fe_xCl_3$ and $NH_4Co_{1-x}Fe_xCl_3$, is sufficient to ensure that η=0.

The nuclear states with spin $I > 1/2$ are non–spherical, and so the substates with I=3/2 are affected by $\mathcal{H}_{\rm QS}$. For the m_I=3/2 substate, the nuclear quadrupole moment Q is defined as (Blatt and Weisskopf 1952)

$$|e|Q = \int r^2(3\cos^2\theta - 1)\rho(\boldsymbol{r})\mathrm{d}\tau$$

where e is the electronic charge, $\rho(\boldsymbol{r})$ is the charge density in the volume element $\mathrm{d}\tau$, which is at a distance r from the centre of the nucleus, and has an included angle θ relative to the nuclear quantisation axis. The value of Q is assumed to be 0.21×10^{-28} m^2 (Davidson *et al* 1973).

With the above definition of Q, and taking into account the axis and symmetry considerations above, Greenwood and Gibb (1971 p55) give

$$\mathcal{H}_{\rm QS} = \frac{|e|QV_{zz}}{4I(2I-1)}[3I_z^2 - \boldsymbol{I}^2] \tag{1.4}$$

where I_z and $\boldsymbol{I}^2$ are the conventional spin operators. For the nuclear state I=3/2, equation (1.4) has eigenvalues

$$E(\pm\tfrac{1}{2}) = -|e|QV_{zz}/4$$
$$\text{and} \quad E(\pm\tfrac{3}{2}) = |e|QV_{zz}/4$$

for the nuclear substates $m_I = \pm\frac{1}{2}$ and $\pm\frac{3}{2}$. The effect of $\mathcal{H}_{\rm QS}$ on the nuclear energy levels is shown in figure 1.4 for the case of $V_{zz} < 0$.

The quadrupole splitting observed in a Mössbauer spectrum is the difference in energy between transitions to the $m_I = \pm\frac{1}{2}$ substates and transitions to the $m_I = \pm\frac{3}{2}$ substates, and is thus

$$\text{QS} = \tfrac{1}{2}|e|QV_{zz}\,. \tag{1.5}$$

V_{zz} is thus inferred from measurements of the splitting QS.

The sole dependence on I_z of $\mathcal{H}_{\rm QS}$ in equation (1.4) is through the term I_z^2. Therefore $\mathcal{H}_{\rm QS}$, and hence QS, is unaffected by the passage of solitons.

The $\mathcal{H}_{\rm M}$ term in equation (1.3) refers to the magnetic dipole interaction of the nuclear spin with the magnetic field at the nucleus $\boldsymbol{B}$,

$$\mathcal{H}_{\rm M} = -g_I\mu_{\rm N}\boldsymbol{I}.\boldsymbol{B}\,.$$

Here $\mu_{\rm N} = e\hbar/(2m_{\rm p})$ is the nuclear magneton with $m_{\rm p}$ the proton mass, and g_I is the nuclear g factor. The Mössbauer Effect Data Index (1976) gives the ground state g factor as (0.18121 ± 0.00002) and the excited state g factor (-0.103541 ± 0.000003).

A diagram of the nuclear energy levels split by the magnetic dipole interaction is shown in figure 1.4.

When external magnetic fields are absent, $\boldsymbol{B}$ is just the magnetic hyperfine field $\boldsymbol{B}_{\rm hf}$. As discussed on page 6, for Fe^{2+} ions in frustrated chains the passage of a soliton is expected to reverse the axis of quantisation. The magnetic hyperfine field produced by the three lowest states of Fe^{2+} in $CsCo_{1-x}Fe_xCl_3$ and $NH_4Co_{1-x}Fe_xCl_3$ is proportional to $< \boldsymbol{S} >$ and $< \boldsymbol{L} >$ (see section 3.5) where $< O >$ refers to the

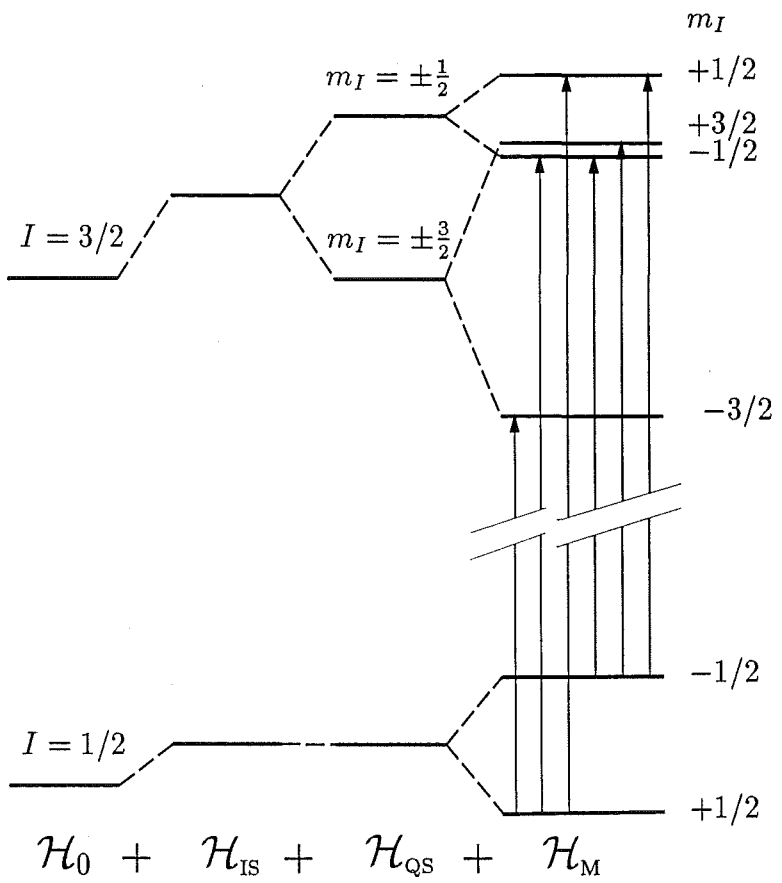

Figure 1.4: The influence of the different terms of Hamiltonian (1.3) on the nuclear energy levels of ^{57}Fe. The hyperfine splitting of the final m_I substates is drawn approximately to scale for $^{57}Fe^{2+}$ in $CsCo_{1-x}Fe_xCl_3$ and $NH_4Co_{1-x}Fe_xCl_3$.

expectation value of operator O. $\boldsymbol{B}_{\rm hf}$ is parallel to the z–axis (Ward *et al* 1987 and this work), and so its sign is reversed when a soliton passes the Fe^{2+} ion.

$\boldsymbol{B}_{\rm hf}$ also changes when relaxation occurs between the electronic states of Fe^{2+} (Ward *et al* (1987) and this work). If the time–scales for these two relaxation processes are of the right magnitude then their influence on the Mössbauer spectrum can be used to determine their relaxation rates.

1.3 Time Scales and Relaxation in Mössbauer Spectra of $CsCo_{1-x}Fe_xCl_3$ and $NH_4Co_{1-x}Fe_xCl_3$.

According to the Heisenberg uncertainty principle, if a system has 2 states of energy E_n and E_m, then the minimum time necessary to distinguish which state is occupied is given by

$$\tau_L \simeq \frac{\hbar}{E_n - E_m} .$$

In a Mössbauer spectrum exhibiting splitting between the absorption lines of energy $E_n = \hbar\omega_n$ and $E_m = \hbar\omega_m$, the time taken to resolve the different energies is

$$\tau_L \simeq (\omega_n - \omega_m)^{-1} .$$

τ_L is commonly referred to as the "Larmor precession time".

The hyperfine structure in a Mössbauer spectrum will be resolvable if at least one Larmor precession time occurs within the mean nuclear excited state life–time τ_N, that is, $\tau_L \lesssim \tau_N \simeq 143$ ns. This amounts to the intuitively obvious requirement that the energy separation of E_n and E_m be at least as large as the Mössbauer linewidth (the uncertainty in E_n and E_m).

A third time-scale is that of the mean life–time of the relaxing nuclear environment τ_R. Two examples of these relaxation processes are soliton and electronic relaxation as mentioned on page 12. If τ_R is very short compared to τ_L, as for spin waves, then the nucleus experiences the time average of the energies of the nuclear states. This effect always results in a reduction of the hyperfine splitting and structure of the Mössbauer spectrum. For slow relaxation τ_R is very long compared to τ_L. In this case the Mössbauer spectrum obtained is a superposition of two (or more) subspectra, each corresponding to one of the nuclear environments.

If the nuclear environment changes at a rate comparable to τ_L, then the nucleus senses a variety of hyperfine fields, and the Mössbauer spectrum will exhibit broadened lines. In this case τ_R can usually be found by fitting the broadened lineshape using the model of Blume and Tjon (1968). Typically τ_R may be determined if it is in the range $0.1\tau_L \lesssim \tau_R \lesssim 10\tau_L$.

An interesting feature of a magnetically split spectrum is that for a given τ_R a number of Larmor precession times may apply, due to the different splittings in the Mössbauer spectrum. This usually results in unequal broadening of the absorption

lines. For example, τ_R may be fast compared to one of the Larmor precession times, resulting in sharp lines, and of the order of one of the other Larmor precession times, resulting in broadened lines. This is a desirable feature which enables the life–time of the nuclear environment to be resolved over a large range. The exact range depends upon the details of the splitting of the Mössbauer spectrum. Typically the relaxation rate $R = \tau_R^{-1}$ may be determined in the range $0.1 \lesssim R \lesssim 1000$ MHz.

The frequency window of the Mössbauer effect extends the range of experimentally observable relaxation rates. The frequency window probed by NIS is above 1000 MHz. Boucher *et al* (1985) have performed exhaustive neutron scattering experiments on $CsCoCl_3$, and found the soliton relaxation rate near the lower extreme of their frequency window. This is the main reason for the interest in using the technique of Mössbauer spectroscopy to measure soliton relaxation rates in $CsCo_{1-x}Fe_xCl_3$. Mössbauer spectroscopy is also another measurement tool which can be used to probe soliton dynamics, and so offers an independent test of the theory of Villain (1975) applied to quasi 1–dimensional Ising–like antiferromagnets.

Ward *et al* (1987) developed the 2–level relaxation model for their analysis of the Mössbauer spectra of $CsCo_{1-x}Fe_xCl_3$. In this model it was assumed that only the two lowest electronic states of Fe^{2+} were occupied significantly, and that in the chains of frustrated spins the Mössbauer spectrum was dominated by soliton relaxation. The soliton relaxation rate that they obtained was much lower than expected from the results of Boucher *et al* (1985). Also, there were some features of the results they obtained which were not consistent with the model, namely:

- The soliton relaxation rate in the frustrated chains was not significantly faster than the Fe^{2+} electronic relaxation rate obtained from the subspectrum corresponding to the 3–dimensionally ordered chains. This is contrary to the assumption of the model that in the chains of frustrated spins the relaxation is dominated by solitons.

- From fits to the Mössbauer spectra taken below T_{N_1}, the magnetic hyperfine field B_{hf} decreased with increasing temperature, in contrast with the prediction that the B_{hf} which the lowest magnetic state of Fe^{2+} produces should be independent of temperature.

- According to preliminary calculations, the electronic energy levels of the Fe^{2+}

ion in $CsCo_{1-x}Fe_xCl_3$ are such that the third electronic state is significantly populated at temperatures above 14.6 K.

The departure from the 2–level relaxation model due to thermal occupation of the third electronic state of Fe^{2+} was expected to be greater in $NH_4Co_{1-x}Fe_xCl_3$, which has a higher T_{N_1}. In order to account for the occupation of the third electronic state the 3–level relaxation model was developed. In the 3–level relaxation model the electronic relaxation evident in the Mössbauer spectra was assumed to occur by the direct relaxation process, as for paramagnetic relaxation.

A further refinement is that of the combined relaxation model. This model was developed to calculate Mössbauer lineshapes when two different relaxation processes occur at the same site, and is suitable for calculating Mössbauer spectra of $^{57}Fe^{2+}$ ions in the frustrated chains of $CsCo_{1-x}Fe_xCl_3$ and $NH_4Co_{1-x}Fe_xCl_3$, where both soliton and electronic relaxation occur.

1.4 Thesis Overview

In chapter 2 details are given of the Mössbauer spectrometer, data analysis methods, cryogenics, and the steps taken to minimise vibrational broadening of the spectral lines. The methods of preparing $NH_4Co_{1-x}Fe_xCl_3$ and NH_4FeCl_3 crystals and absorbers are given, along with the results of X–ray diffraction of NH_4FeCl_3 and chemical analysis of the $NH_4Co_{1-x}Fe_xCl_3$ crystals and absorbers to accurately determine the concentration of the Fe^{2+} dopant.

The first section of the theory chapter is a review of the relaxation theory for Mössbauer spectroscopy based on the work of Blume and Tjon (1968), Abragam (1961), and Blume (1968). The original 2–level relaxation model of Ward *et al* (1987) is given in section 3.2. This model is extended in section 3.3 to the 3–level relaxation model. In this section the approximation that the direct process relaxation rate parameter is independent of which states are involved in electronic relaxation is examined. In section 3.4 the combined relaxation model is described. For this model, the dependence of the combined relaxation rate on the soliton and electronic relaxation rates is derived, starting from the theory reviewed in section 3.1.

The theory enabling the parameters of the Fe^{2+} electronic Hamiltonian to be

determined from the temperature variation of the quadrupole splitting is outlined in section 3.5. The magnetic hyperfine field and the effective exchange field of the Fe^{2+} ion in the Co^{2+} chain are also discussed in this section.

In section 3.6 the theory of the angular dependence for the absorption probability of Mössbauer gamma–rays is covered. This thorough treatment led to a derivation of the relative intensities of the Mössbauer absorption lines in an oriented powder.

The interaction of a soliton in a chain of Co^{2+} ions with an Fe^{2+} ion in that chain is treated in section 3.7. Perturbation theory was applied, and the calculation is outlined up to the point where numerical values are required. The calculation was not pursued further due to the difficulties in obtaining coefficients of fractional parentage for more–than–half–filled shells.

Finally, the theory chapter contains a section on the calculation of the minimum concentration of ^{57}Fe doped into $NH_4Co_{1-x}Fe_xCl_3$ consistent with obtaining a Mössbauer spectrum in a reasonable time. This calculation was used as a guide in growing a low ^{57}Fe concentration $NH_4Co_{1-x}Fe_xCl_3$ crystal, to see whether extra lines in spectra of $NH_4Co_{0.9916}Fe_{0.0084}Cl_3$ were due to the ^{57}Fe concentration being too large.

The results of fitting the Mössbauer spectra of NH_4FeCl_3 are given in section 4.1. At temperatures below 4.2 K the theory of sections 3.1 and 3.6 is used to fit the Mössbauer spectra of the magnetically ordered preferentially oriented powder absorber.

Sections 4.2 and 4.3 are devoted to the results obtained from the Mössbauer spectra of $NH_4Co_{1-x}Fe_xCl_3$ and $CsCo_{1-x}Fe_xCl_3$. At temperatures below T_{N_1} the spectra were fitted using the 2–level, 3–level, and combined relaxation models.

In chapter 5 conclusions are drawn about these relaxation models and the soliton relaxation rates.

Chapter 2

Experimental Details

2.1 The Mössbauer Spectrometer

The transmission Mössbauer spectrometer at the Canterbury University Physics Department comprised a radioactive source, a stationary absorber, and a gamma - ray detector. The energy of emission of the radioactive source was Doppler shifted by oscillating the source. Control, modulation, and detection were provided by a Ranger Scientific (RSI) MS-900 spectrometer.

The source was moved back and forth under constant acceleration by the electromechanical velocity transducer. A symmetric triangular waveform output from the controller was used to drive the velocity transducer. The controller also synchronised the detector and binned the counts from the detector into 1024 channels. The 'velocity setting', which determined the maximum velocity of the source, could be dialled to allow the best resolution of the baseline and spectral features.

The source was ^{57}Co in a Rh matrix, purchased from Amersham on 11/1/1989. When purchased it had a stated activity of 50 mCi. Using the half-life of ^{57}Co of 271 days (Handbook of Chemistry and Physics 1990), the source activity was calculated to range from 35 mCi to 10 mCi during the period when spectra were taken. The source was kept at room temperature and the manufacturers quoted the linewidth to be 0.102 mm s^{-1}.

The overall distance from the source to the detector was $\sim$ 20 cm. The detector was a 97% Kr - 3% CO_2 proportional counter with a Beryllium window. The upper and lower levels of the discriminator were set to select the 14.4 keV Mössbauer

transition and to minimise the background contribution of ^{57}Fe and Rh X-rays.

Absorber temperatures below 5 K were probed using a Mössbauer spectrometer at Liverpool University. A standard transmission geometry was used, with a symmetric triangular output from the controller. A sample temperature of 4.2 K was achieved by immersing the sample in liquid Helium, and pumping on the Helium allowed temperatures of 1.3 and 2.8 K to be reached.

2.2 Data Analysis

Calibration spectra of a National Bureau of Standards natural iron foil (SRM No. 1541) were taken whenever the source velocity setting was changed, or every few weeks. The absorption lines of these calibration spectra were fitted with Lorentzian lineshapes using a least squares routine. Line positions of raw spectra taken with a symmetric triangular waveform are symmetric about the velocity extremes, half-way through the cycle of the velocity transducer. The spectra of samples (other than calibration spectra) were folded about the point of symmetry determined from the calibration spectra.

During the part of the velocity cycle when the source is closer to the detector, the detector window subtends a larger angle at the source, so the count-rate recorded in this part of the cycle is larger than when the source is further away. The curvature of the baseline is almost completely removed after folding.

The velocity scales for folded spectra were found by least-squares fitting a linear scale to the known line positions of the calibration spectra. Isomer shifts were quoted relative to the centroid of the standard iron foil line positions.

Uncertainties in the channel number corresponding to zero isomer shift (the parameter CENTRE obtained from fitting the calibration spectra) affect quoted isomer shifts measured from spectra. Uncertainties in the fitted ratio (the parameter CALIB) of channel number to source velocity affect the isomer shifts, quadrupole splitting, line-width, and hyperfine field measured from spectra. Both of these two types of uncertainties are caused by drift of the spectrometer calibration between (or during) runs, and also by inaccuracies in the fitted line positions in the calibration spectra, due to the usual statistical noise in spectra.

For the velocity setting v=4 (maximum source speed of approximately

± 4 mm s^{-1}), the uncertainties in CALIB and CENTRE were estimated from a series of 9 consecutive standard spectra taken over the period of 1 week. The data obtained from these 9 spectra were: mean CALIB = 61.5363 channels/mm s^{-1}, with uncertainty (standard deviation) of 0.5401 channels/mm s^{-1}, hence a relative uncertainty in CALIB of 0.0088, and the uncertainty (standard deviation) in CENTRE was found to be 0.1055 channels, or using the mean value of CALIB, 0.0017 mm s^{-1}.

Spectra of samples above T_{N_1} were fitted with a pair of Lorentzian curves. Uncertainties in the fitted parameters were calculated as shown in table 2.1, where S_1 and

Quantity measured	Uncertainty calculation
Quadrupole splitting	$\sqrt{S_1^2 + S_2^2 + (0.0088\varepsilon)^2}$
Linewidth	$\sqrt{gerr^2 + (0.0088\varepsilon)^2}$
Isomer shift	$\sqrt{S_1^2 + S_2^2 + (0.0017\text{mm s}^{-1})^2 + (0.0088\varepsilon)^2}$

Table 2.1: Uncertainty calculation for quadrupole split lines.

S_2 are the computational uncertainties of the 2 line positions, ε is the value of the quantity measured, and *gerr* is the computational uncertainty of the linewidth. The major contribution to uncertainties in quadrupole splitting and isomer shift arose from uncertainty in CALIB, while *gerr* and the uncertainty in CALIB contributed equally to the uncertainty in linewidth.

For spectra which weren't fitted with Lorentzian lineshapes (for example, spectra exhibiting relaxation) the uncertainty of a given parameter was found by attempting fits with that parameter fixed at various values around the best fit value, and with all the other parameters free to vary. The uncertainty for the parameter was then chosen so that the fits obtained when the parameter was within the range of the chosen uncertainty fell within acceptable limits of Chi-squared for the best fit, and all the qualitative features (e.g., numbers of lines, general shape of spectrum) were fitted.

There was a small amount of Fe impurity in the window of the detector. This resulted in two "window lines" in all recorded spectra of depth given by 0.2780 % and 0.2910 % of the counts arising from 14.4 keV gamma rays. For the recorded spectra other than calibration spectra, the count rate was taken with and without a copper absorber inserted in front of the detector. The copper absorber predominantly

scatters the 14.4 keV gamma rays, leaving 95.25 % of the background portion of the count. The average counts in each channel arising from the 14.4 keV gamma rays could then be computed, and the window lines were calculated and subtracted from the spectra before the spectra were fitted.

2.3 Cryogenics

The absorber was mounted in a RICOR variable temperature cryostat (type MCH–5B) which was evacuated, and then cooled to temperatures between 250 K and 5.2 K using liquid N_2 or He. Three concentric heat shields separated the sample from the outer walls of the cryostat. The temperature of the inner chamber of the cryostat was measured with a gold (0.07% Fe)/chromel thermocouple. Ice was used as a temperature reference. The temperature was maintained to within 0.3 K of the desired temperature using a temperature controller as described by Bocquet (1987) to vary the flow of cryogen through tubes around the sample and in the cavities between the shields. The thermal inertia of the sample ensured that the temperature fluctuations of the sample were less than the measured temperature fluctuations of the thermocouple.

2.4 Vibration Minimisation

For typical samples of 5 mg of natural iron per square cm, the usual linewidths are about 0.25 mm s^{-1}. However, the initial spectra taken of NH_4FeCl_3 above T_{N_1} had very variable linewidths. Linewidths in the range 0.35 to 0.8 mm s^{-1} were observed. Eventually the problem was traced to vibration broadening transmitted to the sample because of a loose support in the cryostat. A small teflon spacer was substituted for the support.

With the spacer fitted, there was still some extra broadening of the spectral lines when He cryogen was used. Linewidths of (0.245 ± 0.001) mm s^{-1} were observed using N_2 coolant, whereas with He, linewidths were (0.260 ± 0.001) mm s^{-1}, both at 150 K.

Thick rubber bungs were fitted to the underside of the He dewar, as shown in figure 2.1. With these measures taken, no difference was detectable between spectra

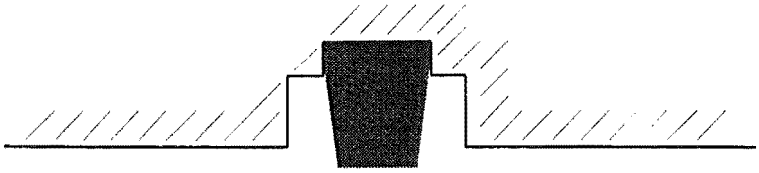

Figure 2.1: Rubber supports for the Helium dewar.

taken with N_2 or He cryogen. The linewidth was found to be (0.247 ± 0.002) mm s^{-1} when a 150 K spectrum was taken with the He dewar supported on rubber bungs. Figure 2.2 shows Mössbauer spectra of NH_4FeCl_3 taken at 150 K before and after the above modifications. Thus the extra broadening was due to building vibrations being transmitted through the He dewar to the cryostat and hence to the sample. The spectra affected by vibration broadening were re-taken after the above problems were remedied.

2.5 Crystal Synthesis

NH_4FeCl_3 was grown by the Bridgman method, by lowering a melt of $FeCl_2$ and NH_4Cl out of the hot zone of a furnace. Details of the process and of the preparation of the constituents are given in section 2.5.2.

$NH_4Co^{57}_{1-x}Fe_xCl_3$ was grown in the same manner as NH_4FeCl_3, from a melt of $Co^{57}_{1-x}Fe_xCl_2$ and NH_4Cl. The $Co^{57}_{1-x}Fe_xCl_2$ was prepared by first dissolving the ^{57}Fe foil in dilute hydrochloric acid, then adding dissolved $CoCl_2$ and drying the solution. Further details are given in section 2.5.1

The raw materials (NH_4Cl, $CoCl_2.6H_2O$, and $FeCl_2.4H_2O$) were all BDH AnalaR grade . The ^{57}Fe enriched iron foil was obtained from Alfred Hempl, Düsseldorf with a stated 95.2 % ^{57}Fe.

All compounds (except NH_4Cl) were hygroscopic, and so a dry box was used for storing and handling these materials. The dry box was a perspex box measuring $45 \times 45 \times 125$ cm^3. A fan and molecular sieves were used to keep the humidity below 15 %. A digital balance was housed inside so that samples could be weighed without leaving the dry environment.

At the temperature of the melt for NH_4CoCl_3 (or NH_4FeCl_3), NH_4Cl has a high

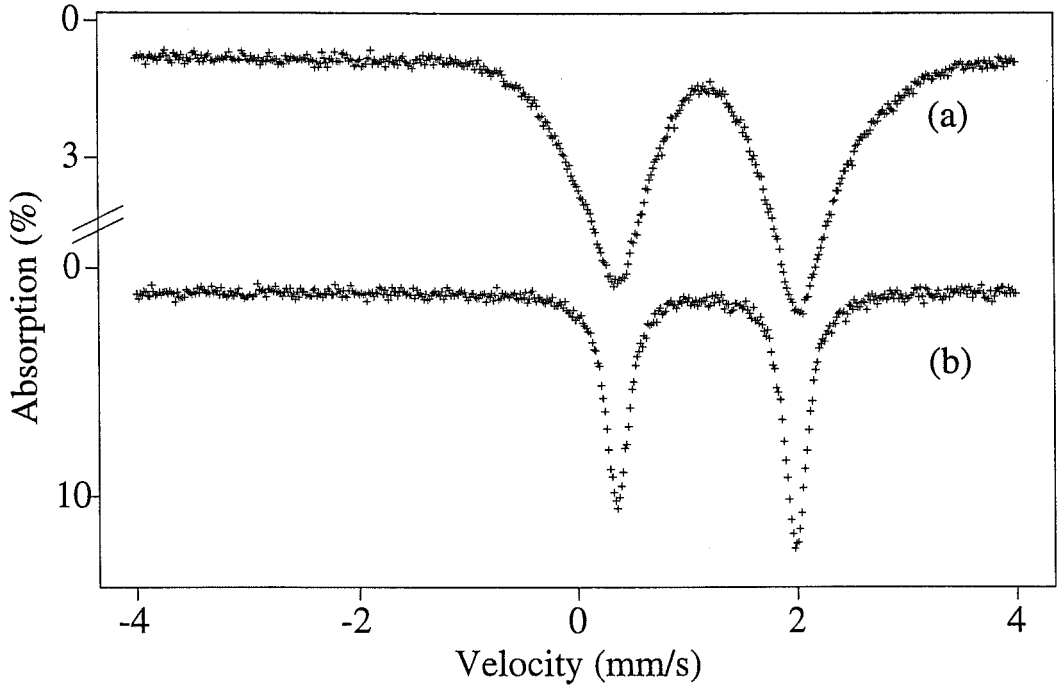

Figure 2.2: Mössbauer spectra of NH_4FeCl_3 taken at 150 K (a) before the modifications using N_2 cryogen, and (b) after the modifications using He cryogen with the He dewar supported by rubber bungs.

vapour pressure, so that some of the NH_4Cl will be in the gas phase when the crystals are formed. Hence a small excess of NH_4Cl is necessary so that the stoichiometric amount of NH_4Cl is in the melt. The vapour pressure of NH_4Cl was calculated from data in *The Handbook of Chemistry and Physics* (1990) to be 15.4 atm at 460 °C (the melting point of NH_4CoCl_3) and 22 atm at 480 °C (the melting point of NH_4FeCl_3). The necessary amount of NH_4Cl in excess of the stoichiometric amount was calculated using the Ideal Gas Law. Assuming the above pressures, and that the length of ampoule not occupied by the melt was 2.5 cm, the excess of NH_4Cl required was calculated to be 17 mg for NH_4CoCl_3 and 24 mg for NH_4FeCl_3.

Care must be taken that the vial the crystal is grown in is strong enough to withstand the above pressures. Manufacturers specifications stated that the sealed vitreous silica (quartz) tubes used in this experiment burst at 30 atm. They had an 8 mm internal diameter with 1 mm thick walls.

2.5.1 $NH_4Co_{1-x}Fe_xCl_3$

NH_4CoCl_3 crystals doped with approximately 1 and 0.5 atomic % ^{57}Fe were grown. The dry $CoCl_2$ was obtained by drying $CoCl_2.6H_2O$ in a vacuum oven at ~70 °C for a period of several weeks.

In detail, the process adopted was:

1. Dissolve a weighed amount of ^{57}Fe in dilute HCl.
2. Dissolve the stoichiometric amount of $CoCl_2$ in distilled water. Add to the dissolved ^{57}Fe.
3. Evaporate and dry the mixture in a vacuum desiccator. Pump down slowly and leave for ~ 36 hours until evaporated.
4. Flush an 8 mm quartz tube with dry N_2 gas ready for the $CoCl_2$.
5. Grind the $CoCl_2$ crystals.
6. Transfer the $CoCl_2$ powder to the quartz tube, attach the tube to the vacuum system, and slowly pump down using a mercury diffusion pump. A fine quartz sieve was placed in the system above the quartz tube to help prevent the $CoCl_2$ mixture permeating the vacuum system.
7. Heat slowly to 70 °C, leave for 24 hrs, then heat slowly to 370 °C and leave for at least 24 hrs. This step drives off any Fe^{3+} ions since $FeCl_3$ decomposes at 306 °C (Handbook of Chemistry and Physics 1990). The $CoCl_2$ should change colour from purple to light blue.
8. Add dry N_2 gas to bring the vacuum system to atmospheric pressure and transfer the quartz tube to the dry box.
9. Place the stoichiometric amount of NH_4Cl plus the calculated excess in a tube on the vacuum system. Evacuate and warm to 50 – 60 °C for at least 24 hrs.
10. Fill the tube with dry N_2 gas and transfer to the dry box.
11. Mix the $CoCl_2$ and NH_4Cl powders. Tip back into the quartz tube.

12. Transfer to vacuum system, evacuate, flush with dry N_2 gas, and evacuate to 2×10^{-5} Torr. Seal the tube off.

13. Heat the ampoule slowly in the hot zone of the Bridgman furnace. Leave at 460 °C for 12 hrs (Asch 1973), then over a period of 6 hrs, slowly lower out of the hot zone.

The resulting boule appeared dark blue, with many needle-like crystallites. Upon crushing the compound appeared light blue.

Two crystals of $NH_4Co_{1-x}Fe_xCl_3$ were prepared. The dry reagent quantities were as in table 2.2.

	$CoCl_2$ (mg)	^{57}Fe foil (mg)	NH_4Cl (mg)	nominal at. % Fe
Crystal B	587 ± 1	2.6 ± 0.6	255 ± 1	1
Crystal C	1889 ± 1	4.2 ± 0.6	815 ± 1	0.5

Table 2.2: Final reagent amounts for $NH_4Co_{1-x}Fe_xCl_3$ synthesis.

2.5.2 NH_4FeCl_3

$FeCl_2$ was prepared by dehydrating $FeCl_2.4H_2O$ in a stream of dry HCl gas at a temperature of 400 – 500 °C (Witteveen and vanVeen 1973). The apparatus used is shown below in figure 2.3. The remaining $FeCl_2$ was melted (m.p. for $FeCl_2$ is 672 °C. (Sidgewick 1950)) and forced through a quartz sieve by reversing the gas flow.

In detail, the steps taken were as follows:

1. Slowly heat $FeCl_2.4H_2O$ in the furnace in a flow of $HCl_{(g)}$, leaving at 500 °C for 6 hrs, then heat to 690 °C (melt) and reverse the gas flow so that the melt falls through the quartz sieve into the tube.

2. Seal the tube of $FeCl_2$ and store in the dry box.

3. Dry the stoichiometric amount plus the small calculated excess of powdered NH_4Cl on the vacuum system at 50 – 60 °C for 1 day.

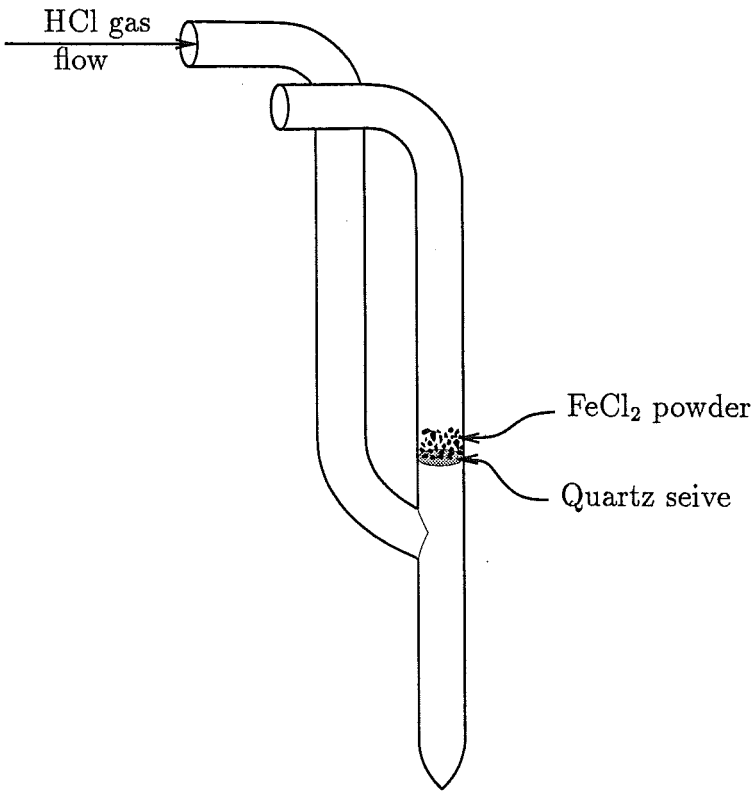

Figure 2.3: Quartz tube used in the preparation of $FeCl_2$.

4. Fill the tube with dry N_2 gas, cork, and transfer to the dry-box.

5. Mix the NH_4Cl and $FeCl_2$.

6. Transfer the mixture to the vacuum system, evacuate the tube to 2×10^{-5} Torr, and seal.

7. Heat the ampoule slowly in a Bridgman furnace to 480 °C (Asch 1973), leave for 12 hrs, then over a period of 6 hrs, slowly lower out of the hot zone.

The resulting boule appeared dark brown, and was formed in many needle-like crystallites. When crushed, the compound appeared light brown.

The reagent quantities used in NH_4FeCl_3 synthesis were (868±1) mg of $FeCl_2$ and (386±1) mg of NH_4Cl.

2.6 X-Ray Diffraction of NH_4FeCl_3

The crystal structure of NH_4FeCl_3 was determined by X-ray diffraction. A small, approximately 1 mm^3, sample of NH_4FeCl_3 was mounted in a stream of cold N_2 gas (from liquid N_2) at 173 K on a Nicolet R3m diffractometer using graphite-monochromated Mo-K_α radiation. Using 2.0° ω-scans at 4.88 - 29.3°.min^{-1}, 182 unique reflections were collected in the range $3° < 2\theta < 50°$, and 168 reflections with $I > 3\sigma(I)$ were used for the structural analysis. The structure was solved using Patterson methods, and was refined in the space group P3 with R=0.067, R_w=0.12.

2.7 Absorber Preparation

Powder absorbers were prepared in the dry-box by crushing the crystal using a mortar and pestle. This powder was mixed with finely ground and sieved Boric acid (H_3BO_3), which acts as a binding agent. The resulting powder was pressed into a 17 mm diameter disk inside a metal ring under a pressure of 170 MPa.

The amount of NH_4CoCl_3 or NH_4FeCl_3 used in each absorber was chosen so that the ^{57}Fe density was approximately 0.11 mg cm^{-2}, corresponding to 5 mg cm^{-2} of natural iron. The details of the constituents for each NH_4CoCl_3 absorber are shown in table 2.3.

	Source crystal	H_3BO_3 (mg)	NH_4CoCl_3 (mg)
Absorber B	B	149 ± 1	77 ± 1
Absorber C	B	150 ± 1	88 ± 1
Absorber D	B	156 ± 1	72 ± 1
Absorber E	C	99 ± 1	120 ± 1

Table 2.3: $NH_4Co_{1-x}Fe_xCl_3$ absorber composition.

The absorber composition for NH_4FeCl_3 is listed in table 2.4. The spectra taken at Liverpool University were taken of absorbers made from crystal B.

	Source crystal	H_3BO_3 (mg)	NH_4FeCl_3 (mg)
Absorber B	B	174 ± 1	39 ± 1
Absorber D	B	171 ± 1	39 ± 1
Absorber E	B	169 ± 1	38 ± 1

Table 2.4: NH_4FeCl_3 absorber composition.

2.8 Chemical Analysis of NH_4CoCl_3 Crystals and Absorbers

A Varian AA1475 atomic absorption spectrometer was used with an air/acetylene flame, to determine the Fe content of crystal B and absorber E NH_4CoCl_3 (from crystal C).

Two samples of crystal B were taken to get an idea of the variability of Fe distribution. Standard solutions of Fe^{2+} ions, concentrations varying from 0.5 to 5 ppm, were prepared. For crystal B, the results were:

- Sample # 1 was (0.27 ± 0.02) % by weight Fe.
- Sample # 2 was (0.25 ± 0.03) % by weight Fe.

Using an overall composition of (0.26 ± 0.02) % by weight Fe, this converts to (0.84 ± 0.06) at. % Fe.

For absorber E, again 2 samples were taken. The results were:

- Sample # 1 was (0.186 ± 0.007) % by weight Fe.
- Sample # 2 was (0.195 ± 0.006) % by weight Fe.

Sample # 1 was taken from the centre of the absorber, whereas sample # 2 was taken from the proximity of the metal ring which held the sample in the cryostat. Hence sample # 2 was discarded as Fe concentration was expected to be higher close to the metal ring, which had rusted slightly during the time the absorber was in the cryostat. Using the composition (0.186 ± 0.007) % by weight Fe, this converts to (0.595 ± 0.002) at. % Fe.

Crystal B was also examined for impurities using a JOEL JSM 35 scanning electron microscope. 20keV electrons were used, with an Ortec wavelength dispersive analyser. LiF, pentaerythritol (PET), and Rubidium acid phthalate (RAP) were used as analysing diffraction gratings. Up to 12th order Co and Cl K_α diffraction lines were observed. Fe K_α and K_β lines were also present.

Small extra lines were observed at 171.6 and 173.8 in PET, and 156.2 in RAP. These lines were less than $\frac{1}{3}$ the depth of the Fe K_α n=1 line, so (assuming they are K_α lines) they correspond to impurity concentrations of less than $0.85 \times \frac{1}{3} = 0.28$ at. %. These lines aren't due to Cd, Ni, Ru, Mo, Er, or higher orders of Fe, Cl, or Co emission, and remain unidentified.

Chapter 3

Theory

3.1 Relaxation Theory

The theory of Blume and Tjon (1968) can be used to calculate Mössbauer lineshapes in the presence of randomly fluctuating electric field gradients or magnetic hyperfine fields. In this section the theory of Blume and Tjon is adapted for the case of absorption of gamma–rays by the nucleus, enabling development in subsequent sections.

Consider a system (for example, a crystal) described by a Hamiltonian $\mathcal{H}$, with ground state $|\alpha\rangle$ and excited state $|\lambda\rangle$. Let $\mathcal{H}^-$ be the Hamiltonian describing the absorption of a photon by the system. In units of $\hbar = 1$, the probability per unit time that a photon of frequency ω will be absorbed by the system, which makes a transition from initial state $|\alpha\rangle$ to final state $|\lambda\rangle$, is then given by (Lamb 1939, Singwi and Sjolander 1960)

$$I_{\alpha\lambda}(\omega) = \frac{|\langle\lambda|\mathcal{H}^-|\alpha\rangle|^2}{(\omega + E_\alpha - E_\lambda)^2 + \frac{1}{4}\Gamma^2}\,, \tag{3.1}$$

where Γ is the full width at half maximum depth of the absorption probability, due to the Heisenberg uncertainty in the excited state energy, and E_α, E_λ are the ground and excited state energies corresponding respectively to the eigenvectors $|\alpha\rangle$ and $|\lambda\rangle$ of the Hamiltonian $\mathcal{H}$ describing the system.

Expressing $I_{\alpha\lambda}$ as a Fourier transform, the result

$$I_{\alpha\lambda}(\omega) = |\langle\lambda|\mathcal{H}^-|\alpha\rangle|^2\,(2/\Gamma)\,Re\int_0^\infty dt\exp[i(\omega + E_\alpha - E_\lambda)t - (1/2)\Gamma t]\,, \tag{3.2}$$

or

$$I_{\alpha\lambda}(\omega) = (2/\Gamma)\, Re \int_0^\infty dt \exp[i\omega t - (1/2)\Gamma t]\langle\alpha|U^\dagger(t)\mathcal{H}^+U(t)|\lambda\rangle\langle\lambda|\mathcal{H}^-|\alpha\rangle\,, \quad (3.3)$$

is obtained, where $\mathcal{H}^+ = \mathcal{H}^{-\dagger}$, and the evolution operator is given by

$$U(t) = \exp(-i\mathcal{H}t)\,. \quad (3.4)$$

The total absorption function $I(\omega)$ is calculated from $I_{\alpha\lambda}(\omega)$ by averaging over the initial states $|\alpha\rangle$ and summing over the final states $|\lambda\rangle$ of the system, that is, $I(\omega) = \sum_{\alpha\lambda} p_\alpha I_{\alpha\lambda}(\omega)$, where p_α is the probability of occurrence of the initial state $|\alpha\rangle$. The lineshape function for the Mössbauer spectrum is obtained by convolving the source lineshape function with the absorber lineshape function. In the case of the thin absorber (Steiner *et al* 1968) this convolution is well approximated by equation (3.3) with Γ replaced by the experimentally observed full width at half maximum depth (the linewidth), comprising contributions from the source, absorber, and detector. Defining $< \theta >= \sum_\alpha p_\alpha\langle\alpha|\theta|\alpha\rangle$, and introducing the Heisenberg operator $\mathcal{H}^+(t) = U^\dagger(t)\mathcal{H}^+U(t)$, the lineshape is given by

$$I(\omega) = (2/\Gamma)Re \int_0^\infty dt \exp[(i\omega - \Gamma/2)t] < \mathcal{H}^+(t)\mathcal{H}^- > \,. \quad (3.5)$$

To simplify the problem, we restrict our attention from the whole system to just the nuclear Hamiltonian, which is then subject to random time-dependent fluctuations due to the changing nuclear environment. For example, consider the stochastic nuclear Hamiltonian

$$\mathcal{H}(t) = \mathcal{H}_0 + Q'(3{I_z}^2 - \boldsymbol{I}^2) + g\mu B I_z f(t). \quad (3.6)$$

$\mathcal{H}_0$ is the unperturbed Hamiltonian for the nucleus in the absence of fields and Q' is the nuclear quadrupole moment operator. The states for the whole system, $|\alpha\rangle$ and $|\lambda\rangle$, are replaced by the nuclear states $|I_0 m_0\rangle$ and $|I_1 m_1\rangle$ respectively, so that the unperturbed Hamiltonian has the property

$$\mathcal{H}_0|I_0 m_0\rangle = E_0|I_0 m_0\rangle\,,\ \mathcal{H}_0|I_1 m_1\rangle = E_1|I_1 m_1\rangle\,.$$

The g factors for the ground and excited states are given by

$$g|I_0 m_0\rangle = g_0|I_0 m_0\rangle\,,\ g|I_1 m_1\rangle = g_1|I_1 m_1\rangle$$
$$\text{and} \quad Q'|I_0 m_0\rangle = 0\,,\ Q'|I_1 m_1\rangle = \frac{|e|QV_{zz}}{4I(2I-1)}|I_1 m_1\rangle\,.$$

$f(t)$ is a stochastic random function of time. For example, if $f(t)$ assumes values of 1 and β, with $-1 < \beta < 1$, Hamiltonian (3.6) models the situation of 2–level electronic relaxation discussed in section 3.2, where the magnetic hyperfine field is along the z principal axis of the electric field gradient, and fluctuates between values of B and βB.

Since the Hamiltonian is now time dependent, the time-ordered evolution operator

$$U(t) = \exp\left[-i\int_0^t \mathcal{H}(t')dt'\right] \tag{3.7}$$

must be used for $U(t)$ in equation (3.3). Under a stochastic Hamiltonian, equation (3.5) becomes

$$I(\omega) = (2/\Gamma)Re\int_0^\infty \exp[(i\omega - \Gamma/2)t]\left(< \mathcal{H}^+(t)\mathcal{H}^- >\right)_{\text{av}}, \tag{3.8}$$

where $(\ )_{\text{av}}$ means the average over the stochastic degrees of freedom (in our case, all the combinations of $f(t)$ over the Mössbauer lifetime).

Substituting for $U(t)$, the matrix elements are

$$\langle I_0 m_0|U^\dagger(t)|I_0 m_0'\rangle = \exp\left\{i[E_0 t + g_0\mu B m_0\int_0^t f(t')dt']\right\}\delta_{m_0 m_0'}$$

and

$$\langle I_1 m_1'|U(t)|I_1 m_1\rangle = \exp\left\{-i[E_1 t + 1/12|e|QV_{zz}(3{m_1}^2 - 15/4)t + g_1\mu B m_1\int_0^t f(t')dt']\right\}\delta_{m_1 m_1'}$$

Upon rearranging the order of averaging,

$$\left(< \mathcal{H}^+(t)\mathcal{H}^- >\right)_{\text{av}} = \Big(\sum_{m_0' m_1' m_0 m_1} p_{|I_0 m_0\rangle}$$

$$\times\langle I_0 m_0|U^+(t)|I_0 m_0'\rangle\langle I_0 m_0'|\mathcal{H}^+|I_1 m_1'\rangle\langle I_1 m_1'|U(t)|I_1 m_1\rangle\langle I_1 m_1|\mathcal{H}^-|I_0 m_0\rangle\Big)_{\text{av}}$$

$$= \sum_{m_0 m_1} p_{|I_0 m_0\rangle}\left|\langle I_1 m_1|\mathcal{H}^-|I_0 m_0\rangle\right|^2\left(\langle I_0 m_0|U^\dagger(t)|I_0 m_0\rangle\langle I_1 m_1|U(t)|I_1 m_1\rangle\right)_{\text{av}}, \tag{3.9}$$

and assuming that the probability of occurrence of each initial state $|I_0 m_0\rangle$ is independent of m_0, i.e., $p_{|I_0 m_0\rangle} = 1/(2I_0 + 1) = 1/2$, the lineshape function is

$$I(\omega) = Re\sum_{m_0 m_1} D_{m_0 m_1}\int_0^\infty dt\exp\left[-i\mathcal{E}t - (\Gamma/2)t\right]G(t) \tag{3.10}$$

where $G(t) \equiv \left(\exp[i\alpha \int_0^t f(t')dt']\right)_{\rm av}$ and $D_{m_0 m_1} \equiv (1/\Gamma)\,|\langle I_1 m_1|\mathcal{H}^-|I_0 m_0\rangle|^2$, $\mathcal{E} \equiv -(\omega - \omega_0 - 1/12|e|QV_{zz}(3{m_1}^2 - \frac{15}{4}))$ with $\omega_0 = E_1 - E_0$, and $\alpha \equiv (g_0 m_0 - g_1 m_1)\mu B$. The $D_{m_0 m_1}$ are essentially Clebsch-Gordan coefficients giving the relative probability of the eight different nuclear transitions.

To evaluate $G(t)$ it is assumed that $f(t)$ is a stationary Markov function, i.e., the transition probability for $f(t)$ changing from one value to another is independent of t, and independent of the past history of $f(t)$. These assumptions allow the function $W(f_2|f_1, \Delta t)$ to be defined as the probability that $f(t + \Delta t) = f_2$ given that $f(t) = f_1$. Following Abragam (1961),

$$G(t) = \lim_{n\to\infty} \sum_{(f_1,\ldots,f_n)} P(f_1, t_1; \ldots; f_n, t_n) \exp\left[i\alpha(f_1 + \ldots + f_n)(t/n)\right] \tag{3.11}$$

where $\Delta t = t/n$, $t_k = k\Delta t$, and the sum has to be taken over all possible paths of the set $(f_1, \ldots, f_n)$. $P(f_1, t_1; \ldots; f_n, t_n)$ is the probability that the stochastic function has the value f_1 at t_1, f_2 at t_2, and so on. That is,

$$P(f_1, t_1; \ldots; f_n, t_n) = K_{f_1} W(f_2|f_1, \Delta t) \ldots W(f_n|f_{n-1}, \Delta t)\,. \tag{3.12}$$

K_{f_1} is the equilibrium probability that the stochastic function $f(t)$ has initial value f_1.

Let $G_\mu(t)$ be the sum of terms of $G(t)$ (equation (3.11)) for which $f(t)$ has a particular value of f_μ at time t, i.e.,

$$G_\mu(t) \equiv \lim_{n\to\infty} \sum_{(f_1,\ldots,f_{n-1})} P(f_1, t_1; \ldots; f_\mu, t_n) \exp\left[i\alpha(f_1 + \ldots + f_\mu)(t/n)\right] \tag{3.13}$$

for a particular f_μ, so that $G(t) = \sum_{f_\mu} G_\mu(t)$.

When Δt is small enough, $W(f_2|f_1, \Delta t)$ can be expanded in a power series of Δt, and when higher orders of Δt are discarded, for $f_2 \neq f_1$

$$W(f_2|f_1, \Delta t) \simeq \pi(f_1, f_2)\Delta t\,, \tag{3.14}$$

since $W(f_2|f_1, 0) = 0$ when $f_2 \neq f_1$. From the definition of equation (3.14),

$$\pi(f_1, f_2) = \frac{d}{d\Delta t} W(f_2|f_1, \Delta t)\bigg|_{\Delta t=0}\,. \tag{3.15}$$

For the case $f_2 = f_1$,

$$W(f_1|f_1, \Delta t) \simeq 1 + \pi(f_1, f_1)\Delta t\,, \tag{3.16}$$

since $W(f_1|f_1,0) = 1$. The sum of the probabilities W must equal unity, that is $\sum_{f_2} W(f_2|f_1,\Delta t) = 1$, so consequently

$$\pi(f_1,f_1) = -\sum_{f_2 \neq f_1} \pi(f_1,f_2)\,. \tag{3.17}$$

Combining equations (3.14) and (3.16), the probability function W is given by

$$W(f_2|f_1,\Delta t) \simeq \delta_{f_1 f_2} + \pi(f_1,f_2)\Delta t\,. \tag{3.18}$$

From equation (3.15), $\pi(f_1,f_2)$ can be interpreted as the transition rate for the stochastic function $f(t)$ making a transition from value f_1 to value f_2 given that $f(t) = f_1$. Therefore the transition rate from value f_1 to value f_2 is $K_{f_1}\,\pi(f_1,f_2)$.

The time evolution of $G_\mu(t)$ can be found by differentiating equation (3.13), and using equations (3.12) and (3.14) to obtain

$$\frac{dG_\nu}{dt} = i\alpha f_\nu G_\nu + \sum_{f_\mu} \pi(f_\mu,f_\nu) G_\mu(t)\,,$$

or, converting to matrix notation,

$$\boldsymbol{\pi}_{\mu\nu} \equiv \pi(f_\mu,f_\nu)\,,\ \boldsymbol{F}_{\mu\nu} \equiv f_\mu\delta_{\mu\nu}\,,\ \boldsymbol{G}_\mu \equiv G_\mu\,,\ \boldsymbol{K}_\mu \equiv K_{f_\mu}\,,\ \text{and}\ \mathbf{1}_\mu \equiv 1\,,$$

the result is

$$\frac{d\boldsymbol{G}}{dt} = \boldsymbol{G}(i\alpha\boldsymbol{F} + \boldsymbol{\pi})$$

yielding

$$\boldsymbol{G}(t) = \boldsymbol{G}(0)\exp[(i\alpha\boldsymbol{F} + \boldsymbol{\pi})t]\,.$$

From equations (3.11) and (3.12), $\boldsymbol{G}(0) = \boldsymbol{K}$, and

$$\begin{aligned} G(t) &= \sum_{f_\mu} \boldsymbol{G}_\mu(t) \\ &= \boldsymbol{K}.\exp[(i\alpha\boldsymbol{F} + \boldsymbol{\pi})t].\mathbf{1} \end{aligned} \tag{3.19}$$

Substituting for $G(t)$ in equation (3.10), the lineshape is

$$\begin{aligned} I(\omega) &= Re \sum_{m_0 m_1} D_{m_0 m_1} \int_0^\infty dt\ \exp[-i\mathcal{E}t - (\Gamma/2)t]\boldsymbol{K}.\exp[(i\alpha\boldsymbol{F} + \boldsymbol{\pi})t].\mathbf{1}\,. \\ &= Re \sum_{m_0 m_1} D_{m_0 m_1} \int_0^\infty dt\ \boldsymbol{K}.\exp(\boldsymbol{A}t).\mathbf{1}\,, \end{aligned} \tag{3.20}$$

where $\boldsymbol{A}_{\mu\nu} \equiv i(\alpha \boldsymbol{F}_{\mu\nu} - \mathcal{E}\delta_{\mu\nu}) + \boldsymbol{\pi}_{\mu\nu} - (\Gamma/2)\delta_{\mu\nu}$. Performing the integration, the lineshape is

$$I(\omega) = Re \sum_{m_0 m_1} D_{m_0 m_1} \boldsymbol{K}.\boldsymbol{A}^{-1}.\mathbf{1}\,. \tag{3.21}$$

This expression is somewhat clumsy to use for calculating spectra, since for each frequency ω the matrix $\boldsymbol{A}$ must be inverted. Clauser (1971) reduced the number of matrix manipulations necessary for the calculation of the lineshape function by using the fact that the frequency appears only in the diagonal elements of $\boldsymbol{A}$. Defining $\boldsymbol{Z}$ by $\boldsymbol{A} = \boldsymbol{Z} + i\omega\boldsymbol{I}$ where $\boldsymbol{I}$ is the identity matrix, allows the intensity to be written as

$$I(\omega) = Re \sum_{m_0 m_1} D_{m_0 m_1} \mathrm{Tr}[\boldsymbol{X}^{-1}\boldsymbol{E}\boldsymbol{\sigma}\boldsymbol{X}(\boldsymbol{\lambda} - i\omega\boldsymbol{I})^{-1}]\,, \tag{3.22}$$

where $\boldsymbol{X}$ is the matrix of column eigenvectors of $\boldsymbol{Z}$, $\boldsymbol{\lambda}$ is the diagonal matrix of corresponding eigenvalues of $\boldsymbol{Z}$, $\boldsymbol{E}$ is a matrix of 1's, and $\boldsymbol{\sigma}$ is the diagonal matrix of values of $\boldsymbol{K}$. Since $(\boldsymbol{\lambda} - i\omega\boldsymbol{I})^{-1}$ is diagonal, only diagonal elements of $\boldsymbol{X}^{-1}\boldsymbol{E}\boldsymbol{\sigma}\boldsymbol{X}$ will contribute to the trace, so finally

$$I(\omega) = Re \sum_{m_0 m_1} D_{m_0 m_1} \sum_j \frac{[\boldsymbol{X}^{-1}\boldsymbol{E}\boldsymbol{\sigma}\boldsymbol{X}]_{jj}}{\boldsymbol{\lambda}_{jj} - i\omega}\,. \tag{3.23}$$

$I(\omega)$ is approximately a sum of Lorentzian lines. The real and imaginary parts of the eigenvalues $\boldsymbol{\lambda}$ give the linewidth and position of the lines respectively. For each nuclear transition the relative intensities of the lines are contained in the trace of $\boldsymbol{X}^{-1}\boldsymbol{E}\boldsymbol{\sigma}\boldsymbol{X}$, and the relative intensities and angular dependence of the transition probabilities are given by the $D_{m_0 m_1}$ factors. An absorption spectrum can be calculated by subtracting the lineshape function $I(\omega)$ from the baseline count rate.

In the case where the relaxing magnetic hyperfine field is not parallel to the z principal axis of the electric field gradient (as for NH_4FeCl_3), or if the asymmetry parameter $\eta \neq 0$, the stochastic Hamiltonian (3.6) does not commute with itself at different times. That is, some t exists such that $[\mathcal{H}(0), \mathcal{H}(t)] \neq 0$, and the stochastic and quantum mechanical averages which occur in the lineshape calculation cannot be separated as in equation (3.9). In this case the method of Blume (1968) is followed and the Louiville operator formalism is introduced. A good summary of the method may be found in Grandjean (1988). Dunlap and Shenoy (1976) also deal with this subject.

Defining the Louiville operator $A^\times$ acting on the operator B as $A^\times B = [A, B]$, it is easy to show (Blume 1968) that the 4-index "matrix-elements" of $A^\times$ are given by

$$\langle \mu\nu | A^\times | \mu'\nu' \rangle = \delta_{\nu\nu'} \langle \mu | A | \mu' \rangle - \delta_{\mu\mu'} \langle \nu | A | \nu' \rangle \, .$$

Also $\exp(A) B \exp(-A) = \exp(A^\times) B$, which is the principal property of Louiville operators allowing the lineshape to be calculated from equation (3.8) as

$$I(\omega) = Re \sum_{m_0 m_1 m_0' m_1'} \langle I_1 m_1 | \mathcal{H}^- | I_0 m_0 \rangle \langle I_0 m_0' | \mathcal{H}^+ | I_1 m_1' \rangle$$
$$\times \sum_{\mu\nu} K_\mu \langle I_0 m_0 I_1 m_1 \mu | [\boldsymbol{K} - \boldsymbol{\pi} - i \sum_j V_j^\times \boldsymbol{F}]^{-1} | I_0 m_0' I_1 m_1' \nu \rangle \, . \quad (3.24)$$

Here $\boldsymbol{K}$, $\boldsymbol{\pi}$ and $\boldsymbol{F}$ are defined on page 33. The μ and ν in equation (3.24) are indices denoting the electronic system. The operators V_j are defined by $\mathcal{H}(t) = \sum_j V_j f_j(t)$. For example, in the case of a magnetic hyperfine field fluctuating between 0 and B in the x direction,

$$V_1 = Q'(3I_z{}^2 - \boldsymbol{I}^2), \qquad f_1(t) = 1,$$
$$\text{and} \quad V_2 = g\mu B I_x, \qquad f_2(t) = f(t) \, .$$

When $\boldsymbol{B}_{\rm hf}$ is not parallel to the z principal axis of the EFG tensor, the computer program FUSTOP (FUll STochastic problem for an Oriented Powder) was used to calculate lineshapes from equation (3.24) using the Clauser formalism, as given in equation (3.23), and the theory for the line intensities of Mössbauer spectra taken of an oriented powder, given in section 3.6. Using the theory for the line intensities of an oriented powder (page 52), I adapted FUSTOP from a computer program FUST obtained from the Liverpool University Oliver Lodge laboratory. FUST calculated lineshapes for a single crystal absorber.

3.2 2–Level Relaxation Model

In fitting Mössbauer spectra of $NH_4Co_{1-x}Fe_xCl_3$ and $CsCo_{1-x}Fe_xCl_3$ taken below T_{N_1}, the 2–level relaxation model developed by Ward *et al* (1987) was applied. The lineshape was calculated by equation (3.23) based on the theory of Blume and Tjon (1968), and it was assumed that only the two lowest electronic states of the Fe^{2+} ions were occupied. (The electronic states of Fe^{2+} in $NH_4Co_{1-x}Fe_xCl_3$ and

$CsCo_{1-x}Fe_xCl_3$ are discussed in sections 3.5, 4.2.2 and 4.3.) The ground and first excited states at 0 K are labelled as state (1) and (2) respectively, with occupation probabilities P_1 and P_2 respectively. Assuming that the states are thermally populated, the occupation probabilities are given by Boltzmann statistics. Defining E_2 as the energy of state (2) minus the energy of state (1),

$$P_2 = \frac{\exp[-E_2/kT]}{1 + \exp[-E_2/kT]}, \tag{3.25}$$

and $P_1 = 1 - P_2$. Equilibrium requires that the sum of the transition probabilities from a particular state is equal to the sum of the transition probabilities to that state. Hence for the 2–level relaxation model,

$$P_1\pi_{12} = P_2\pi_{21}\,. \tag{3.26}$$

The diagonal elements π_{11} and π_{22} of the relaxation matrix $\boldsymbol{\pi}$ are given by equation (3.17), so for 2–level relaxation only one rate parameter is necessary.

Assuming that both electronic states result in the same quadrupole splitting, and that $\boldsymbol{B}_{\rm hf}$ is parallel to the z principal axis of the EFG tensor, the Hamiltonian given in equation (3.6) can be used to describe the nucleus. At temperatures below T_{N_2}, spectra of $NH_4Co_{1-x}Fe_xCl_3$ and $CsCo_{1-x}Fe_xCl_3$ were fitted with relaxation between a magnetic hyperfine field of B and 0 ($f(t) = 1$ and 0) produced by states (1) and (2) respectively.

Between T_{N_2} and T_{N_1}, the relaxation at Fe^{2+} sites in the frustrated chains of $NH_4Co_{1-x}Fe_xCl_3$ and $CsCo_{1-x}Fe_xCl_3$ was expected to be dominated by the passage of solitons. Soliton relaxation in these sites was modeled by relaxation between hyperfine fields of B and $-B$ ($f(t) = 1$ and -1), with equal occupation probabilities. State (2) was ignored in the frustrated chains. 1/3 of the sites are expected to be in frustrated chains, so the relative area of the soliton subspectrum was fixed to 1/3. The remaining sites in 3-dimensionally ordered chains were modeled in the same way as they were below T_{N_2}.

The 2–level relaxation model was implemented for an oriented powder by the computer program MOST (MOssbauer STochastic). The version that was used was re–written in 1984 by Dr John Ward, of the University of Canterbury.

3.3 3–Level Relaxation Model

The 3–level relaxation model enables lineshapes to be calculated when relaxation occurs between the three lowest energy electronic states of Fe^{2+} in $NH_4Co_{1-x}Fe_xCl_3$ and $CsCo_{1-x}Fe_xCl_3$. States (1) and (2) are as defined for the 2–level relaxation model, and the second excited state is labeled state (3). State (3) gives a magnetic hyperfine field of the opposite sign to state (1), so in the sites in 3-dimensionally ordered chains the addition of state (3) permits relaxation between B and $-B$ in addition to the relaxation between B and 0. The sites in frustrated chains were treated using the same approximation that was made in the 2–level relaxation model, namely that the lineshape of these sites is dominated by soliton relaxation between B and $-B$, with equal occupation probability.

In the sites in 3–dimensionally ordered chains, the occupation probabilities of the three states are given by Boltzmann statistics as for the 2–level relaxation model, that is, defining P_3 as the occupation probability of state (3), and E_3 as the energy of state (3) minus the energy of state (1),

$$P_3 = \frac{\exp[-E_3/kT]}{1+\exp[-E_2/kT]+\exp[-E_3/kT]}\,,$$

$$P_2 = \frac{\exp[-E_2/kT]}{1+\exp[-E_2/kT]+\exp[-E_3/kT]}\,, \tag{3.27}$$

and $P_1 = 1 - P_2 - P_3$.

In the case of the 3–level relaxation model, the relaxation matrix $\boldsymbol{\pi}$ has nine elements. There are three equations which determine the diagonal elements of $\boldsymbol{\pi}$, and three equations which are required to satisfy equilibrium conditions, so that only three elements of $\boldsymbol{\pi}$ are independent. However, relaxation between state (2) and either of state (1) or state (3) result in relaxation between magnetic hyperfine fields of 0 and B or 0 and $-B$, giving the same lineshape, so a further reduction in the number of independent rate parameters was necessary. This reduction was achieved by assuming that the relaxation occurs due to a spin–phonon relaxation process, as for a paramagnetic centre. The direct and Raman processes were considered. The Raman process was rejected because the relaxation rates obtained by fitting the 2–level relaxation model to $NH_4Co_{1-x}Fe_xCl_3$ and $CsCo_{1-x}Fe_xCl_3$ spectra (shown in figures 4.11 and 4.16) did not show the T^7 dependence on temperature characteristic of the Raman process for non-Kramers ions (Abragam and Bleaney 1970 p.563).

The relaxation rates given by the direct process are derived in Abragam and Bleaney (1970 p.558). For transitions from a lower energy state $|\psi_i\rangle$ to a higher energy state $|\psi_j\rangle$, separated by energy E, the rate $\pi_f\uparrow$ given that the initial state is occupied is

$$\pi_f\uparrow = \omega_0 \frac{E^3}{\exp[E/(kT)] - 1} \tag{3.28}$$

where ω_0 is a parameter that is fitted, and is related to the density ρ, the speed of sound in the crystal v, and the matrix element of the term linear in strain, $V^{(1)}$, in the expansion of the crystalline electric potential $V = V_0 + \epsilon V^{(1)} + \epsilon^2 V^{(2)} + ...$

$$\omega_0 = \frac{3|\langle\psi_j|V^{(1)}|\psi_i\rangle|^2}{2\pi\hbar^4\rho v^5}. \tag{3.29}$$

The rate $\pi_f\downarrow$ for transitions from a higher energy state to a lower energy state is

$$\pi_f\downarrow = \omega_0 \frac{E^3 \exp[E/(kT)]}{\exp[E/(kT)] - 1} \tag{3.30}$$

Equations (3.28) and (3.30) are used for the off-diagonal elements of $\boldsymbol{\pi}$, and equation (3.17) gives the diagonal elements.

In using equations (3.28) and (3.30), the electronic relaxation rate parameter ω_0 (and hence the matrix element $\langle\psi_j|V^{(1)}|\psi_i\rangle$) in equation (3.29) is assumed to be independent of the electronic states $|\psi_i\rangle$ and $|\psi_j\rangle$ between which the relaxation occurs. This assumption can be partially checked by performing some calculations based on the orbit lattice interaction, following the approach of Orbach (1961), Blume and Orbach (1962), and Price (1978).

The wavefunctions in equation (3.29) are taken to be Born–Oppenheimer products of the form

$$\Phi^0_{i\alpha} = \psi_i|\prod_{\boldsymbol{k},s} N_\alpha(\boldsymbol{k}, s)\rangle$$

where ψ_i are eigenstates of the Hamiltonian for an electron on the Fe^{2+} ion with the surrounding nuclei fixed at their mean positions. These eigenstates are determined for Fe^{2+} in $NH_4Co_{1-x}Fe_xCl_3$ by diagonalizing the Hamiltonian whose parameters are given in section 4.2.2. The Hamiltonian parameters for Fe^{2+} in $CsCo_{1-x}Fe_xCl_3$ are given in section 4.3. The $N_\alpha(\boldsymbol{k}, s)$ are the occupation numbers of the phonon states of wave–vector $\boldsymbol{k}$ and polarisation s; the index α relates the particular set of occupation numbers to the product state $\Phi^0_{i\alpha}$.

Under octahedral symmetry the term in the expansion of the crystalline potential which is linear in strain can be written (Orbach 1961) as

$$\mathcal{H}_{\rm ol} = \sum_{n,m} v_n^m \varepsilon_n^m \,,$$

the scalar product of tensor operators $\boldsymbol{v}$ and $\boldsymbol{\varepsilon}$ whose components v_n^m and ε_n^m transform under rotation as spherical harmonics. Taking into consideration the point symmetry of the ion in the lattice, Price (1978) re–expressed $\mathcal{H}_{\rm ol}$ as

$$\mathcal{H}_{\rm ol} = \sum_{\Gamma,p} \sum_{l} b_l(\Gamma) B_l(\Gamma,p) \varepsilon(\Gamma,p) \,,$$

where $\varepsilon(\Gamma,p)$ are those linear combinations of the strain tensor $\boldsymbol{\varepsilon}$ which transform as the pth subvector of the representation Γ of the relevant point group, and the orbital operators $B_l(\Gamma,p)$ are the appropriately transforming linear combinations of spherical harmonics. The $b_l(\Gamma)$ are the coupling coefficients, and are unknown.

Within the Born–Oppenheimer approximation, the matrix elements of $\mathcal{H}_{\rm ol}$ can be written as products of electronic and phonon matrix elements as

$$\begin{aligned}\langle \Phi^0_{j\beta} | \mathcal{H}_{\rm ol} | \Phi^0_{i\alpha} \rangle = \sum_{\Gamma,p} \sum_{l} b_l(\Gamma) \langle \psi_j | B_l(\Gamma,p) | \psi_i \rangle \\ \times \langle \prod_{\boldsymbol{k},s} N_\beta(\boldsymbol{k},s) | \varepsilon(\Gamma,p) | \prod_{\boldsymbol{k},s} N_\alpha(\boldsymbol{k},s) \rangle \,. \end{aligned} \tag{3.31}$$

The dependence of $\langle \Phi^0_{j\beta} | \mathcal{H}_{\rm ol} | \Phi^0_{i\alpha} \rangle$ on the electronic states $|\psi_i\rangle$ and $|\psi_j\rangle$ is contained in the matrix elements of the $B_l(\Gamma,p)$ operators. Thus, ω_0 will be independent of which states relaxation occurs between if $\langle \psi_1 | B_l(\Gamma,p) | \psi_2 \rangle = \langle \psi_1 | B_l(\Gamma,p) | \psi_3 \rangle$ for all possible l, Γ, and p.

Only even–parity modes of oscillation contribute to matrix elements of $\mathcal{H}_{\rm ol}$ (Price 1978). For 3d ions, only $l = 0$, 2, and 4 need be considered. The $B_0(\Gamma,p)$ operators produce constant matrix elements which do not produce new effects, and so are ignored. In the basis x_+, x_0, and x_- of equation (3.40), the only non–diagonal orbital operators $B_l(\Gamma,p)$ are $B_2(E_{\rm g}^{(1)},p)$, $B_2(E_{\rm g}^{(2)},p)$, $B_4(E_{\rm g}^{(1)},p)$, and $B_4(E_{\rm g}^{(2)},p)$. Under octahedral symmetry, the matrices for the B_4 operators are proportional to those for B_2, so only $B_2(E_{\rm g}^{(1)},p)$ and $B_2(E_{\rm g}^{(2)},p)$ are considered.

The matrix elements of $B_2(E_{\rm g}^{(1)},1)$, $B_2(E_{\rm g}^{(1)},2)$, $B_2(E_{\rm g}^{(2)},1)$, and $B_2(E_{\rm g}^{(2)},2)$ between states (1) and (2) and states (1) and (3) of $NH_4Co_{1-x}Fe_xCl_3$ at 1.3 K and 15 K were calculated using a computer program written at this laboratory (Laban 1994). The results are listed in table 3.1.

matrix element	$B_2(E_g^{(1)},1)$	$B_2(E_g^{(1)},2)$	$B_2(E_g^{(2)},1)$	$B_2(E_g^{(2)},2)$
$\langle r_Q^{-3}\rangle$=3.5 au T=1.3 K				
$\langle 1\|B\|2\rangle$	0.0290	0.0290	0.0178	0.0178
$\langle 1\|B\|3\rangle$	0.0109	-0.0109	-0.0142	0.0142
T=15.0 K				
$\langle 1\|B\|2\rangle$	0.0290	0.0290	0.0179	0.0179
$\langle 1\|B\|3\rangle$	0.0106	-0.0106	-0.0139	0.0139
$\langle r_Q^{-3}\rangle$=4.5 au T=1.3 K				
$\langle 1\|B\|2\rangle$	0.0294	0.0294	0.0180	0.0180
$\langle 1\|B\|3\rangle$	0.0112	-0.0112	-0.0144	0.0144
T=15.0 K				
$\langle 1\|B\|2\rangle$	0.0294	0.0294	0.0180	0.0180
$\langle 1\|B\|3\rangle$	0.0109	-0.0109	-0.0140	0.0140

Table 3.1: Matrix elements of the orbital operators $B_2(E_g)$ between states (1) and (2) and between states (1) and (3) of Fe^{2+} in $NH_4Co_{1-x}Fe_xCl_3$. The wavefunctions used are labelled by the value of the $\langle r_Q^{-3}\rangle$ parameter and correspond to sets of parameters for the electronic Hamiltonian shown in tables 4.5 and 4.7.

These calculations show that, for the wavefunctions considered, the matrix elements of $B_2(E_g)$ are 2 to 3 times larger between states (1) and (2) than between states (1) and (3). Thus, if the coupling coefficients $b_2(\Gamma)$ and the phonon matrix elements are independent of Γ and p, then the ω_0 parameter of equation (3.29) will be 2^2 to 3^2 times larger between states (1) and (2) than between states (1) and (3). This indicates that the assumption that ω_0 is constant is invalid. However, the difficulties in accurately determining the coupling coefficients and phonon matrix elements of the strain tensor make a full calculation of ω_0 impractical, so for the purposes of this thesis, ω_0 is assumed constant.

I wrote a subroutine called THREL (THRee level ELectronic relaxation) which calculates the Mössbauer lineshape for the 3–level relaxation model for an oriented powder. The I/O routines used were those of the program MOST for the 2–level relaxation model, slightly modified because of the different set of parameters.

3.4 Combined Relaxation

In the frustrated chains at temperatures between T_{N_2} and T_{N_1}, there is a possibility that both soliton relaxation and electronic relaxation with similar rates occur at the same site. It is necessary to extend the general theory of Abragam(1961) presented in section 3.1 to include two relaxation processes. If these two relaxation processes are independent electronic relaxation can be represented by the function $f(t)$, as for the 3–level relaxation model, and the stationary Markov function $s(t)$ which takes values +1 and −1 can be introduced to represent soliton relaxation. The Hamiltonian equation (3.6) then becomes

$$\mathcal{H}(t) = \mathcal{H}_0 + Q'(3I_z^2 - \boldsymbol{I}^2) + g\mu B I_z f(t)s(t)\,. \tag{3.32}$$

The product $f(t)s(t)$ models the situation where solitons flip the sign of the magnetic hyperfine field when $f(t) = \pm 1$, and have no effect when $f(t) = 0$. Replacing $f(t)$ by $f(t)s(t)$ in equations (3.6) to (3.10), and defining $W(f_2s_2|f_1s_1, \Delta t)$ as the probability that $f(t+\Delta t) = f_2$ and $s(t+\Delta t) = s_2$ given that $f(t) = f_1$ and $s(t) = s_1$,

$$G(t) = \lim_{n\to\infty} \sum_{(f_1s_1,\ldots,f_ns_n)} P(f_1s_1, t_1; \ldots; f_ns_n, t_n) \exp\left[i\alpha(f_1s_1 + \ldots + f_ns_n)(t/n)\right] \tag{3.33}$$

where

$$P(f_1s_1, t_1; \ldots; f_ns_n, t_n) = K_{f_1s_1} W(f_2s_2|f_1s_1, \Delta t) \ldots W(f_ns_n|f_{n-1}s_{n-1}, \Delta t)\,,$$

and $K_{f_1s_1}$ is the equilibrium probability that both $f(0) = f_1$ and $s(0) = s_1$.

$G_{\mu\nu}(t)$ is defined as in equation (3.13),

$$G_{\mu\nu}(t) = \lim_{n\to\infty} \sum_{(f_1s_1,\ldots,f_{n-1}s_{n-1})} P(f_1s_1, t_1; \ldots; f_\mu s_\nu, t_n) \exp\left[i\alpha(f_1s_1 + \ldots + f_\mu s_\nu)(t/n)\right] \tag{3.34}$$

for particular values of f_μ and s_ν, so that

$$G(t) = \sum_{f_\mu s_\nu} G_{\mu\nu}(t)\,. \tag{3.35}$$

Expanding $W(f_2s_2|f_1s_1, \Delta t)$ in a power series in Δt,

$$W(f_2s_2|f_1s_1, \Delta t) \simeq \delta_{f_1,f_2}\delta_{s_1,s_2} + \pi(f_1s_1, f_2s_2)\Delta t \tag{3.36}$$

where π has 36 elements, one for each combination of f_1, s_1, f_2, and s_2.

Defining 6×6 matrices $\boldsymbol{\pi}_{\mu\rho\nu\sigma} \equiv \pi(f_\mu s_\rho, f_\nu s_\sigma)$, $\boldsymbol{F}_{\mu\rho\nu\sigma} \equiv f_\mu \delta_{\mu\nu} s_\rho \delta_{\rho\sigma}$, the 1×6 row vector $\boldsymbol{K}_{\mu\rho} \equiv K_\mu/2$, and the 6×1 column vector $\mathbf{1}_{\mu\rho} \equiv 1$, equation (3.19) is obtained as in section 3.1.

Before combined relaxation spectra can be fitted meaningfully, the elements of the combined relaxation matrix $\boldsymbol{\pi}_{fs}$ must be related to elements of the electronic $\boldsymbol{\pi}_f$ and soliton $\boldsymbol{\pi}_s$ relaxation matrices. If electronic and soliton relaxation processes are independent, the occupation probability of the combined state is

$$W_{fs}(yv|xu, \Delta t) = W_f(y|x, \Delta t) W_s(v|u, \Delta t) \tag{3.37}$$

for $y \neq x$ and $v \neq u$, where x and y label values of $f(t)$, and u and v label values of $s(t)$. $W_s(v|u, \Delta t)$ is the probability that $s(t + \Delta t) = s_v$ given that $s(t) = s_u$.

If both electronic and soliton relaxation have occurred during time Δt, then $y \neq x$ and $v \neq u$, and using equations (3.15) and (3.37),

$$\begin{aligned}
\pi_{fs}(xu, yv) &= \frac{d}{d\Delta t} W_{fs}(yv|xu, \Delta t)\Big|_{\Delta t=0} \\
&= \frac{d}{d\Delta t} [W_f(y|x, \Delta t) W_s(v|u, \Delta t)]\Big|_{\Delta t=0} \\
&= [\pi_f(x, y) W_s(v|u, \Delta t) + W_f(y|x, \Delta t) \pi_s(u, v)]|_{\Delta t=0} \\
&= 2\pi_f(x, y) \pi_s(u, v) \Delta t|_{\Delta t=0} \\
&= 0.
\end{aligned}$$

If, during time Δt, only electronic relaxation has occurred, then $y \neq x$, $v = u$, and

$$\begin{aligned}
\pi_{fs}(xu, yu) &= \frac{d}{d\Delta t} [W_f(y|x, \Delta t) W_s(u|u, \Delta t)]\Big|_{\Delta t=0} \\
&= [\pi_f(x, y)\,(1 + \pi_s(u, u)\Delta t) + \pi_f(x, y) \Delta t \pi_s(u, u)]|_{\Delta t=0} \\
&= \pi_f(x, y)\,.
\end{aligned}$$

Likewise for $v \neq u$, $\pi_{fs}(xv, xu) = \pi_s(u, v)$. By equation (3.17), the diagonal elements of π_{fs} are

$$\pi_{fs}(xu, xu) = -\sum_{yv \neq xu} \pi_{fs}(xu, yv)\,. \tag{3.38}$$

The combined relaxation matrix $\boldsymbol{\pi}$ has the form given in table 3.2. The elements π_f of $\boldsymbol{\pi}_{fs}$ are given by equations 3.28 and 3.30, π_s is the soliton relaxation rate , and Σ is the negative of the sum over the row of the off-diagonal elements of $\boldsymbol{\pi}_{fs}$, given by equation (3.38).

$xu\backslash yv$	11	21	31	12	22	32
11	Σ	π_f	π_f	π_s	0	0
21	π_f	Σ	π_f	0	π_s	0
31	π_f	π_f	Σ	0	0	π_s
12	π_s	0	0	Σ	π_f	π_f
22	0	π_s	0	π_f	Σ	π_f
32	0	0	π_s	π_f	π_f	Σ

Table 3.2: The form of the combined relaxation matrix.

In fitting Mössbauer spectra of $NH_4Co_{1-x}Fe_xCl_3$ and $CsCo_{1-x}Fe_xCl_3$, the combined relaxation model is the same as the 3–level relaxation model, except in the sites in frustrated chains, which occur between T_{N_2} and T_{N_1}. In these sites, both soliton and electronic relaxation are assumed to occur independently, and the lineshape for these sites is calculated according to the above theory. I wrote a program called SOEL (SOliton and ELectronic relaxation) which incorporates combined relaxation for the frustrated sites. For spectra without frustrated sites, that is, at temperatures below T_{N_2} and for the 3–dimensional sites between T_{N_2} and T_{N_1}, SOEL operates exactly the same as THREL.

3.5 The Fe^{2+} Electronic Hamiltonian and Mössbauer Parameters.

In this section the procedure is outlined for obtaining the crystal field, spin–orbit, and magnetic exchange parameters for the electronic Hamiltonian of Fe^{2+} in $CsCo_{1-x}Fe_xCl_3$ and $NH_4Co_{1-x}Fe_xCl_3$. The eigenstates of the electronic Hamiltonian are used to calculate the Mössbauer parameter, quadrupole splitting. The crystal field and spin–orbit parameters are then varied so that a least–squares fit to the experimental quadrupole splitting data can be obtained for temperatures above T_{N_1}.

The Fe^{2+} ion substitutes for the Co^{2+} ion into sites with point symmetries of $\bar{3}m$ and $3m$ for $CsCoCl_3$ and NH_4CoCl_3 respectively. The crystal field at the Fe^{2+} site

must be invariant under the symmetry operations of the local point symmetry, so that at temperatures above T_{N_1}, where we ignore the magnetic exchange interaction, the Hamiltonian for the Fe^{2+} electrons is (Sugano *et al* 1970 p. 134, Ballhausen 1962)

$$\begin{aligned}\mathcal{H} &= \mathcal{H}_{\text{octahedral}} + \mathcal{H}_{\text{trigonal}} + \mathcal{H}_{\text{so}} \\ &= B_C^4[C_0^{(4)} + (10/7)^{1/2}(C_3^{(4)} - C_{-3}^{(4)})] + (B_0^2 C_0^{(2)} + B_0^4 C_0^{(4)}) + \lambda \boldsymbol{L}.\boldsymbol{S} \quad (3.39)\end{aligned}$$

Here $\mathcal{H}_{\text{so}}$ is the spin-orbit Hamiltonian with spin-orbit parameter λ, B_C^4 is the cubic crystal field parameter, and B_0^2 and B_0^4 are the trigonal and second order axial crystal field parameters respectively. The normalised spherical harmonic operators are defined by Sugano *et al* (1970 p.7) as $C_m^{(k)}(\theta,\phi) = [4k/(2k+1)]^{1/2} Y_{km}(\theta,\phi)$. The Y_{km} are the usual spherical harmonics.

The electronic ground term of a free Fe^{2+} ion is ^5D, derived from the electronic configuration $[Ar]3d^6$. The five orbital states appropriate to trigonal symmetry are (Sugano *et al* 1970, p.132)

$$x_+ = -(2/3)^{1/2} Y_2^{-2} - (1/3)^{1/2} Y_2^1 \qquad x_0 = Y_2^0$$

$$x_- = (2/3)^{1/2} Y_2^2 - (1/3)^{1/2} Y_2^{-1}$$

$$u_+ = -(1/3)^{1/2} Y_2^{-2} + (2/3)^{1/2} Y_2^1 \qquad u_- = (1/3)^{1/2} Y_2^2 + (2/3)^{1/2} Y_2^{-1} \,. \quad (3.40)$$

These orbital states are multiplied by the five spin states for $S = 2$, namely $|m_s\rangle$, where $m_s = -2, ..., 2$, giving a basis of 25 states. $\mathcal{H}$ is diagonalised in this basis, yielding the eigenstates and eigenvalues of $\mathcal{H}$. The quadrupole splitting QS is then calculated according to equation (1.5).

In this equation V_{zz} is the z principal component of the second derivative of the electric potential at the $^{57}Fe^{2+}$ nucleus. There are two contributions to V_{zz},

$$V_{zz} = V_{zz}^{\text{val}} + V_{zz}^{\text{lat}} \,. \quad (3.41)$$

V_{zz}^{lat} is the contribution due to the rest of the crystal, primarily the neighbouring ions, and is assumed to be independent of temperature. V_{zz}^{val} is the contribution from the valence electrons of the Fe^{2+} ion. It varies with temperature depending on the occupation of the electronic states.

$$V_{zz}^{\text{val}} = \frac{1}{42\pi\varepsilon_0} |e| \left\langle r_Q^{-3} \right\rangle \left\langle 3L_z^2 - L(L+1) \right\rangle \quad (3.42)$$

where the expectation value $\langle O \rangle$ of an operator O refers to the average over the thermally populated eigenstates of the Fe^{2+} Hamiltonian (equation (3.39)).

$$\langle O \rangle = \frac{\sum_i \langle \psi_i | O | \psi_i \rangle \exp(-E_i/kT)}{\sum_j \exp(-E_j/kT)} \tag{3.43}$$

where E_i is the eigenvalue corresponding to the eigenvector $|\psi_i\rangle$ of the electronic Hamiltonian. In using expectation values in equation (3.42) it has been assumed that the time that the Fe^{2+} ion spends in each state is much less than the ^{57}Fe nuclear precession period. This assumption is justified by the trend in the relaxation rates shown in sections 4.2.2 and 4.3. The parameter $\left\langle r_Q^{-3} \right\rangle$ is related to the free ion value of the expectation value of r^{-3}, $\left\langle r_{\text{free}}^{-3} \right\rangle$, by the Sternheimer shielding factor R_Q; $\left\langle r_Q^{-3} \right\rangle = (1 - R_Q) \left\langle r_{\text{free}}^{-3} \right\rangle$. The Sternheimer shielding factor allows for the polarisation of the $[Ar]3d^6$ configuration, which destroys the spherical symmetry of the free ion (Watson and Freeman 1963).

The temperature variation of the quadrupole splitting at temperatures above T_{N_1} was fitted using an iterative least-squares computer program described in Pollard *et al* (1982), which optimised the values of the crystal field parameters B_C^4, B_0^2, B_0^4, and λ, V_{zz}^{lat}, and $\left\langle r_Q^{-3} \right\rangle$.

The magnetic hyperfine field $\boldsymbol{B}_{\text{hf}}$ for each eigenstate of Hamiltonian (3.39) is given by (Ingalls 1971)

$$\begin{aligned} \boldsymbol{B}_{\text{hf}} &= \boldsymbol{B}_{\text{S}} + \boldsymbol{B}_{\text{L}} + \boldsymbol{B}_{\text{D}} \\ &= (1/2)B_c\langle \boldsymbol{S} \rangle + (\mu_0\mu_{\text{B}}/2\pi)\langle r^{-3} \rangle \langle \boldsymbol{L} \rangle \\ &\quad + (\mu_0\mu_{\text{B}}/84\pi)\langle r^{-3} \rangle \left\langle \left[\frac{3}{2}[\boldsymbol{L}(\boldsymbol{L}.\boldsymbol{S}) + (\boldsymbol{L}.\boldsymbol{S})\boldsymbol{L}] - L(L+1)\boldsymbol{S} \right] \right\rangle , \end{aligned} \tag{3.44}$$

where here the expectation value of operator O, $\langle O \rangle$, refers to a particular eigenstate of Fe^{2+}. $\boldsymbol{B}_{\text{S}}$ is the Fermi contact term arising from polarisation of the inner s electrons by exchange interaction with the 3d electrons. B_c is the Fermi contact effective field, and $\boldsymbol{S}$ is the ionic spin. $\boldsymbol{B}_{\text{L}}$ and $\boldsymbol{B}_{\text{D}}$ are the orbital and dipolar contributions to $\boldsymbol{B}_{\text{hf}}$. The parameter $\langle r^{-3} \rangle$ is assumed to be the same for both $\boldsymbol{B}_{\text{L}}$ and $\boldsymbol{B}_{\text{D}}$. $\langle r^{-3} \rangle$ is reduced from the free ion value for this interaction of $\langle r_{\text{free}}^{-3} \rangle$=4.59 au (Watson and Freeman (1967)). The parameter $\langle r^{-3} \rangle$ does not necessarily have the same value as $\langle r_Q^{-3} \rangle$ since they parameterise different interactions.

Below T_{N_1}, the Fe^{2+} ion is considered to be in the effective magnetic exchange

field of its Co^{2+} ion neighbours. The Fe^{2+} electronic Hamiltonian is then

$$\mathcal{H} = \mathcal{H}_{\text{octahedral}} + \mathcal{H}_{\text{trigonal}} + \mathcal{H}_{\text{so}} + \mathcal{H}_{\text{exch}} \tag{3.45}$$

with

$$\mathcal{H}_{\text{exch}} = -J_{\text{eff}}\langle S_{\text{Co}}\rangle[\sin\theta_{\text{ex}}(\cos\phi_{\text{ex}}S_x + \sin\phi_{\text{ex}}S_y) + \cos\theta_{\text{ex}}S_z]\,. \tag{3.46}$$

Here, $\langle S_{\text{Co}}\rangle$ is the thermal average of the host spin. θ_{ex} and ϕ_{ex} are the polar and azimuthal angles respectively of the mean field of the Fe^{2+} neighbours relative to the c–axis of the crystal. J_{eff} is the effective exchange constant, and $S_{x,y,z}$ are the x, y, and z components of the spin $\boldsymbol{S}$ of the Fe^{2+} ion.

In the case of the Ising–like $CsCo_{1-x}Fe_xCl_3$ and $NH_4Co_{1-x}Fe_xCl_3$, the Co^{2+} spin is along the z axis, so $\theta_{\text{ex}} = 0$. $\mathcal{H}_{\text{exch}}$ reduces to

$$\mathcal{H}_{\text{exch}} = -J_{\text{eff}}\langle S_{\text{Co}}\rangle S_z\,, \tag{3.47}$$

The spin interactions within the ground doublet of Co^{2+} in $CsCo_{1-x}Fe_xCl_3$ are well approximated if the true spin S=3/2 is replaced by the effective spin $S = 1/2$ (Tellenbach 1978). Thus $\langle S_{\text{Co}}\rangle$ is given by the S=1/2 Brillouin function (Kittel 1976).

3.6 Mössbauer Line Intensities for a Preferentially Oriented Powder.

The departure of the ratio of the intensities of the quadrupole split absorption lines of $CsCo_{1-x}Fe_xCl_3$, $NH_4Co_{1-x}Fe_xCl_3$, and NH_4FeCl_3 from the value of 1 for a randomly oriented powder (Wertheim 1964) is expected to be due to preferential orientation of the crystallites in the powder. This preferential orientation, due to the crystals cleaving easily in planes parallel to the crystallographic c axis, has been observed in crystals having similar structure (Baines *et al* 1983, Putnik *et al* 1976, Euler *et al* 1978) and in previous work in this laboratory (Ward *et al* 1987).

Firstly the angular dependence of absorption of gamma rays by the ^{57}Fe nucleus in a single crystal is calculated for the situation of the nuclear Hamiltonian commuting with itself, i.e., $[\mathcal{H}(0), \mathcal{H}(t)] = 0$. This situation is that of equation 3.6, and of all Hamiltonians which are independent of time.

Consider a gamma-ray with wave-vector $\boldsymbol{k}$ and polarisation λ, causing a transition from the nuclear ground state $|\phi_{\rm g}(i)\rangle$ to the first excited state $|\phi_{\rm e}(j)\rangle$. For transverse electromagnetic radiation the polarisation vectors

$$\begin{aligned} \hat{\boldsymbol{\varepsilon}}_{k1} &= \hat{\boldsymbol{k}} \times \hat{\boldsymbol{z}} \\ \text{and} \qquad \hat{\boldsymbol{\varepsilon}}_{k2} &= \hat{\boldsymbol{k}} \times \hat{\boldsymbol{\varepsilon}}_{k1} \end{aligned} \tag{3.48}$$

can be constructed. Weissbluth (1978) p.495 gives the relative absorption probability for a general plane wave with polarisation vector $\hat{\boldsymbol{\varepsilon}}_{k\lambda}$ as

$$P(\boldsymbol{k},\lambda;i,j) = |\langle\phi_{\rm e}(j)|\hat{\boldsymbol{\varepsilon}}_{k\lambda}.\boldsymbol{p}\exp(i\boldsymbol{k}.\boldsymbol{r})|\phi_{\rm g}(i)\rangle|^2 \ .$$

The magnetic dipole (M1) component of $\hat{\boldsymbol{\varepsilon}}_{k\lambda}.\boldsymbol{p}\exp(i\boldsymbol{k}.\boldsymbol{r})$ is of the form $\hat{\boldsymbol{k}} \times \hat{\boldsymbol{\varepsilon}}_{k\lambda}.\boldsymbol{\mu}$ where $\boldsymbol{\mu}$ is the magnetic moment operator. Since $\hat{\boldsymbol{k}}$, $\hat{\boldsymbol{\varepsilon}}_{k1}$, and $\hat{\boldsymbol{\varepsilon}}_{k2}$ form a right-handed set, within the modulus squared the absorption probability is

$$P(\boldsymbol{k},\lambda;i,j) = |\langle\phi_{\rm e}(j)|\hat{\boldsymbol{\varepsilon}}_{k\lambda}.\boldsymbol{\mu}|\phi_{\rm g}(i)\rangle|^2 \ . \tag{3.49}$$

Expressing the nuclear states ϕ in terms of the complete set of eigenfunctions $\psi(I,m_I)$ of the angular momentum operators $\boldsymbol{I}^2$, and I_z, the absorption probability is

$$P(\boldsymbol{k},\lambda;i,j) = \left|\langle\sum_{m_j} a_{j,m_j}\psi(\tfrac{3}{2},m_j))|\hat{\boldsymbol{\varepsilon}}_{k\lambda}.\boldsymbol{\mu}|\sum_{m_i} b_{i,m_i}\psi(\tfrac{1}{2},m_i)\rangle\right|^2 \ .$$

Changing from the Cartesian basis to the standard spherical basis given in Weissbluth (1978),

$$\hat{\boldsymbol{\varepsilon}}_{k\lambda}.\boldsymbol{\mu} = \sum_q \varepsilon^*_{q\lambda}\mu^{(1)}_q$$

where $q = +,0,-$ and the components (μ_+, μ_0, μ_-) of $\mu^{(1)}_q$ are given in terms of the components of the Cartesian basis by

$$\mu_\pm = \mp\frac{1}{\sqrt{2}}(\mu_x \pm i\mu_y), \qquad \mu_0 = \mu_z \tag{3.50}$$

The $\varepsilon_{q\lambda}$ are the standard components of the circular polarisation vector, which relate to the components of the linear polarisation vector in the same way as the components of $\mu^{(1)}_q$ relate to $\mu_{x,y,z}$, given by equations (3.50).

Substituting for $\hat{\boldsymbol{\varepsilon}}_{k\lambda}.\boldsymbol{\mu}$, the relative transition probability is expressed as matrix elements of the irreducible tensor operators $\mu^{(1)}_q$

$$P(\boldsymbol{k},\lambda;i,j) = \left|\sum_q \varepsilon^*_{q\lambda}\langle\sum_{m_j} a_{j,m_j}\psi(\tfrac{3}{2},m_j))|\mu^{(1)}_q|\sum_{m_i} b_{i,m_i}\psi(\tfrac{1}{2},m_i)\rangle\right|^2 \ .$$

Applying the Wigner Eckhart theorem (Weissbluth 1978, p.159), the relative absorption probability can be factored into symmetry dependent and independent parts.

$$P(\boldsymbol{k},\lambda;i,j) = \left| \sum_{m_i,m_j,q} a^*_{j,m_j} b_{i,m_i} (-1)^{\frac{3}{2}-m_j} \begin{pmatrix} \frac{3}{2} & 1 & \frac{1}{2} \\ -m_j & q & m_i \end{pmatrix} \varepsilon^*_{q\lambda} \right|^2 \times \left| \langle \tau, \tfrac{3}{2} || \mu^{(1)} || \tau', \tfrac{1}{2} \rangle \right|^2 , \tag{3.51}$$

where the $\begin{pmatrix} \frac{3}{2} & 1 & \frac{1}{2} \\ -m_j & q & m_i \end{pmatrix}$ are 3-j symbols. The reduced matrix element $\langle \tau, \frac{3}{2} || \mu^{(1)} || \tau', \frac{1}{2} \rangle$ is independent of symmetry, so the angular dependence of the relative absorption probability is given by the first factor in equation (3.51). τ and τ' symbolize the totality of all quantum numbers apart from I and m_I necessary to specify the eigenstates of the system completely. The Wigner Eckhart theorem also gives the condition on q, $m_j = m_i + q$. Expanding P for the three values of q,

$$P(\boldsymbol{k},\lambda;i,j) = \left| A\varepsilon^*_{-1\lambda} + B\varepsilon^*_{0\lambda} + C\varepsilon^*_{1\lambda} \right|^2 , \tag{3.52}$$

where A, B, and C are calculated from 3-j symbols (Rotenberg *et. al.* 1959) to be

$$\begin{aligned} A &= \sqrt{\frac{1}{12}} a^*_{j,-\frac{1}{2}} b_{i,\frac{1}{2}} + \frac{1}{2} a^*_{j,-\frac{3}{2}} b_{i,-\frac{1}{2}} , \\ B &= \sqrt{\frac{1}{6}} a^*_{j,\frac{1}{2}} b_{i,\frac{1}{2}} + \sqrt{\frac{1}{6}} a^*_{j,-\frac{1}{2}} b_{i,-\frac{1}{2}} , \\ C &= \frac{1}{2} a^*_{j,\frac{3}{2}} b_{i,\frac{1}{2}} + \sqrt{\frac{1}{12}} a^*_{j,\frac{1}{2}} b_{i,-\frac{1}{2}} . \end{aligned} \tag{3.53}$$

Substituting for the $\varepsilon_{q\lambda}$ in terms of the Cartesian components of $\hat{\boldsymbol{\varepsilon}}_{\boldsymbol{k}\lambda}$,

$$\begin{aligned} P(\boldsymbol{k},\lambda;i,j) \propto & \left| A(\varepsilon_{x\lambda} + i\varepsilon_{y\lambda}) + \sqrt{2}B\varepsilon_{z\lambda} - C(\varepsilon_{x\lambda} - \varepsilon_{y\lambda}) \right|^2 \\ = & (A^*A + C^*C)(\varepsilon^2_{x\lambda} + \varepsilon^2_{y\lambda}) + 2B^*B\varepsilon^2_{z\lambda} \\ & + 2\sqrt{2} Re\{A^*B(\varepsilon_{x\lambda}\varepsilon_{z\lambda} - i\varepsilon_{y\lambda}\varepsilon_{z\lambda})\} \\ & + 2Re\{A^*C(\varepsilon^2_{x\lambda} - 2i\varepsilon_{x\lambda}\varepsilon_{y\lambda} - \varepsilon^2_{y\lambda})\} \\ & - 2\sqrt{2} Re\{B^*C(\varepsilon_{z\lambda}\varepsilon_{x\lambda} - i\varepsilon_{z\lambda}\varepsilon_{y\lambda})\} . \end{aligned} \tag{3.54}$$

For a gamma-ray with wave-vector $\boldsymbol{k}$ at polar angles (α, β) relative to the princi-

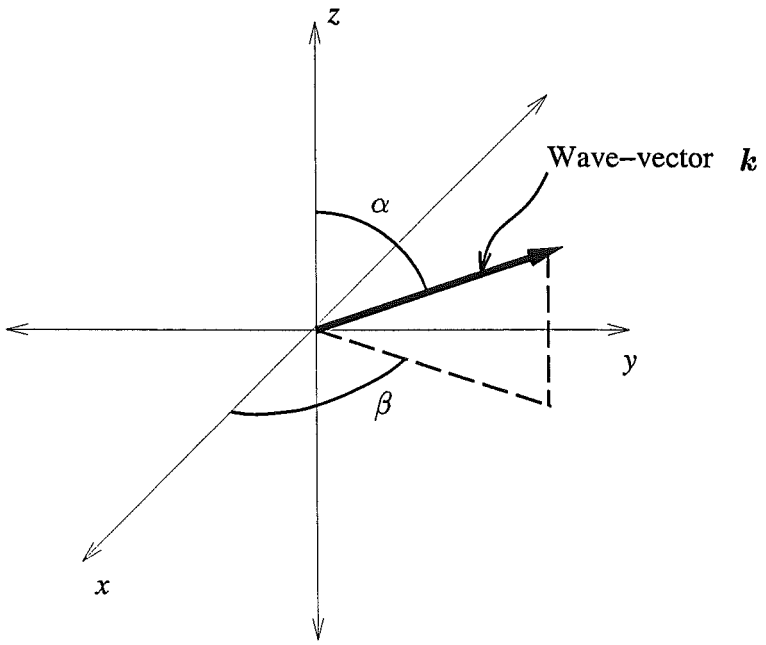

Figure 3.1: The angles defined by the wave-vector relative to the principal axes of the EFG tensor.

pal axes of the electric field gradient tensor, as shown in figure 3.1, the components of $\boldsymbol{k}$ in the principal axis system are

$$\hat{\boldsymbol{k}} = \begin{pmatrix} \sin\alpha\cos\beta \\ \sin\alpha\sin\beta \\ \cos\alpha \end{pmatrix}$$

so one polarisation vector is given by

$$\hat{\boldsymbol{\epsilon}}_{k1} = \hat{\boldsymbol{k}} \times \hat{z} = \begin{pmatrix} \sin\beta \\ -\cos\beta \\ 0 \end{pmatrix}, \tag{3.55}$$

and the other is

$$\hat{\boldsymbol{\epsilon}}_{k2} = \hat{\boldsymbol{k}} \times \hat{\boldsymbol{\epsilon}}_{k1} = \begin{pmatrix} \cos\alpha\cos\beta \\ \cos\alpha\sin\beta \\ -\sin\alpha \end{pmatrix}. \tag{3.56}$$

The relative absorption probability is averaged over both polarisations. For the $\hat{\boldsymbol{\epsilon}}_{k1}$ polarisation,

$$P(\boldsymbol{k},1;i,j) = (A^*A + C^*C) - 2Re\{A^*C(\sin^2\beta + 2i\sin\beta\cos\beta - \cos^2\beta)\}. \tag{3.57}$$

For the $\hat{\boldsymbol{\varepsilon}}_{\boldsymbol{k}2}$ polarisation,

$$\begin{aligned} P(\boldsymbol{k},2;i,j) = & (A^*A + C^*C)\cos^2\alpha + 2B^*B\sin^2\alpha \\ & +2\sqrt{2}Re\{A^*B(-\cos\alpha\sin\alpha\cos\beta + i\cos\alpha\sin\alpha\sin\beta)\} \\ & -2Re\{A^*C(\cos^2\alpha\cos^2\beta - 2i\cos^2\alpha\cos\beta\sin\beta - \cos^2\alpha\sin^2\beta)\} \\ & -2\sqrt{2}Re\{B^*C(-\sin\alpha\cos\alpha\cos\beta + i\sin\alpha\cos\alpha\sin\beta)\}\,. \end{aligned} \tag{3.58}$$

The addition of equations (3.57) and (3.58) yields the relative absorption probability for a gamma ray:

$$\begin{aligned} P(\alpha,\beta;i,j) = & (A^*A + C^*C)(\cos^2\alpha + 1) + 2B^*B\sin^2\alpha \\ & -\sqrt{2}Re\{A^*B\sin 2\alpha\exp(-i\beta)\} \\ & +2Re\{A^*C\sin^2\alpha\exp(-2i\beta)\} \\ & +\sqrt{2}Re\{B^*C\sin 2\alpha\exp(-i\beta)\}\,, \end{aligned} \tag{3.59}$$

where the wave–vector $\boldsymbol{k}$ and the now redundant polarisation labels λ of P have been replaced by the polar angles (α,β) of the wave–vector relative to the principal axes of the EFG tensor.

In the case of a preferentially oriented powder, the relative absorption probability $P(i,j)$ is given by the average of equation (3.59) over the orientations of each crystallite in the absorber.

$$\begin{aligned} P(i,j) &= < P(\alpha,\beta;i,j) >_{\mathrm{av}} \\ &= \int_{\alpha=0}^{\pi}\int_{\beta=0}^{2\pi} g(\alpha,\beta)P(\alpha,\beta;i,j)\sin\alpha\, d\alpha\, d\beta\,. \end{aligned} \tag{3.60}$$

Assuming that the distribution function $g(\alpha,\beta)$ has cylindrical symmetry about the z–axis, the relative absorption probability is

$$P(i,j) = (|A|^2 + |C|^2)(2 - < \sin^2\alpha >_{\mathrm{av}}) + 2|B|^2 < \sin^2\alpha >_{\mathrm{av}}\,. \tag{3.61}$$

For the case when $[\mathcal{H}(0),\mathcal{H}(t)] \neq 0$ the lineshape given by equation (3.24) involves two matrix elements of the Hamiltonian describing the interaction between the nucleus and radiation,

$$DMM(\alpha,\beta;m_0,m_1;m_0',m_1') \equiv \langle I_1 m_1|\mathcal{H}^-|I_0 m_0\rangle\langle I_0 m_0'|\mathcal{H}^+|I_1 m_1'\rangle\,. \tag{3.62}$$

For a preferentially oriented powder, the desired quantity is the average of DMM over the distribution of orientations (α,β) in the powder.

For a single crystal absorbing a gamma–ray with wave–vector $\boldsymbol{k}$ relative to the axis of quantisation, $|\mathcal{H}^-\mathcal{H}^+|$ is given by equation (3.49), so

$$DMM(\boldsymbol{k},\lambda;m_0,m_1;m_0',m_1') = \langle I_1 m_1|\hat{\boldsymbol{\varepsilon}}_{\boldsymbol{k}\lambda}.\boldsymbol{\mu}|I_0 m_0\rangle\langle I_0 m_0'|[\hat{\boldsymbol{\varepsilon}}_{\boldsymbol{k}\lambda}.\boldsymbol{\mu}]^\dagger|I_1 m_1'\rangle\,.$$

The M1 operator $\hat{\boldsymbol{\varepsilon}}_{\boldsymbol{k}\lambda}.\boldsymbol{\mu}$ is Hermitian, so DMM is

$$\begin{aligned} DMM(\boldsymbol{k},\lambda;m_0,m_1;m_0',m_1') &= \langle I_1 m_1|\hat{\boldsymbol{\varepsilon}}_{\boldsymbol{k}\lambda}.\boldsymbol{\mu}|I_0 m_0\rangle\langle I_1 m_1'|\hat{\boldsymbol{\varepsilon}}_{\boldsymbol{k}\lambda}.\boldsymbol{\mu}|I_0 m_0'\rangle^* \\ &\equiv M(\alpha,\beta;m_0,m_1)M^*(\alpha,\beta;m_0',m_1')\,. \end{aligned}$$

Making the trivial expansion of the kets,

$$\begin{aligned} &|I_0 m_0\rangle = \textstyle\sum_{m_i}\delta_{m_0 m_i}\psi(\frac{1}{2},m_i) \\ \text{and}\qquad &|I_1 m_1\rangle = \textstyle\sum_{m_j}\delta_{m_1 m_j}\psi(\frac{3}{2},m_j) \end{aligned}$$

enables the theory developed in equations (3.51) to (3.53) to be used by replacing b_{i,m_i} and a_{j,m_j} with $\delta_{m_0 m_i}$ and $\delta_{m_1 m_j}$. Thus

$$\begin{aligned} M(\alpha,\beta;m_0,m_1) &= \varepsilon^*_{q\lambda}\textstyle\sum_{m_i,m_j,q}\delta_{m_0,m_i}\delta_{m_1,m_j}(-1)^{\frac{3}{2}-m_j}\begin{pmatrix}\frac{3}{2} & 1 & \frac{1}{2}\\ -m_j & q & m_i\end{pmatrix} \\ &= A\varepsilon^*_{-1\lambda} + B\varepsilon^*_{0\lambda} + C\varepsilon^*_{1\lambda} \end{aligned} \tag{3.63}$$

where the A, B, and C are given in equation (3.53) with the a's and b's replaced as above. Likewise, defining A', B', and C' the same as A, B, and C, but with m_0' and m_1' replacing m_0 and m_1 respectively,

$$M^*(\alpha,\beta;m_0',m_1') = A'\varepsilon_{-1\lambda} + B'\varepsilon_{0\lambda} + C'\varepsilon_{1\lambda}\,, \tag{3.64}$$

so, calculating MM^*, and substituting for the $\varepsilon_{q\lambda}$ in terms of the Cartesian components of $\hat{\boldsymbol{\varepsilon}}_{\boldsymbol{k}\lambda}$,

$$\begin{aligned} DMM(\boldsymbol{k},\lambda;m_0,m_1;m_0',m_1') \propto\ & (AA'+CC')(\varepsilon^2_{x\lambda}+\varepsilon^2_{y\lambda}) + 2BB'\varepsilon^2_{z\lambda} \\ & +\sqrt{2}AB'(\varepsilon_{x\lambda}+i\varepsilon_{y\lambda})\varepsilon_{z\lambda} + \sqrt{2}BA'(\varepsilon_{x\lambda}-i\varepsilon_{y\lambda})\varepsilon_{z\lambda} \\ & -AC'(\varepsilon_{x\lambda}+i\varepsilon_{y\lambda})^2 - CA'(\varepsilon_{x\lambda}-i\varepsilon_{y\lambda})^2 \\ & -\sqrt{2}BC'(\varepsilon_{x\lambda}+i\varepsilon_{y\lambda})\varepsilon_{z\lambda} - \sqrt{2}CB'(\varepsilon_{x\lambda}-i\varepsilon_{y\lambda})\varepsilon_{z\lambda} \end{aligned}$$

For the $\hat{\boldsymbol{\varepsilon}}_{\boldsymbol{k}1}$ polarisation,

$$\begin{aligned} DMM(\boldsymbol{k},1;m_0,m_1;m_0',m_1') = \ & (AA'+CC') \\ & AC'(\sin\beta - i\cos\beta)^2 - CA'(\sin\beta + i\cos\beta)^2 \end{aligned}$$

and for the $\hat{\boldsymbol{\varepsilon}_{k2}}$ polarisation,

$$\begin{aligned}DMM(\boldsymbol{k},2;m_0,m_1;m_0',m_1') &= (AA'+CC')\cos^2\alpha + 2BB'\sin^2\alpha \\ &-\sqrt{2}AB'\cos\alpha\sin\alpha(\cos\beta+i\sin\beta) - \sqrt{2}BA'\sin\alpha\cos\alpha(\cos\beta-i\sin\beta) \\ &-AC'\cos^2\alpha(\cos\beta+i\sin\beta)^2 - CA'\cos^2\alpha(\cos\beta-i\sin\beta) \\ &+\sqrt{2}BC'\sin\alpha\cos\alpha(\cos\beta+i\sin\beta) + \sqrt{2}CB'\cos^2\alpha(\cos\beta-i\sin\beta)\end{aligned}$$

Adding the contributions from the two polarisations,

$$\begin{aligned}DMM(\alpha,\beta;m_0,m_1;m_0',m_1') &= (AA'+CC')(2-\sin^2\alpha) + 2BB'\sin^2\alpha \\ &-\tfrac{1}{\sqrt{2}}AB'\sin 2\alpha\exp(i\beta) - \tfrac{1}{\sqrt{2}}BA'\sin 2\alpha\exp(-i\beta) \\ &+AC'\sin^2\alpha\exp(2i\beta) + CA'\sin^2\alpha\exp(-2i\beta) \\ &+\tfrac{1}{\sqrt{2}}BC'\sin 2\alpha\exp(i\beta) + \tfrac{1}{\sqrt{2}}CB'\sin 2\alpha\exp(-i\beta)\,.\end{aligned} \tag{3.65}$$

The A, B, and C coefficients are given for the different nuclear transitions in table 3.3.

Transition $m_i \rightarrow m_j$		A	B	C
$-\frac{1}{2}$	$-\frac{3}{2}$	$\sqrt{\frac{3}{12}}$	0	0
$-\frac{1}{2}$	$-\frac{1}{2}$	0	$\sqrt{\frac{2}{12}}$	0
$-\frac{1}{2}$	$\frac{1}{2}$	0	0	$\sqrt{\frac{1}{12}}$
$-\frac{1}{2}$	$\frac{3}{2}$	0	0	0
$\frac{1}{2}$	$-\frac{3}{2}$	0	0	0
$\frac{1}{2}$	$-\frac{1}{2}$	$\sqrt{\frac{1}{12}}$	0	0
$\frac{1}{2}$	$\frac{1}{2}$	0	$\sqrt{\frac{2}{12}}$	0
$\frac{1}{2}$	$\frac{3}{2}$	0	0	$\sqrt{\frac{3}{12}}$

Table 3.3: Line intensity coefficients in equations (3.63) and (3.64), calculated from 3-j symbols.

In the case of a powder with preferential orientation, equation (3.65) is averaged by following the procedure of equation (3.60). For cylindrical symmetry

$$DMM(m_0,m_1;m_0',m_1') = (AA'+CC')(2-<\sin^2\alpha>_{\rm av}) + 2BB'<\sin^2\alpha>_{\rm av}\,. \tag{3.66}$$

A computer program which calculated the lineshape for a random powder with relaxation of the electric and magnetic hyperfine fields along arbitrary axes was

obtained from the University of Liverpool Oliver Lodge laboratory. . The computer code was altered to calculate the lineshape for a preferentially oriented powder.

For Mössbauer spectra of non–magnetic single crystals the ratio of the quadrupole split line intensities for the nuclear transitions between $m_I = \pm\frac{1}{2} \rightarrow \pm\frac{1}{2}$ and $m_I = \pm\frac{1}{2} \rightarrow \pm\frac{3}{2}$ states (see figure 1.4) is given by Wertheim (1964) as

$$\frac{I_{\rightarrow\pm\frac{1}{2}}}{I_{\rightarrow\pm\frac{3}{2}}} = \frac{1 + \frac{3}{2}\sin^2\alpha}{\frac{3}{2}(1 + \cos^2\alpha)} \tag{3.67}$$

where α is the angle between the z principal axis of the EFG tensor and the incoming gamma–ray. For a powder with preferential orientation,

$$x \equiv \frac{I_{\rightarrow\pm\frac{1}{2}}}{I_{\rightarrow\pm\frac{3}{2}}} = \frac{1 + \frac{3}{2} < \sin^2\alpha >_{\text{av}}}{\frac{3}{2}(2 - < \sin^2\alpha >_{\text{av}})} \tag{3.68}$$

where $< \sin^2\alpha >_{\text{av}}$ is the average of $\sin^2\alpha$ over the orientations α for each crystallite in the absorber (see section 3.6, page 50).

Rearranging equation (3.68),

$$< \sin^2\alpha >_{\text{av}} = \frac{6x - 2}{3x + 3}\,. \tag{3.69}$$

Putting $\alpha = 90°$ into equation (3.67), the ratio of the line intensities is

$$\frac{I_{\rightarrow\pm\frac{1}{2}}}{I_{\rightarrow\pm\frac{3}{2}}} = \frac{5}{3}\,, \tag{3.70}$$

whereas this ratio is 1/3 for $\alpha = 0$. Equation (3.70) indicates, for a powder with preferential orientation towards $\alpha = 90°$, that the $I_{\rightarrow\pm\frac{1}{2}}$ absorption line will be more intense than the $I_{\rightarrow\pm\frac{3}{2}}$ line.

For Fe^{2+} in $NH_4Co_{1-x}Fe_xCl_3$ and $CsCo_{1-x}Fe_xCl_3$, the energy shift E_Q caused by the electric quadrupole interaction between the nucleus and the EFG tensor is given by equation (1.4). Evaluating E_{m_I} for the nuclear $\pm\frac{3}{2}$ and $\pm\frac{1}{2}$ substates yields

$$E_{\pm\frac{3}{2}} = \frac{|e|QV_{zz}}{4}\,,$$

$$\text{and} \qquad E_{\pm\frac{1}{2}} = -\frac{|e|QV_{zz}}{4}\,.$$

This means that in the absence of magnetic fields, for $V_{zz} < 0$ (and $Q = 0.21 \times 10^{-28}$ m$^2 > 0$), the transition drawn in figure 1.4 to the $m_I = \pm 3/2$ states has

a lower energy than the transition to the $m_I = \pm 1/2$ states. Thus for a powder absorber with preferential orientation towards $\alpha = 90°$, if the more intense QS absorption line is at higher energy, then $V_{zz} < 0$.

The value of $< \sin^2 \alpha >_{\rm av}$ for a particular absorber was determined from the ratio of the line intensities of spectra taken above $T_{\rm N_1}$. When fitting spectra taken at temperatures below $T_{\rm N_1}$, $< \sin^2 \alpha >_{\rm av}$ was fixed to the value determined from spectra above $T_{\rm N_1}$.

3.7 Iron–Soliton Interaction

The 2–level and 3–level relaxation models of sections 3.2 and 3.3 assume that all Fe^{2+} ions in the frustrated chains produce a magnetic hyperfine field $B_{\rm hf}$ at the nucleus, and that this always changes sign with the passage of a soliton.

In the combined relaxation model of section 3.4, the crystal field and magnetic exchange splittings of the Fe^{2+} ion in the frustrated chains are assumed to be the same as that for the 3-dimensionally ordered chains. In addition, soliton and electronic relaxation are assumed independent, with solitons causing a reversal of the hyperfine field only when an electronic state with $B_{\rm hf} = \pm B$ is occupied. The soliton is assumed to have no effect when an electronic state with $B_{\rm hf} = 0$ is occupied.

In this section a procedure is outlined by which one may estimate the effect on an Fe^{2+} ion of the passage of a soliton along the surrounding chain of Co^{2+} spins. The formalism is pursued up to the point where numerical values are required. Because of difficulties obtaining coefficients of fractional parentage for more–than–half–filled shells, the calculations weren't carried further.

In order to estimate the effects of soliton passage on Fe^{2+} relaxation, it was planned to use time dependent perturbation theory to calculate the soliton induced relative transition probabilities to different Fe^{2+} states, given that the initial Fe^{2+} state was occupied. The resulting relative transition probabilities could be added directly to elements of the relaxation matrix π_{fs} in section 3.4.

According to time dependent perturbation theory (Merzbacher 1970), the Hamiltonian $\mathcal{H}$ for the system (of an Fe^{2+} ion in a Co^{2+} chain) is broken up into

$$\mathcal{H} = \mathcal{H}_0 + V$$

where $\mathcal{H}_0$ describes the unperturbed system, consisting of a chain of Co^{2+} ions and an Fe^{2+} ion in the crystal field environment of the chain, but excluding the exchange interaction of the Fe^{2+} ion with its Co^{2+} neighbours in the chain, i.e.,

$$\mathcal{H}_0 = \mathcal{H}_{\text{chain}} + \mathcal{H}_{\text{Fe}} .$$

V is the interaction between the Fe^{2+} ion and the Co^{2+} chain, which we assume to be dominated by the Coulomb interaction between electrons on the Fe^{2+} ion and the electrons of the neighbours in the chain.

$$V = \sum_{i\in\text{Fe},j\in\text{Co}} \mathcal{H}_{ij} = \sum_{i\in\text{Fe},j\in\text{Co}} \frac{ke^2}{r_{ij}} .$$

Eigenstates of $\mathcal{H}_0$ are $|\Psi\rangle = |\psi_{\text{chain}}\psi_{\text{Fe}}\rangle$ where ψ_{chain} is an eigenstate of $\mathcal{H}_{\text{chain}}$, ignoring the effect of the Fe^{2+} ion on the chain, and ψ_{Fe} is an eigenstate of $\mathcal{H}_{\text{Fe}}$. The three lowest energy wavefunctions for Fe^{2+} in $NH_4Co_{1-x}Fe_xCl_3$ and $CsCo_{1-x}Fe_xCl_3$ can be obtained by diagonalizing the electronic Hamiltonian having parameters given in tables 4.5 and 4.13 respectively.

To first order in perturbation theory the probability P of a transition from state $|\Psi\rangle$ to state $|\Psi'\rangle$ is then proportional to the matrix element of the perturbation V,

$$P(\Psi \to \Psi') \propto \langle\Psi'|V|\Psi\rangle .$$

Ignoring next–nearest neighbour and longer–range interactions with the Fe^{2+} ion, matrix elements of V are well approximated if ψ_{chain} is replaced with the two neighbours of the Fe^{2+} ion, $\psi^1_{\text{Co}}\psi^2_{\text{Co}}$. Since the Coulomb operator $\mathcal{H}_{ij}$ acts between only two electrons, the ith on the Fe^{2+} ion, and the jth on *one* of the Co^{2+} ions, only matrix elements of V between pair states of the total wavefunction $|\Psi\rangle = |\psi_{\text{Co}}\psi_{\text{Fe}}\rangle$ need to be considered.

A soliton has the effect of "flipping the spin" of each Co^{2+} ion in the chain, so that, if the initial Co^{2+} wavefunction was $\psi_{\text{Co}} = \psi_+$ (the wavefunctions $\psi_\pm$ are given by Tellenbach (1978)), the Co^{2+} wavefunction after the passage of a soliton would be $\psi_{\text{Co}}{}' = \psi_-$. The probability that a transition is induced from Fe^{2+} state ψ_{Fe} to state $\psi_{\text{Fe}}{}'$ is then given by

$$P(\psi_{\text{Fe}} \to \psi_{\text{Fe}}{}') \propto \langle\psi_-\psi_{\text{Fe}}{}'|V|\psi_+\psi_{\text{Fe}}\rangle .$$

Since electrons are fermions, the total wavefunction for the Fe–Co system must be antisymmetric with respect to exchange of coordinates and spin. To express this determinantal product states are used for the total wavefunctions $|\Psi\rangle$.

$$|\Psi\rangle = \sum_{\prod} \frac{(-1)^{\prod}}{\sqrt{(N_\mathrm{A}+N_\mathrm{B})!}} \prod |\psi_{\mathrm{A}_1}(1)\psi_{\mathrm{A}_2}(2)...\psi_{\mathrm{A}_{N_\mathrm{A}}}(N_\mathrm{A})\psi_{B_1}(N_\mathrm{A}+1)...\psi_{\mathrm{B}_{N_\mathrm{B}}}(N_\mathrm{A}+N_\mathrm{B})\rangle \,.$$

Here $\psi_{\mathrm{A}_i}(j)$ is the ith 1–electron wave function (including spin) of the jth electron on atom A. The permutation operator $\prod$ covers all permutations of the electron numbers. There are N_A electrons (1–electron wavefunctions) on atom A and N_B electrons on atom B, so $1/\sqrt{(N_\mathrm{A}+N_\mathrm{B})!}$ normalises $|\Psi\rangle$.

Of interest is the interaction between the ith electron on atom A and the jth electron on atom B. Since the electrons on each atom are all equivalent,

$$\langle\Psi| \sum_{i\in\mathrm{A}\, j\in\mathrm{B}} \mathcal{H}_{ij}|\Psi'\rangle = N_\mathrm{A}N_\mathrm{B}\langle\Psi|\mathcal{H}_{11}|\Psi'\rangle \,,$$

where $\mathcal{H}_{11}$ is the interaction Hamiltonian which acts on the first electron of atom A and the first electron of atom B.

The concept of cosets (Fraleigh 1967) can be used to split the total wavefunction into a sum of permutations between the wavefunctions of Fe^{2+} and Co^{2+}.

$$|\Psi\rangle = \sum_{\prod} \frac{(-1)^{\prod}}{\sqrt{\frac{(N_\mathrm{A}+N_\mathrm{B})!}{N_\mathrm{A}!N_\mathrm{B}!}}} \prod |\psi^\mathrm{A}\rangle_\mathcal{A}|\psi^\mathrm{B}\rangle_\mathcal{A}$$

where here, $\prod$ permutes electrons between atoms A and B only. The states $|\phi^\mathrm{A}\rangle_\mathcal{A}$ and $|\psi^\mathrm{B}\rangle_\mathcal{A}$ are normalised antisymmetric N_A and N_B electron wavefunctions on atoms A and B respectively. A matrix element of the interaction Hamiltonian is then

$$\langle\Psi|\sum\mathcal{H}_{ij}|\Psi'\rangle = N_\mathrm{A}N_\mathrm{B}\langle\psi^\mathrm{A}|_\mathcal{A}\langle\psi^\mathrm{B}|_\mathcal{A}\mathcal{H}_{11}\sum_{\prod}(-1)^{\prod}\prod|\psi^{\mathrm{A}'}\rangle_\mathcal{A}|\psi^{\mathrm{B}'}\rangle_\mathcal{A} \,.$$

The permutation operator $\prod$ can be factorised into a product of two parts, $\prod_{11} \in \{1, (1,1)\}$ (where (1,1) permutes the first electron of each atom) which acts *only* on the first electron of atom A and the first electron of atom B, and $\prod'$ which contains all other possibilities for $\prod$. Since $\mathcal{H}_{11}$ acts only on the first electron of atom A and the first electron of atom B, by orthogonality of the 1–electron wavefunctions, the only non–zero matrix elements of $\langle\Psi|\sum\mathcal{H}_{ij}|\Psi'\rangle$ occur for $\prod' = 1$, the

identity operator. Thus

$$\langle\Psi|\sum\mathcal{H}_{ij}|\Psi'\rangle = N_{\rm A}N_{\rm B}\langle\psi^{\rm A}|_{\mathcal{A}}\langle\psi^{\rm B}|_{\mathcal{A}}\mathcal{H}_{11}\sum_{\Pi_{11}}(-1)^{\Pi}\Pi_{11}|\psi^{\rm A'}\rangle_{\mathcal{A}}|\psi^{\rm B'}\rangle_{\mathcal{A}}\,.$$

The first electrons from atoms A and B are decoupled using the technique of fractional parentage (Weissbluth 1978).

$$\langle\Psi|\sum\mathcal{H}_{ij}|\Psi'\rangle = N_{\rm A}N_{\rm B}\sum_{\overline{\rm A},\overline{\rm B}}\langle\psi^{\rm A}|\psi^{\overline{\rm A}},\psi_{\rm A}\rangle\langle\psi^{\rm A'}|\psi^{\overline{\rm A}'},\psi'_{\rm A}\rangle\langle\psi^{\rm B}|\psi^{\overline{\rm B}},\psi_{\rm B}\rangle\langle\psi^{\rm B'}|\psi^{\overline{\rm B}'},\psi'_{\rm B}\rangle$$

$$\times\langle\psi^{\overline{\rm A}},\psi_{\rm A}|\langle\psi^{\overline{\rm B}},\psi_{\rm B}|\mathcal{H}_{11}\sum_{\Pi_{11}}(-1)^{\Pi}\Pi_{11}|\psi^{\overline{\rm A}'},\psi'_{\rm A}\rangle|\psi^{\overline{\rm B}'},\psi'_{\rm B}\rangle$$

In this equation, $\langle\psi^{\rm A}|\psi^{\overline{\rm A}},\psi_{\rm A}\rangle$ is the coefficient of fractional parentage (cfp) for the state $|\psi^{\rm A}\rangle$. The sum is over all the parent states $\psi^{\overline{\rm A}}$, where $\overline{\rm A}\equiv N_{\rm A}-1$. $|\psi^{\overline{\rm A}},\psi_{\rm A}\rangle$ is the product of the antisymmetric $N_{\rm A}-1$ electron parent wavefunction with the 1–electron wavefunction $|\psi_{\rm A}\rangle$, and is formed by coupling the orbital and spin angular momenta of the two wavefunctions.

Since $\mathcal{H}_{11}$ acts on only the decoupled 1–electron wavefunctions, non-zero elements of $\langle\Psi|\sum\mathcal{H}_{ij}|\Psi'\rangle$ occur only if the parent wavefunctions on atom A (or B) are identical. Hence, denoting the product of two single electron wavefunctions, one on each ion, as $|\psi_{\rm A}\psi_{\rm B}\rangle$, and dropping the subscripts on $\mathcal{H}_{11}$,

$$\langle\Psi|\sum\mathcal{H}_{ij}|\Psi'\rangle = N_{\rm A}N_{\rm B}\sum_{\overline{\rm A},\overline{\rm B}}\langle\psi^{\rm A}|\psi^{\overline{\rm A}},\psi_{\rm A}\rangle\langle\psi^{\rm A'}|\psi^{\overline{\rm A}},\psi'_{\rm A}\rangle\langle\psi^{\rm B}|\psi^{\overline{\rm B}},\psi_{\rm B}\rangle\langle\psi^{\rm B'}|\psi^{\overline{\rm B}},\psi'_{\rm B}\rangle$$

$$\times\langle\psi_{\rm A}\psi_{\rm B}|\mathcal{H}\sum_{\Pi_{11}}(-1)^{\Pi}\Pi_{11}|\psi'_{\rm A}\psi'_{\rm B}\rangle$$

Since the electronic d shells are nearly filled , it is desirable to consider hole states, which makes the use of cfp's easier. The values of the coefficients of fractional parentage are tabulated in Nielson and Koster (1963).

The direct matrix elements ($\Pi_{11}=1$) of the interaction $\mathcal{H}$ are ignored, since these matrix elements represent the Coulomb interaction between neighbours in the chain, and do not cause splittings in the Fe^{2+} ion which are dependent upon which Co^{2+} wavefunction is occupied. The matrix elements which are left are of the "exchange" form $-\langle\psi_{\rm A}\psi_{\rm B}|\mathcal{H}\,\Pi|\psi'_{\rm A}\psi'_{\rm B}\rangle$, where here, Π permutes only the first electrons between each atom.

The 1–electron wavefunctions ψ comprise an orbital part ϕ and a spin part χ. The orbital part of the problem can be separated from the spin part by writing the permutation operator Π as $P_{\rm r}P_\sigma$ where $P_{\rm r}$ permutes only the orbital wavefunctions, and P_σ acts only on the spin functions. Within the space spanned by the single electron spin functions, the matrix elements of P_σ are the same as those of the Heisenberg–Dirac–van Vleck form (Weissbluth 1978, Dirac 1929) $2\boldsymbol{S}_1.\boldsymbol{S}_2 + \frac{1}{2}$, so

$$\langle\psi_{\rm A}\psi_{\rm B}|\mathcal{H}\,\Pi|\psi'_{\rm A}\psi'_{\rm B}\rangle = \langle\phi_{\rm A}\phi_{\rm B}|\mathcal{H}P_{\rm r}|\phi'_{\rm A}\phi'_{\rm B}\rangle\langle\chi_{\rm A}\chi_{\rm B}|2\boldsymbol{S}_1.\boldsymbol{S}_2 + \tfrac{1}{2}|\chi'_{\rm A}\chi'_{\rm B}\rangle\,.$$

The orbital part $\langle\phi_{\rm A}\phi_{\rm B}|\mathcal{H}|\phi'_{\rm B}\phi'_{\rm A}\rangle$, where the first orbital is on atom A, and the second on atom B in each bra/ket, is subject to the constraints of site symmetry. For the Fe–Co system in $CsCo_{1-x}Fe_xCl_3$ ($NH_4Co_{1-x}Fe_xCl_3$), there is D_{3d} (C_{3v}) symmetry about the axis along the chain.

The form of the interaction $\mathcal{H}$ is now considered. Since the distance between the intra–chain Co^{2+} ions is 3.0158 Å in $CsCo_{1-x}Fe_xCl_3$ (Soling 1968), and 3.005 Å in $NH_4Co_{1-x}Fe_xCl_3$ (Swanson *et al* 1968), the Coulomb interaction is expected to be principally via superexchange through the intermediate Cl^- ions. To avoid the complexities of a full ab-initio calculation of matrix elements of $1/r_{ij}$ (Levy 1969) between the Fe^{2+} (or Co^{2+}) and the Cl^- wavefunctions, the strategy of Bradbury and Newman (1971), and Stedman and Newman (1971) is adopted, and the angular and distance dependence of the interaction is modelled by overlap integrals. This method, the Mulliken approximation, has been successful in accounting for superexchange interactions between Gd^{3+} pairs in $LaCl_3$ and $EuCl_3$ (Bradbury and Newman 1968, 1971), and also between Ir^{4+} ions in hexachloroplatinates (Stedman and Newman 1971). In this method the full interaction $\langle\phi_{\rm A}\phi_{\rm B}|\mathcal{H}|\phi'_{\rm B}\phi'_{\rm A}\rangle$ is replaced by

$$\mathcal{E}\langle\phi_{\rm A}|\mathcal{O}|\phi'_{\rm B}\rangle\langle\phi_{\rm B}|\mathcal{O}|\phi'_{\rm A}\rangle \tag{3.71}$$

where $\mathcal{E}$ is an energy parameter to be determined from experiment.

In the case of $NH_4Co_{1-x}Fe_xCl_3$ or $CsCo_{1-x}Fe_xCl_3$ with one Cl^- ligand in the superexchange path,

$$\mathcal{O} = \sum_{T\tau} |\xi_{T\tau}\rangle\langle\xi_{T\tau}|\,.$$

$\xi_{T\tau}$ is an orbital for the Tth Cl^- ligand. This form of $\mathcal{O}$ includes "looped" interaction paths, first mentioned by Bradbury and Newman (1968), in which different ligands

are involved in the "forward" and "return" parts of equation (3.71). To proceed further requires evaluation of the overlap integrals between hole orbitals on the Fe^{2+} and Co^{2+} ions, and the hole orbitals on their Cl^- ligands.

3.8 Absorber Thickness Calculation

In an effort to determine whether the extra absorption lines in the Mössbauer spectra of one of the samples of $NH_4Co_{0.9916}Fe_{0.0084}Cl_3$ (labelled crystal B in table 2.2) were due to Fe^{2+} (instead of Co^{2+}) neighbours of the ^{57}Fe ion, a crystal with a lower ^{57}Fe concentration was grown. The concentration of ^{57}Fe in crystal C was chosen to be as low as possible within the constraints listed below:

1. Spectrum collection time t should be of the order of 1 day.
2. The signal to noise ratio S must be the same for spectra taken of both crystals.
3. The relative dip (defined below) must be approximately less than 10 % so that the absorption lines in the Mössbauer spectrum are not saturated.
4. The absorber thickness τ (including Boric acid binding agent) obeys $\tau \approx 2/\mu_e$, where μ_e is the electronic mass absorption coefficient for the absorber.
5. $\tau \approx 100$ mg.cm^{-2} so that the powder can be pressed successfully into the absorber ring, using the press as described in section 2.7.

Constraint 4 is taken from the paper of Long *et al* (1983) for the case of a thin absorber and a low background component of the Mössbauer spectrum.

The electronic mass absorption coefficient for the absorber has two contributions, one from the electronic mass absorption coefficient for $NH_4Co_{1-x}Fe_xCl_3$, μ_{Co} and the other from that of Boric acid, μ_B. Thus

$$\mu_e = F\mu_{Co} + (1 - F)\mu_B$$

where F is the fractional mass of $NH_4Co_{1-x}Fe_xCl_3$ in the absorber, and μ_{Co} and μ_B are calculated from tables in Long *et al* (1983) to be 33.5 and 1.82 cm^2.g^{-1} respectively.

Constraint 4 gives

$$\tau \approx 2/[F\mu_{\mathrm{Co}} + (1-F)\mu_{\mathrm{B}}]$$

Solving for F, and applying constraint 5, the fractional mass of $NH_4Co_{1-x}Fe_xCl_3$ in the absorber is $F \approx 0.57$.

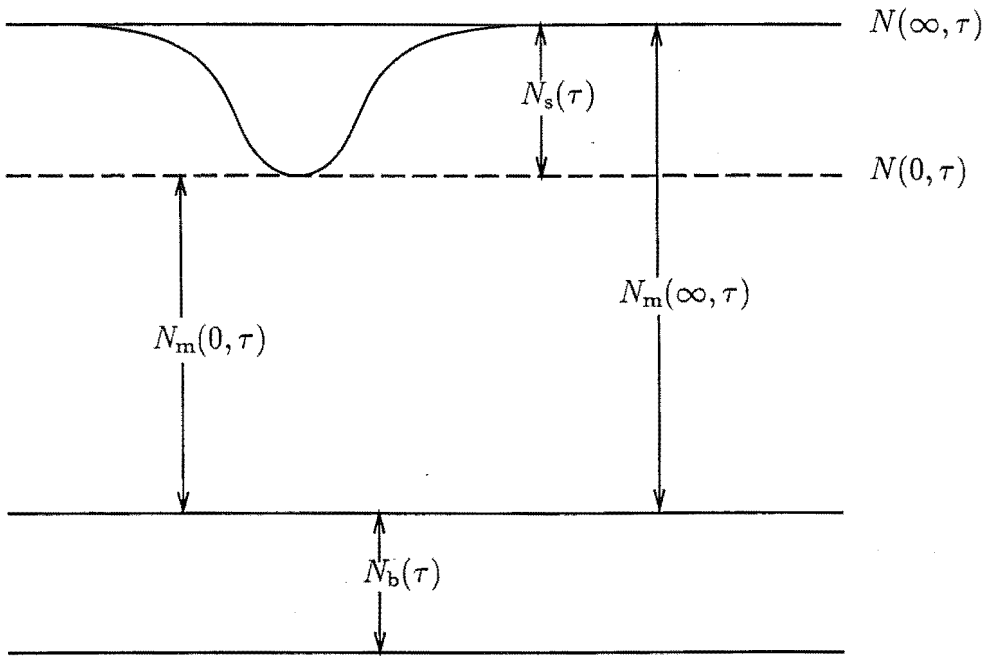

Figure 3.2: A Mössbauer absorption line, taken from the diagram of Long *et al* (1983). $N(\infty,\tau)$ and $N(0,\tau)$ are the counts far from resonance and on resonance respectively. N_{m} are the counts from the Mössbauer transition, and N_{b} are the background counts.

Referring to figure 3.2 and following the notation of Long *et al* (1983), the signal N_{s} is defined as $N_{\mathrm{s}}(\tau) = N(\infty,\tau) - N(0,\tau)$, where $N(\infty,\tau)$ and $N(0,\tau)$ are the total counts far from resonance and at resonance respectively. The fractional dip D of an absorption line is

$$D = N_{\mathrm{s}}(\tau)/N(\infty,\tau)$$

For a thin absorber we have (Long *et al* 1983)

$$N_{\mathrm{s}}(\tau) = N_{\mathrm{m}}(\infty,0) f\tau\mu_{\mathrm{n}} \exp(-\tau\mu_{\mathrm{e}}) \tag{3.72}$$

where $N_{\mathrm{m}}(\infty,0)$ is the number of counts from the Mössbauer transition ($N(\infty,\tau) = N_{\mathrm{m}}(\infty,\tau) + N_{\mathrm{b}}(\tau)$ where $N_{\mathrm{b}}(\tau)$ is the number of background counts),

f is the recoil-free fraction of the absorber, and μ_n is the nuclear mass absorption coefficient for resonant absorption. Since all gamma-rays producing counts in the system undergo electronic absorption,

$$N(\infty,\tau) = N(\infty,0)\exp(-\tau\mu_e)\ , \tag{3.73}$$

so

$$D = (N_m(\infty,0)/N(\infty,0))f\tau\mu_n$$

Letting subscript 1 denote parameters referring to absorber D from crystal B $NH_4Co_{1-x}Fe_xCl_3$, and subscript 2 denote the new absorber, the ratio of the fractional dips is

$$\frac{D_2}{D_1} = \frac{\tau_2\mu_{n_2}}{\tau_1\mu_{n_1}}\ .$$

This ratio is independent of N and N_m because the ratio $N_m(\infty,0)/N(\infty,0)$ is dependent only on the source. Also f is expected to be independent of the $^{57}Fe^{2+}$ concentration for low concentrations of $^{57}Fe^{2+}$. The two absorber thicknesses are $\tau_1 = \tau_2 (\approx 100\ \text{mg.cm}^{-2})$, and so the ratio of the fractional dips is independent of τ. The total nuclear mass absorption coefficient for the absorber (μ_n) is equal to the mass fraction of ^{57}Fe in the absorber multiplied by the nuclear absorption coefficient for ^{57}Fe. Defining w to be the mass fraction of ^{57}Fe in the $NH_4Co_{1-x}Fe_xCl_3$ crystal, the ratio of the fractional dips is

$$\frac{D_2}{D_1} = \frac{F_2w_2}{F_1w_1}\ . \tag{3.74}$$

$D_1 \approx 10\%$, so this ratio should be approximately 1.

The signal to noise ratio is

$$S \equiv N_s(\tau)/\sqrt{(\Delta N(\infty,\tau))^2 + (\Delta N(0,\tau))^2}$$

where ΔN is the statistical uncertainty in N. Since a numerical fitting program was used, the baseline is determined from a large number of points, and the uncertainty in the baseline $\Delta N(\infty,\tau)$ is small compared to $\Delta N(0,\tau)$. Hence $\Delta N(\infty,\tau)$ is ignored. Radioactive decay obeys Poisson statistics, and using the fact that $N_s(\tau)$ is small, $N(0,\tau) \simeq N(\infty,\tau)$, and

$$\Delta N(0,\tau) \simeq \sqrt{N(\infty,\tau)}\ .$$

Using equations (3.72) and (3.73), the signal to noise ratio is

$$S = \frac{N_{\rm m}(\infty,0) f \tau \mu_{\rm n} \exp(-\tau\mu_{\rm e})}{[N(\infty,0)\exp(-\tau\mu_{\rm e}]^{\frac{1}{2}}} .$$

Both $N_{\rm m}(\infty,0)$ and $N(\infty,0)$ are proportional to time t, so

$$S \propto \sqrt{t} f \tau \mu_{\rm n} \exp(-\tau\mu_{\rm e}/2) .$$

For a given S,

$$\frac{t_2}{t_1} = \left(\frac{F_1 w_1}{F_2 w_2}\right)^2 \exp[\tau(\mu_{\rm e_2} - \mu_{\rm e_1})] . \tag{3.75}$$

The choice of the ratio $t_2/t_1 \approx 2$ is reasonable, since an acceptable signal to noise ratio S was obtained after ~ 12 hrs for absorber D $NH_4Co_{1-x}Fe_xCl_3$.

A solution to equations (3.74), and (3.75) with $F \lesssim 0.57$ is $w_2 = 0.155\%$ and $F_2 = 0.529$. $w_2 = 0.155\%$ corresponds to 0.50 atomic percent ^{57}Fe in $NH_4Co_{1-x}Fe_xCl_3$.

Chapter 4

Results and Discussion

4.1 NH_4FeCl_3

4.1.1 Spectra Taken at Temperatures Above 5.5 K

Representative Mössbauer spectra of a powder absorber of NH_4FeCl_3 in the temperature range 5.5 K to 250 K are shown in figure 4.1. The results presented in this section and section 4.1.2 are to be published in Sheen *et al* (1994). The spectra above 10 K consist of a pair of quadrupole split absorption lines of unequal intensity. The difference in intensity is due to preferential orientation of the crystallites in the absorber, as discussed later in this section. Weak absorption lines are evident around the higher energy line of the main quadrupole split pair in the 5.5 K and 6.0 K spectra, presumably due to a precursor of the magnetic ordering shown at 1.3 K in section 4.1.2. These weak extra lines were not of sufficient intensity to allow accurate determination of their parameters, and so were not included in the final fit.

For spectra taken at temperatures above 5.5 K, each main absorption line was fitted with a Lorentzian lineshape with independent parameters position, linewidth, and depth as a fraction of the baseline. The isomer shift (IS) was derived from the line positions by taking the average line position, and the quadrupole splitting (QS) was found from the difference of the two line positions for each spectrum. The linewidth (Γ) is the full width at half maximum of the fitted Lorentzian lineshape, as described in section 3.1, and the depth is expressed as a fraction of the baseline.

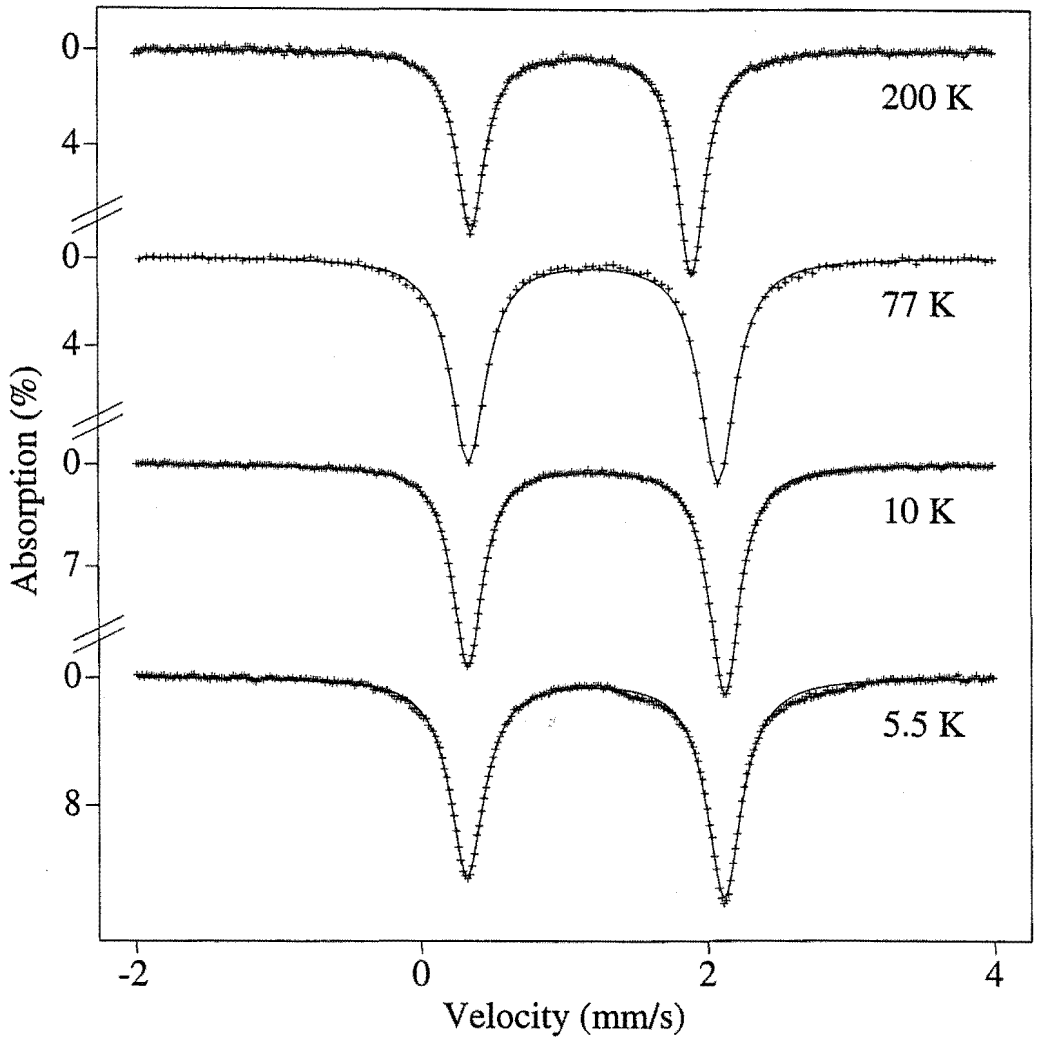

Figure 4.1: Representative Mössbauer spectra of paramagnetic NH_4FeCl_3 in the range 200 K to 5.5 K. The fitted curves have Lorentzian lineshapes.

The uncertainties in QS, IS and linewidth were calculated according to table 2.1. The uncertainty in depth is taken to be the statistical uncertainty of the line depth obtained from the fitting program. The contribution from spectrometer drift to the uncertainties of the parameters of the spectra taken using the Liverpool University Oliver Lodge laboratory spectrometer were assumed to be the same as those obtained for the University of Canterbury Physics Department spectrometer as discussed in section 2.2. The parameters from the fits to the spectra taken above 5.5 K are shown in table 4.1.

The linewidth broadens rapidly at temperatures below 10 K, well above the Neél

Absorber	T (K)	QS (mm s^{-1})	IS (mm s^{-1})	Γ (mm s^{-1})		depth (%)	
				right	left	right	left
E	250	−1.49(1)	1.11(1)	0.239(5)	0.247(6)	4.79(6)	5.70(5)
D	200	−1.55(1)	1.14(1)	0.239(2)	0.244(3)	9.5(3)	7.7(3)
D	150	−1.63(1)	1.17(1)	0.245(3)	0.246(3)	11.5(4)	9.4(4)
E	110	−1.70(2)	1.19(1)	0.250(3)	0.254(3)	11.9(5)	10.1(5)
D	100	−1.72(2)	1.20(1)	0.252(2)	0.252(3)	13.6(4)	11.4(4)
D	80	−1.73(2)	1.21(1)	0.254(3)	0.254(3)	14.6(5)	12.3(5)
L	77	−1.74(2)	1.21(1)	0.295(5)	0.297(5)	10.3(5)	9.4(5)
E	60	−1.75(2)	1.21(1)	0.253(3)	0.256(3)	14.1(5)	12.1(5)
E	40	−1.76(2)	1.22(1)	0.256(3)	0.258(3)	13.8(4)	12.0(4)
E	20	−1.78(2)	1.23(1)	0.259(2)	0.261(3)	15.7(4)	13.7(4)
E	15	−1.78(2)	1.22(1)	0.259(3)	0.260(3)	15.8(3)	13.9(3)
E	10	−1.79(2)	1.22(1)	0.261(2)	0.259(2)	15.8(3)	13.9(3)
E	6.0	−1.81(2)	1.23(1)	0.282(4)	0.285(4)	12.8(4)	14.3(4)
E	5.5	−1.79(2)	1.22(1)	0.294(5)	0.297(5)	12.5(4)	13.8(4)

Table 4.1: Data from Mössbauer spectra of NH_4FeCl_3 above 5.5 K. The absorption lines were fitted with Lorentzian lineshapes. The L denotes a spectrum taken at Liverpool University, and D and E refer to the absorber with composition given in table 2.4. The numbers in brackets indicate the uncertainty in the least significant figure.

temperature of 1.7 K (Visser and Harrison 1992). Broadening of the Mössbauer absorption lines above T_N has not been reported for any other members of the $AFeX_3$ group, where A is one of NH_4, Rb or Cs, and X is Cl or Br. It is tempting to draw a parallel with $CsCo_{1-x}Fe_xCl_3$ and $NH_4Co_{1-x}Fe_xCl_3$. In these compounds, broadening of the Mössbauer lines occurs up to $\sim$ 80 K, approximately 4 times their magnetic ordering temperatures. Indeed, for $RbFeCl_3$, neutron diffraction experiments of Davidson *et al* (1971) indicate that magnetic correlations along the c axis occur up to 20 K (T_N for $RbFeCl_3$ is 2.55 K (Shiba 1982)). NIS experiments may confirm whether or not the increase in linewidth in NH_4FeCl_3 above T_N is due to 1–dimensional correlations.

As discussed in section 3.6 the intensities of the quadrupole split lines are not equal, due to preferential orientation of the crystallites in the absorber. The ratio of the line intensities of the 77 K spectrum was used to calculate the parameter $< \sin^2 \alpha >_{av}$, defined by equation (3.68). This parameter was then used when fitting the spectra of magnetically ordered NH_4FeCl_3.

The right–hand lines of the paramagnetic spectra of figure 4.1 are the most

intense. Hence, using the theory derived on page 53, $V_{zz} < 0$, and the right-hand line of a spectrum of paramagnetic NH_4FeCl_3 is due to the $m_I = \pm\frac{1}{2} \rightarrow \pm\frac{1}{2}$ transition. Thus, since the area of a Lorentzian lineshape is proportional to its width Γ multiplied by its depth, the ratio of line intensities x for the 77 K spectrum is $x = 1.087 \pm 37$, giving by equation (3.69), $< \sin^2 \alpha >_{av} = 0.722 \pm 23$. The sign of V_{zz} is confirmed by fits of the Mössbauer spectrum taken at 1.3 K.

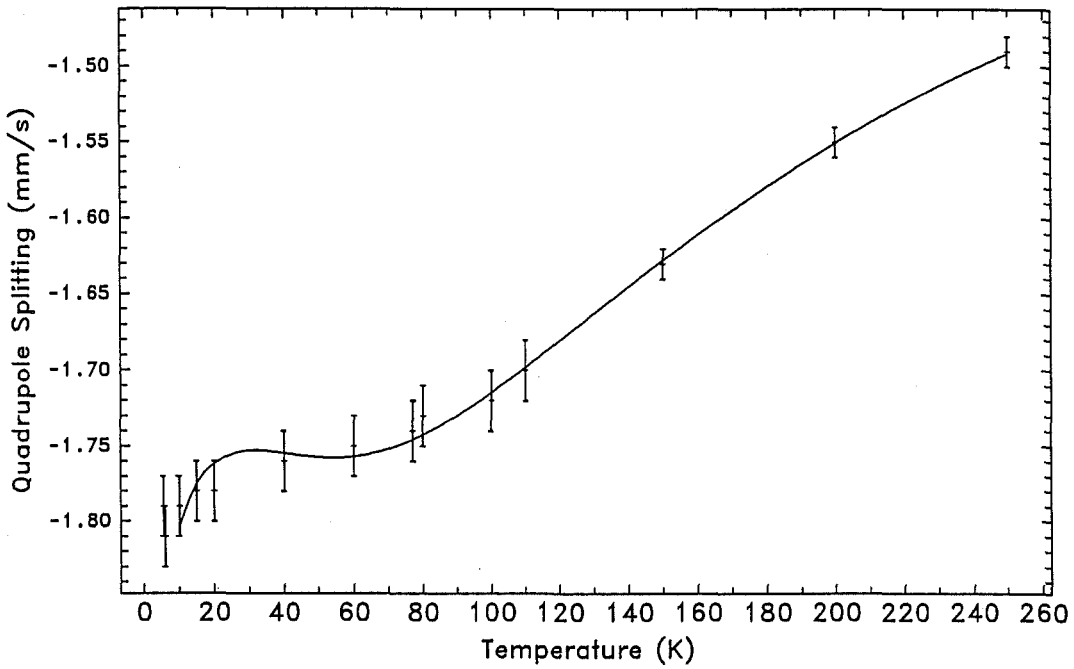

Figure 4.2: The quadrupole splitting for NH_4FeCl_3 at temperatures above 10 K. The solid curve is calculated from the eigenstates of the electronic Hamiltonian according to the expectation value of V_{zz}, and is for the parameter set of table 4.2 with $\left\langle r_Q^{-3} \right\rangle = 4.5$ au. The curve for the parameter set with $\left\langle r_Q^{-3} \right\rangle$=3.0 au is the same.

As can be seen in figure 4.2, QS varies smoothly over the whole temperature range. The structural phase transition which occurs between 10 and 30 K (Harrison 1993) evidently does not change the local environment of the Fe^{2+} ions sufficiently to be observed as a change in QS. In ND_4FeBr_3 structural phase transitions occurring at (270±10) K and (90±10) K are attributed to lowering of the symmetry through cooperative rotations of the ammonium ions and the magnetic chains (Harrison *et al* 1991). The magnetic chain is moved as a whole, and so interactions centred about the chain, for example J_{eff} and V_{zz}, are expected to be relatively unaffected.

$RbFeBr_3$ has a hexagonal perovskite structure and space group $P6_3/mmc$ at room temperature. Chains of trigonally–distorted, face–sharing $FeBr_6^{4-}$ octahedra lie parallel to the crystal c–axis. At 108 K (Harrison and Visser 1989) $RbFeBr_3$ undergoes a structural phase change in which 2/3 of the Fe^{2+}chains move by approximately 0.5 Å out of the basal plane to form a honeycomb lattice, with the remaining 1/3 of the chains in a triangular array. This phase change, which is possibly of the same nature as that observed in NH_4FeCl_3, does not result in a change in QS (Lines and Eibschütz 1975).

The eigenstates of the Hamiltonian for the Fe^{2+} electrons (equation (3.39)) were used to calculate the quadrupole splitting according to equations (1.5) and (3.41) to (3.43). The Hamiltonian parameters B_0^2, B_0^4, λ, and $V_{zz}^{\rm lat}$ were varied to obtain the best fit of the calculated QS to the experimental QS for temperatures above 10 K. The 5.5 K and 6.0 K spectra were omitted from this analysis since they are affected by a precursor of magnetic ordering. The fitted values of QS above 10 K are plotted in figure 4.2. The poor fit at temperatures below 40 K is common to similar fits for $RbFeBr_3$, $CsFeBr_3$, $RbFeCl_3$, and $CsFeCl_3$ (McCann *et al* 1992). As discussed in that paper, including a correlated effective field term (Lines 1974) into the electronic Hamiltonian (3.5) does not significantly improve the fit to the data for these compounds. Problems with the correlated effective field were discussed by Suzuki (1978) and a modification, the dynamic correlated effective field, was developed. This theory was developed for an Heisenberg Hamiltonian. Although an effective $S' = 1$ spin Hamiltonian which incorporates anisotropic correlation effects has been used (Suzuki 1983), it is unclear how to use these results to calculate QS if the exchange interaction is anisotropic.

The parameters obtained by fitting QS are shown in table 4.2. The calculated QS was insensitive to the value of the cubic crystal field parameter $B_{\rm C}^4$, so in these fits $B_{\rm C}^4$ was fixed to 10 150 cm^{-1} obtained from optical absorption spectra of $RbFeCl_3$ and $CsFeCl_3$ taken by Putnik *et al* (1976). The value of λ is reduced from its free ion value of 103 cm^{-1} (Trees 1951) by covalency effects. Appropriate limits on λ are $50 \lesssim \lambda \lesssim 90$ cm^{-1} (Ingalls 1977). $\left\langle r_{\rm Q}^{-3} \right\rangle$ is also reduced by covalency from its free ion value of 4.93 au (Freeman and Watson 1963). The values of the parameters $\left\langle r_{\rm Q}^{-3} \right\rangle$, B_0^2, and B_0^4 were correlated, with a wide range of parameters yielding the same goodness of fit χ^2. In fitting QS, it was necessary to fix $\left\langle r_{\rm Q}^{-3} \right\rangle$

$\langle r_Q^{-3} \rangle$ (au)	B_0^2 (cm^{-1})	B_0^4 (cm^{-1})	λ (cm^{-1})	$\frac{1}{2}\lvert e\rvert QV_{zz}^{lat}$ (mm s^{-1})
3.0	-150(50)	50(50)	-60(5)	-1.16(2)
4.5	30(50)	70(50)	-60(5)	-1.16(2)

Table 4.2: Parameters obtained from fitting the quadrupole splitting shown in figure 4.2 using Hamiltonian (3.39) and QS calculated using equations (1.5) and (3.41). B_C^4 was fixed to 10 150 cm^{-1} and $\langle r_Q^{-3} \rangle$ was fixed to the values shown. The numbers in brackets indicate the uncertainty in the least significant figure(s).

in order that it did not become larger than its free ion value. Values of 3.0 and 4.5 au were chosen to cover the range of reasonable values for $\langle r_Q^{-3} \rangle$. There was a strong interdependence of the two axial parameters B_0^2 and B_0^4, resulting in large uncertainties in their determination. Fits with small values of these parameters were chosen as being more representative of a trigonal (axial) distortion of the basic octahedral symmetry.

4.1.2 Spectra Taken at Temperatures Below 5.5 K

Fits to the 1.3 K spectrum using the computer program FUSTOP (see section 3.1 on page 35.) determined the angle between the magnetic hyperfine field and the z principal axis of the EFG tensor to be $\theta = (90 \pm 10)°$. In all subsequent fits to magnetically ordered NH_4FeCl_3 spectra, θ was fixed to 90°. Also, $< \sin^2 \alpha >_{av}$ was fixed to 0.722, the value determined from a spectrum of the same absorber at 77 K.

It is noted that the high energy (right hand) line at high temperature (above $\sim$ 5 K) is split into three absorption lines at 1.3 K, whilst the low energy line is split into two lines at 1.3 K. These splittings confirm the conclusion of the previous section that $V_{zz} < 0$.

It can be seen from figure 4.3 that two subspectra are necessary to fit the 1.3 K spectrum; one with magnetic hyperfine splitting, and the other nonmagnetic. The parameters IS, QS, and Γ were forced to be the same for both subspectra in the static field fit of figure 4.3. This fit is improved if slow relaxation, as outlined in section 3.2, is permitted between the two subspectra.

Figure 4.4 shows Mössbauer spectra of NH_4FeCl_3 at 4.2 K and 1.3 K fitted using

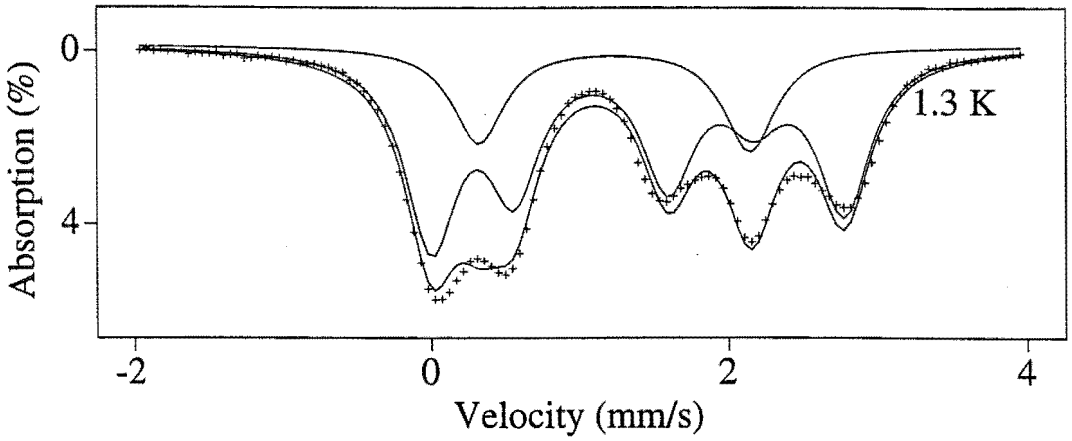

Figure 4.3: A static fit to the Mössbauer spectrum of NH_4FeCl_3 at 1.3 K. The fitted curve is the sum of two subspectra; a magnetic subspectrum, and a quadrupole split nonmagnetic pair of lines.

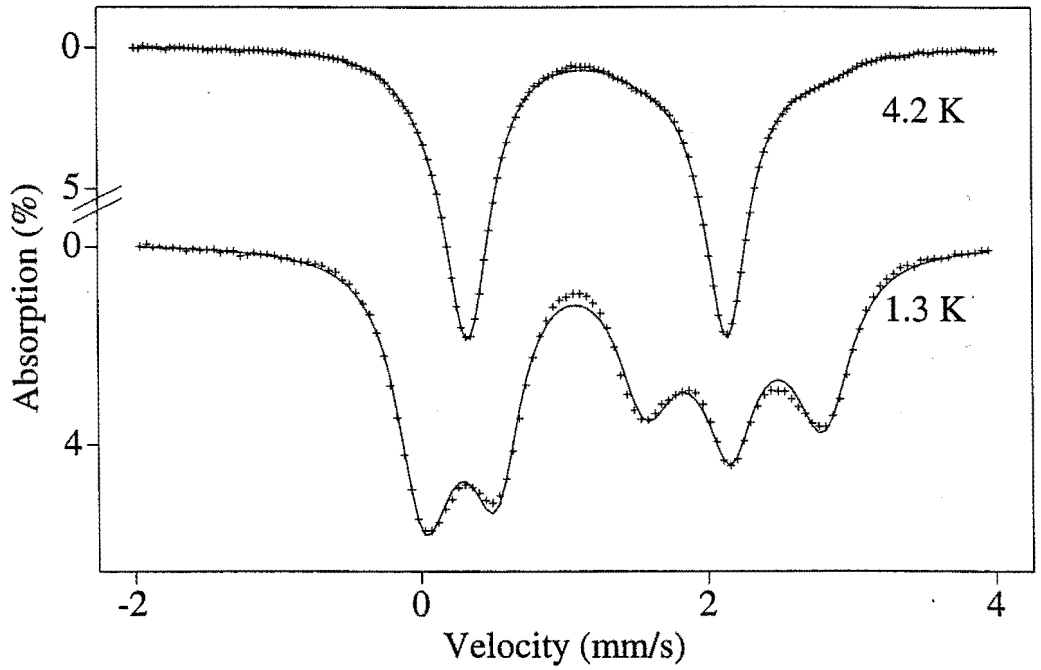

Figure 4.4: Mössbauer spectra of NH_4FeCl_3 taken at 4.2 K and 1.3 K. The spectra were fitted with relaxation lineshapes using program FUSTOP as described in the text.

the program FUSTOP with relaxation between magnetic hyperfine fields of 0 and $B_{\rm hf}$ at an angle of 90° to the principal axis of the EFG tensor.

The parameter values obtained for both relaxing and static field fits are summarised in table 4.3. B is the magnitude of the magnetic hyperfine field, P_m is

T (K)	χ^2	QS (mm s^{-1})	IS (mm s^{-1})	Γ (mm s^{-1})	B (T)	P_m (%)	R (MHz)
4.2	1.4	−1.807(5)	1.229(1)	0.292(5)	5.32(6)	21(1)	0.90(11)
	4.7	−1.813(5)	1.228(1)	0.369(20)	4.2(3)	12(3)	0^f
1.3	3.7	−1.804(3)	1.229(2)	0.34(2)	5.2(2)	72(1)	1.1(2)
	12	−1.826(3)	1.234(2)	0.42(5)	4.7(3)	77(2)	0^f

Table 4.3: Parameters obtained by fitting the 4.2 and 1.3 K spectra using the program FUSTOP. The superscript f denotes parameters whose values were fixed, and the numbers in brackets indicate the uncertainty in the least significant figure(s).

the proportion of the spectrum which is magnetic, and R is the relaxation rate. It should be noted that the goodness of fit parameter χ^2 can only be compared between different fits of the same spectrum, since the statistics vary between spectra. The relative area of the magnetic subspectrum increases from 21 % for the 4.2 K spectrum to 72 % for the 1.3 K spectrum.

Comparing the values of QS, IS, and Γ of table 4.3 for the fits using FUSTOP to the values above 5.5 K, it can be seen that QS and IS at 1.3 K and 4.2 K follow the trend of the data above 5.5 K. The linewidth used in fitting spectra showing relaxation should be the same as that for a spectrum without relaxation effects at higher temperatures. The same absorber as was used at 1.3 K and 4.2 K had a linewidth of (0.296±0.005) mm s^{-1} at 77 K. The increase in Γ shown in table 4.3 for the fits to the 1.3 K spectrum indicates that neither of the models used describe the spectra adequately. The broadened absorption lines are suggestive of a distribution of hyperfine magnetic fields. However, the cause and form of the distribution of hyperfine magnetic fields is unknown.

The persistence of the non–magnetic subspectrum below the ordering temperature $T_{\rm N} = (1.7 \pm 0.2)$ K (Visser and Harrison 1992) is unexplained at present. The series $AFeCl_3$ where A is Rb, Cs, or NH_4 have ferromagnetic exchange interactions between the Fe^{2+} spins along the c axis (Achiwa 1969, Witteveen and van Veen

1973, and Montano *et al* 1974). $RbFeCl_3$ is expected to have similar exchange interactions to NH_4FeCl_3, because of the similar atomic radii of Rb^+ and NH_4^+ (1.47 Å for Rb^+, and 1.43 Å for NH_4^+, Handbook of Chemistry and Physics (1990)), and has a weak antiferromagnetic interchain exchange interaction (Eibschütz *et al* 1975). $RbFeCl_3$ has three ordering temperatures (Wada *et al* 1982, Shiba 1982) of 1.95, 2.3 and 2.55 K, with the magnetic phases changing from a commensurate structure below 1.95 K, through two incommensurate phases, to the paramagnetic phase above 2.55 K. The 1.3 K Mössbauer spectrum of $RbFeCl_3$ (Baines *et al* 1983) is completely magnetic. $RbFeCl_3$ is in the 120° triangular phase at this temperature, and thus each Fe^{2+} site is expected to be subject to magnetic exchange.

A possible explanation of the presence of the non–magnetic subspectrum and linewidth broadening in the 1.3 K Mössbauer spectrum of NH_4FeCl_3 is that there are magnetically inequivalent sites as there would be in an incommensurate phase. This explanation may be confirmed by NIS experiments. Further Mössbauer spectra of NH_4FeCl_3 taken at low temperatures, as well as some spectra in the incommensurate phase of $RbFeCl_3$, may also be interesting.

Another possible cause of the persistence of the non–magnetic spectrum below T_N may be partial disorder (Matsubara 1982) as suggested for $RbFeBr_3$. Using specific heat measurements Adachi *et al* (1983) found two ordering temperatures for this salt, one at (5.16±0.02) K and one at (2.00±0.04) K. They predicted that the phase between the ordering temperatures was partially disordered, in which 1/3 of the chains of Fe^{2+} ions remain uncorrelated with the others. Eibschütz *et al* (1973) used neutron diffraction to determine the magnetic structure, and found that at 1.7 K there were two models which gave good fits to the intensity data. The first was a triangular arrangement in which the Fe^{2+} moments all equalled 2.2 μ_B, and the second was a collinear antiferromagnetic structure in which 1/3 of the chains of Fe^{2+} ions had zero moment, and 2/3 had a moment of 2.7 μ_B. The Mössbauer spectrum of $RbFeBr_3$ taken at 1.54 K by Eibschütz *et al* (1973) showed no magnetic splitting or appreciable broadening. They tentatively attributed this result to cancellation of the different components of the magnetic hyperfine field (see equation (3.44)). Using NIS at 4.5 K Harrison and Visser (1992) were unable to confirm the existence of an ordered phase in $RbFeBr_3$ other than the regular triangular structure. Nevertheless, their results did not rule out the existence of a

partially disordered phase, since it was expected that the difference in the exchange interactions between the magnetically ordered sites and between partially disordered sites would not cause sufficient splitting of the energy of the magnetic excitations to be resolved with their apparatus.

If partial disorder is occurring in NH_4FeCl_3 then the zero magnetic hyperfine field could be associated with the disordered chains. This would account for 33 % of the spectrum so that 67 % of the spectrum would show magnetic hyperfine splitting. However at 1.3 K the "magnetic" subspectrum is (72 ± 1) % of the total area (see table 4.3) so the experimental results are inconsistent with the model of partial disorder. Neutron diffraction may be useful in determining the magnetic phases of NH_4FeCl_3.

The persistence of the magnetically split subspectrum up to 6.0 K (see figures 4.1 and 4.4), and the broadening of the 5.5 and 6.0 K spectra indicate the existence of magnetic correlations in NH_4FeCl_3 above the ordering temperature of 1.7 K, as observed in $RbFeCl_3$ (Davidson *et al* 1971).

To summarise, the linewidth broadening below 10 K is evidence for the existence of magnetic correlations at these temperatures. The 4.2 K and 1.3 K spectra show that a distribution of magnetic hyperfine fields are present, the major components are 21 % of the Mössbauer spectrum with $B = (5.32 \pm 0.06)$ T at 4.2 K and 72 % of the Mössbauer spectrum with $B = (5.2 \pm 0.2)$ T at 1.3 K. The cause of the magnetic subspectrum above T_N=1.7 K and the persistence of the non–magnetic subspectrum at 1.3 K are unexplained although possible reasons for the persistence have been discussed.

4.2 $NH_4Co_{1-x}Fe_xCl_3$

4.2.1 Mössbauer Spectra of Paramagnetic $NH_4Co_{1-x}Fe_xCl_3$.

Figure 4.5 displays some representative spectra of $NH_4Co_{1-x}Fe_xCl_3$ in the temperature range 27.5 K to 250 K. The spectra show a pair of quadrupole split absorption lines, as is characteristic of spectra of Fe^{2+} ions in paramagnetic samples in sites with a distortion from octahedral symmetry. No extra lines, due to hydration or

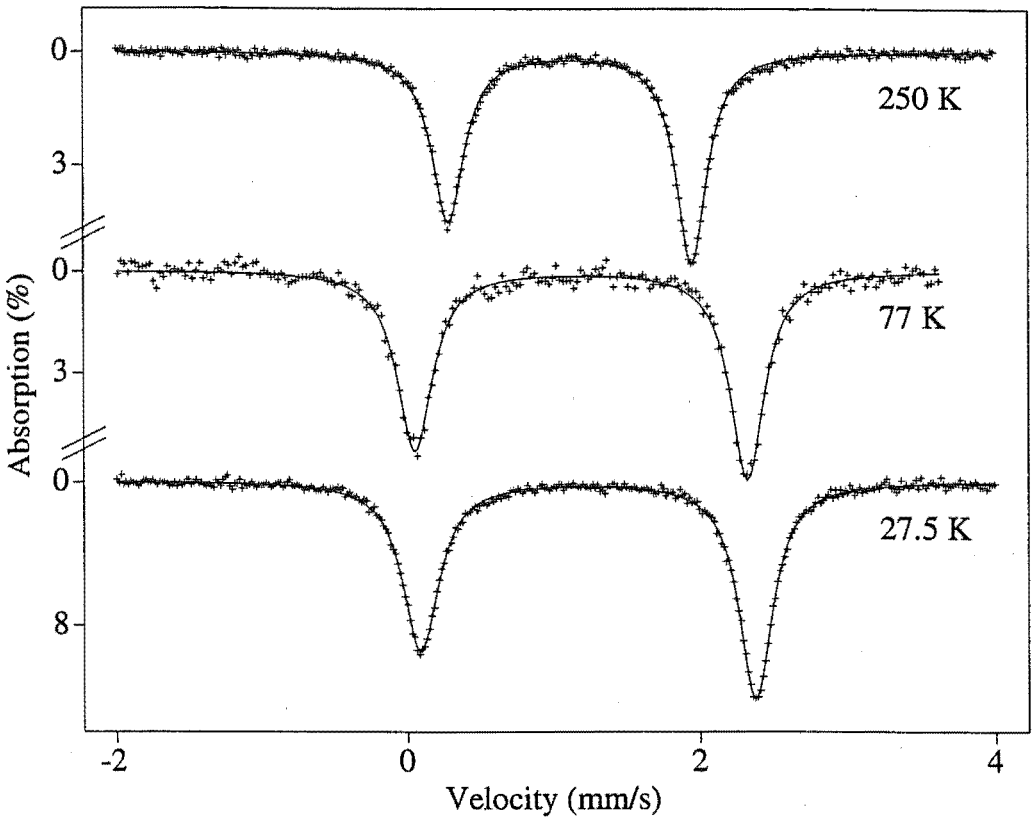

Figure 4.5: Representative Mössbauer spectra of paramagnetic $NH_4Co_{1-x}Fe_xCl_3$ in the range 250 K to 27.5 K. The 77 K spectrum was taken at Liverpool University. The fitted curves have Lorentzian lineshapes.

T	QS	IS	Γ (mm s^{-1})		depth (%)	
(K)	(mm s^{-1})	(mm s^{-1})	left	right	left	right
250	−1.665(15)	1.116(10)	0.269(6)	0.245(5)	4.52(6)	5.67(6)
200	−1.831(16)	1.143(10)	0.250(3)	0.249(3)	5.6(2)	6.9(2)
150	−2.025(18)	1.176(11)	0.256(4)	0.258(3)	6.6(5)	8.0(5)
110	−2.182(19)	1.191(11)	0.266(3)	0.263(3)	7.6(4)	9.3(4)
80	−2.229(20)	1.199(11)	0.264(3)	0.268(3)	8.8(4)	10.5(4)
77	−2.271(20)	1.187(11)	0.293(3)	0.281(3)	5.3(4)	6.2(4)
60	−2.279(20)	1.220(11)	0.266(3)	0.266(3)	9.4(4)	11.4(4)
40	−2.280(20)	1.226(11)	0.272(3)	0.274(3)	10.1(5)	11.9(5)
30	−2.287(20)	1.232(11)	0.287(3)	0.276(3)	9.8(4)	12.1(4)
27.5	−2.288(20)	1.233(11)	0.301(4)	0.277(3)	9.5(6)	12.2(6)

Table 4.4: Parameters obtained from Mössbauer spectra of absorber B $NH_4Co_{1-x}Fe_xCl_3$ above 27.5 K. The 77 K spectrum was taken at Liverpool University. The absorption lines were fitted with Lorentzian lineshapes. The numbers in brackets indicate the uncertainty in the least significant figure(s).

impurities, are apparent. Each absorption line was fitted with a Lorentzian lineshape, and the fitted parameters QS, IS, Γ, and depth are shown in table 4.4. Below 40 K the linewidth shows a gradual increase as the temperature decreases, consistent with magnetic correlations along the c axis above the magnetic ordering temperature (Ajiro *et al* 1989). The large width of the left line of the 250 K spectrum is probably due to partial hydration of the sample which occurred while the 250 K spectrum was being taken. A 200 K spectrum taken immediately after the 250 K spectrum clearly showed extra lines, presumably due to hydration.

QS values above 30 K were fitted using the same general procedure as for NH_4FeCl_3. With the cubic crystal field parameter fixed to 10150 cm^{-1}, as for NH_4FeCl_3, it was found that a very good fit could be obtained for any value of $\left\langle r_Q^{-3} \right\rangle$ in the range 3.5 to 4.5 au, if $|B_0^2|$, $|B_0^4|$, and $|\lambda|$ were allowed to become very large. For reasonable values of λ (less than 90 % of its free ion value of -104 cm^{-1}), and B_0^4 fixed to values less than 3000 cm^{-1}, the energy splittings between the singlet ground state and the first excited doublet were found to be in the range 6.5 to 17 cm^{-1} at 27 K (T_{N_1}). A value of $B_0^4 = 1000$ cm^{-1} was chosen, which gave the greatest stability of χ^2 to variation of $\left\langle r_Q^{-3} \right\rangle$, and gave a singlet–doublet splitting at 27 K of $\sim$ 11.3 cm^{-1} for values of $\left\langle r_Q^{-3} \right\rangle$ of both 3.5 and 4.5 au. The fits obtained when $\left\langle r_Q^{-3} \right\rangle$ was fixed to 3.5 and 4.5 au are shown in figure 4.6, while the parameters obtained are shown in table 4.5. Values of QS below 30 K are also shown in figure 4.6 and these are discussed in the next section.

The values for λ and $\frac{1}{2}|e|QV_{zz}^{lat}$ can be compared to those obtained for Fe^{2+} in the similar environment in $CsCo_{1-x}Fe_xCl_3$ (Ward *et al* 1987, and section 4.3), and to those found in NH_4FeCl_3. General agreement is found, with λ being the same within uncertainties for all three salts, and $\frac{1}{2}|e|QV_{zz}^{lat}$ lying between the values (–0.41±0.08) and (–1.16±0.02) mm s^{-1} for $CsCo_{1-x}Fe_xCl_3$ and NH_4FeCl_3 respectively.

As can be seen from the unequal line intensities in figure 4.5, there is preferential orientation of the crystallites in absorber B of $NH_4Co_{1-x}Fe_xCl_3$. The ratio of the right to left hand line intensity is 1.23±0.09 for the 200 K spectrum, giving a value of $< \sin^2 \alpha >_{av}$=0.80±0.05, and consistent with $V_{zz} < 0$. The assignment of $V_{zz} < 0$ is confirmed by the low temperature spectra (in figure 4.7) which can only be fitted if $V_{zz} < 0$. The ratio of the right to left hand line intensities for the 200 K spectrum of absorber E of $NH_4Co_{1-x}Fe_xCl_3$ is 1.21±0.09, yielding $< \sin^2 \alpha >_{av}$=0.79±0.05.

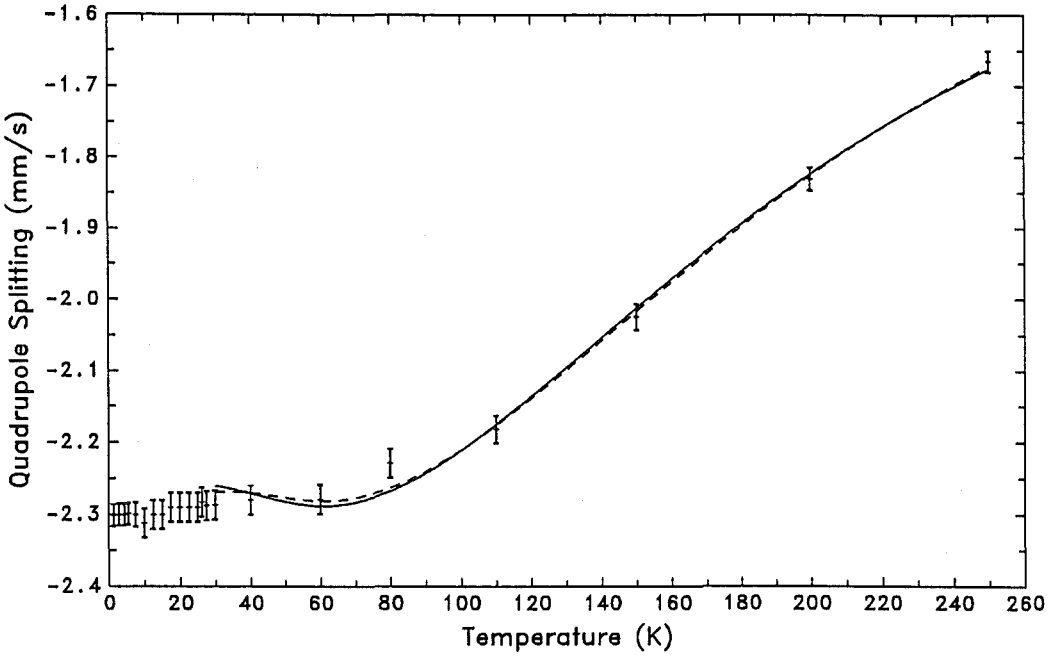

Figure 4.6: The quadrupole splitting for absorber B of $NH_4Co_{1-x}Fe_xCl_3$ fitted for temperatures above 30 K. The fitted curves were calculated from the eigenstates of the electronic Hamiltonian according to the expectation value of V_{zz} for the different parameter sets in table 4.5. The dashed (solid) curve corresponds to the parameter set of table 4.5 with $\left\langle r_Q^{-3} \right\rangle$ fixed to 4.5 (3.5) au. The QS at temperatures below 27.5 K is from spectra of absorber E of $NH_4Co_{1-x}Fe_xCl_3$ fitted using the combined relaxation model (program SOEL) as described in section 4.2.2.

χ^2	$\left\langle r_Q^{-3} \right\rangle$ (au)	B_0^2 (cm^{-1})	B_0^4 (cm^{-1})	λ (cm^{-1})	$\frac{1}{2}\lvert e\rvert QV_{zz}^{lat}$ (mm s^{-1})
1.45	3.5^f	990(20)	1000^f	-64(3)	-0.75(8)
0.92	4.5^f	950(20)	1000^f	-70(3)	-0.65(8)

Table 4.5: Parameters obtained from fitting the quadrupole splitting data shown in figure 4.6 using Hamiltonian (3.39) and QS calculated using equation (3.41). B_C^4 was fixed to 10 150 cm^{-1}, and the superscript f denotes other parameters which were fixed during the fit. The numbers in brackets indicate the uncertainty in the least significant figure(s).

These values of $< \sin^2 \alpha >_{av}$ were used in section 4.2.2 when fitting the magnetically split relaxation spectra.

4.2.2 Mössbauer Spectra of Magnetically Ordered $NH_4Co_{1-x}Fe_xCl_3$.

As can be seen in figures 4.7 and 4.8, the spectra below T_{N_1} exhibit magnetic splitting, with unequally broadened absorption lines indicating relaxation. In this section the orientation and magnitude of the magnetic hyperfine field and expected energy splittings of the electronic states of Fe^{2+} in $NH_4Co_{1-x}Fe_xCl_3$ are established. Once these preliminary results are analysed, fits to the Mössbauer spectra of $NH_4Co_{1-x}Fe_xCl_3$ using the 2–level, 3–level and combined relaxation models are reported and the parameters obtained from the different models are compared.

Fits of the 1.3 K and 2.8 K spectra using FUSTOP with relaxation between magnetic hyperfine fields of B and 0 T were performed to determine the angle θ between the magnetic hyperfine field and the z principal axis of the EFG tensor. The goodness of fit and parameter values obtained were identical to those obtained from fits with θ fixed to zero. The parameters were the same as in table 4.6, with $\theta = (0.8 \pm 1.3)°$. In all subsequent fits θ was assumed to be zero in $NH_4Co_{1-x}Fe_xCl_3$.

The 1.3 K and 2.8 K spectra could be approximated reasonably by a static fit (no relaxation) using the computer program MOST (the same as FUSTOP except that θ=0 for MOST) with two subspectra, one split by a magnetic hyperfine field, and the other with zero magnetic hyperfine field, as shown in figure 4.9. From these fits it can be seen that at these temperatures there are two electronic states significantly occupied, one state producing $B_{hf} = B$ lying below a state with $B_{hf} = 0$ T. The value of B is determined to be 22.3 T. The parameters of the static and relaxation fits at 1.3 K and 2.8 K are shown in table 4.6, where E_2 is defined as the energy of the $B_{hf} = 0$ state (state (2)) minus the energy of the $B_{hf} = B$ state (state (1)). E_2 is the energy splitting of the two states required to give the correct occupation probabilities according to Boltzmann statistics, as given by equation (3.25).

The broadened spectra between 4.2 K and 10 K cannot be fitted with static hyperfine fields. When these spectra are fitted using a 2 or 3–level relaxation model as described in sections 3.2 and 3.3, the lines which correspond to a $B_{hf} = 0$ T

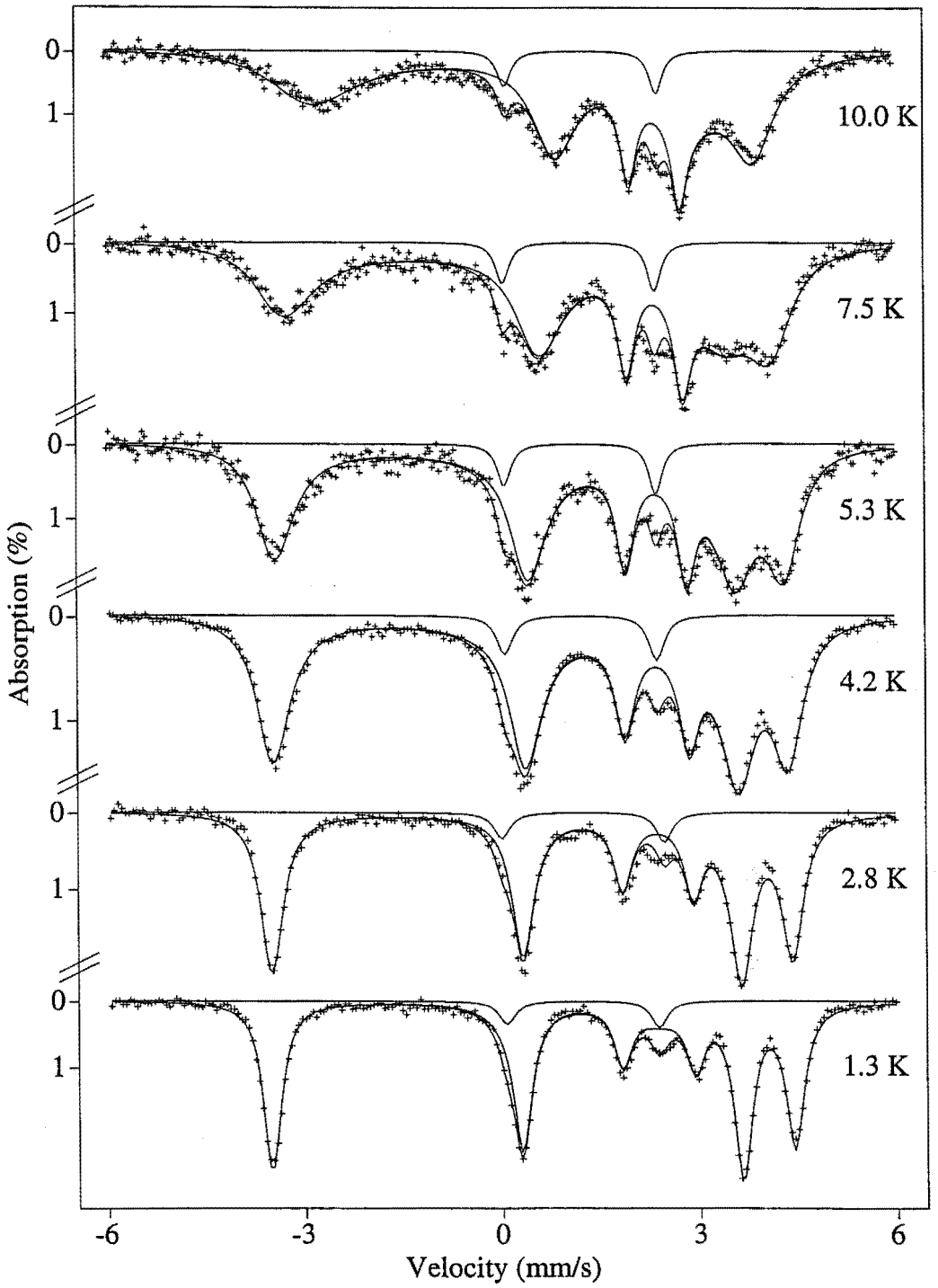

Figure 4.7: Mössbauer spectra of absorber E of $NH_4Co_{1-x}Fe_xCl_3$ taken at temperatures below 10 K. The weak quadrupole–split subspectrum has a relative area of 5.5 % as justified in the text. The main subspectrum is fitted using the computer program THREL (or equivalently SOEL), with electronic relaxation between the 3 lowest Fe^{2+} states as described in section 3.3.

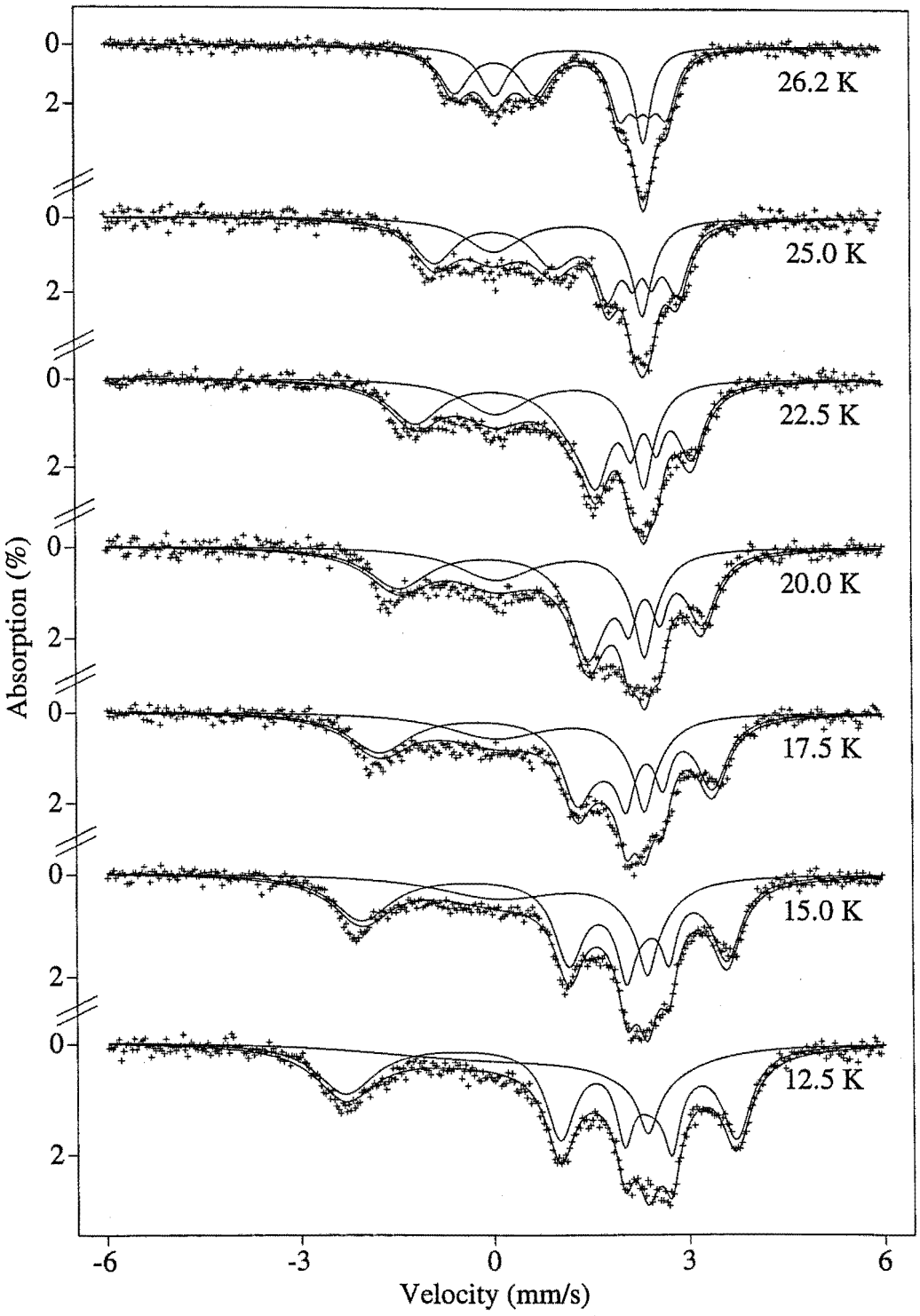

Figure 4.8: Mössbauer spectra of absorber E of $NH_4Co_{1-x}Fe_xCl_3$ taken at temperatures above 12.5 K. The fitted curves were obtained using the combined relaxation model with the computer program SOEL. The relative area of the soliton subspectrum was fixed to 1/3, as described in section 3.4. The remainder of the spectrum, comprising 2/3 of the relative area, has 3–level electronic relaxation only.

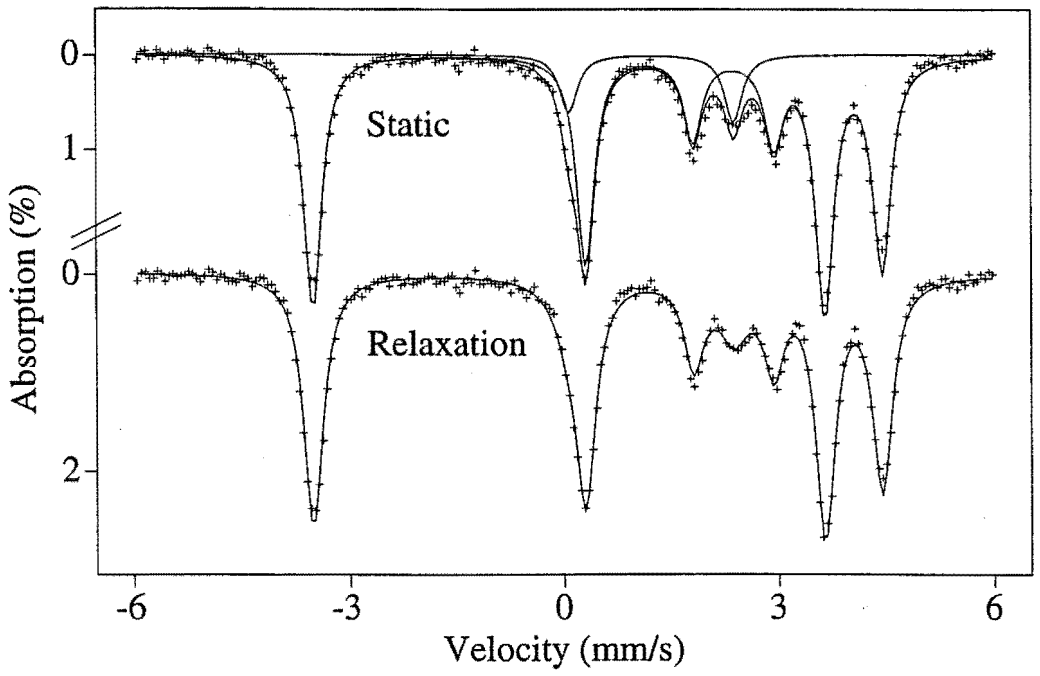

Figure 4.9: Static and relaxation fits to the 1.3 K spectrum of E $NH_4Co_{1-x}Fe_xCl_3$ made using the program MOST. The static fit was obtained by adding two static subspectra, one with a B_{hf}, and the other a quadrupole-split pair of absorption lines. The total spectrum and each subspectrum are shown separately.

T (K)	χ^2	QS (mm s^{-1})	IS (mm s^{-1})	B (T)	E_2 (cm^{-1})	*Rate* (MHz)
1.3	1.76	−2.305(20)	1.225(5)	22.30(3)	1.9(1)	0^f
1.3	1.14	−2.303(20)	1.223(5)	22.31(3)	1.8(1)	0.012(8)
2.8	4.47	−2.305(20)	1.226(5)	22.25(3)	4.5(1)	0^f
2.8	1.17	−2.300(20)	1.220(5)	22.27(3)	3.7(1)	0.040(8)

Table 4.6: Parameters obtained by fitting the 1.3 K and 2.8 K spectra using the computer program MOST. The superscript f denotes parameters whose values were fixed. In these fits the linewidth Γ was fixed to 0.3 mm s^{-1}. The numbers in brackets indicate the uncertainty in the least significant figure(s).

spectrum cannot be fitted. Accordingly, an "extra subspectrum" with $B_{\rm hf} = 0$ T is added in to relaxation fits of spectra in this temperature range. The fits of the 1.3 and 2.8 K spectra are also improved when this procedure is adopted. The relative area of the extra subspectrum is fixed at 5.5 % for all fits between 1.3 and 10 K, as shown in figure 4.7. The constancy of the relative area is consistent with the extra subspectrum originating from a different crystallographic site, since if alternatively it was due to an unusually large population of $B_{\rm hf} = 0$ states (not sites), then the relative area of the extra subspectrum would be expected to change as the temperature varied. Also, if the extra subspectrum was due to an unusually large population of the $B_{\rm hf} = 0$ states, relaxation would occur between the extra $B_{\rm hf} = 0$ T states and the $B_{\rm hf} = B$ states, so the spectra should be fitted well by the relaxation program. This is not the case.

Contrary to the above evidence, the absence of an extra subspectrum in the spectra above T_{N_2} as can be seen in figure 4.8, and the fact that the extra non–magnetic subspectrum has the same QS and IS as the main relaxation spectrum, indicates that the two subspectra originate from similar crystallographic sites.

Below T_{N_2} the relative area of the extra subspectrum in absorber B of $NH_4Co_{0.9916}Fe_{0.0084}Cl_3$ is 10.9 % whereas it is 5.5 % for absorber E of $NH_4Co_{0.99405}Fe_{0.00595}Cl_3$. This difference may indicate that the extra subspectrum is due to $^{57}Fe^{2+}$ ions with Fe^{2+} neighbours (instead of Co^{2+}). However, in $CsCo_{0.97}Fe_{0.03}Cl_3$, Mekata (1990) reports an extra subspectrum at all temperatures, with a different QS from the main spectrum. They attribute the extra lines to Fe^{2+} neighbours, since $CsCo_{0.99}Fe_{0.01}Cl_3$ could be fitted with only one site (Ward *et al* 1987). Also, NH_4FeCl_3 has a distinctly different QS from $NH_4Co_{1-x}Fe_xCl_3$ (see sections 4.1.1 and 4.2.1), so it is expected that an extra subspectrum caused by Fe^{2+} neighbours in $NH_4Co_{1-x}Fe_xCl_3$ would have a different QS from the main spectrum.

The precise origin of these extra lines could not be proved. The following analysis is performed on Mössbauer spectra of absorber E of $NH_4Co_{0.99405}Fe_{0.00595}Cl_3$, since the relative area of the extra subspectrum is least for this absorber.

The energy splitting between the ground singlet and low–lying electronic doublet of the Fe^{2+} ion in $NH_4Co_{1-x}Fe_xCl_3$ was fixed by the electronic Hamiltonian parameters of table 4.5 determined from the temperature variation of QS. The effective Fe–Co exchange parameter $J_{\rm eff}$ of equation (3.47) controls the splitting of the

low–lying doublet of Fe^{2+} in $NH_4Co_{1-x}Fe_xCl_3$. $J_{\rm eff}$ was chosen so that at 2.8 K the predicted energy splitting between the lowest two electronic states was $E_2 \simeq 4$ cm^{-1}. The energy splitting parameter $E_2 = (2.34 \pm 0.02)$ cm^{-1} found from the 1.3 K spectrum was not used, as it was found to be anomalously small (see page 84).

The magnetic subspectrum was used to determine the magnetic hyperfine field B produced by the lowest electronic state of Fe^{2+}. The Fermi contact effective field B_c was determined from B using equation (3.44) and the electronic states found from diagonalizing Hamiltonian (3.45). The values of $J_{\rm eff}$ and B_c determined by the method above are displayed in table 4.7.

$\langle r_Q^{-3} \rangle$ (au)	$J_{\rm eff}$ (cm^{-1})	E_2 (cm^{-1})	B_c (T)	B (T)
4.5	–25	4.2	–55	22.3
3.5	–26	4.2	–53	22.6

Table 4.7: The values of $J_{\rm eff}$ were chosen to give an energy splitting of $\simeq$4 cm^{-1} at 2.8 K (as found from the fits in tables 4.10 and 4.11) with the other Hamiltonian parameters given in table 4.5. The values of B_c were chosen using the same procedure, to give $B \simeq 22.3$ T, the value found from preliminary fits of the 2.8 K spectrum in table 4.6. B in the table is that calculated according to equation (3.44) at 2.8 K using the value of B_c shown, $\langle r^{-3} \rangle$=4.0 au, and the eigenstates of the Hamiltonian (3.39).

Using the wavefunctions obtained by diagonalizing the electronic Hamiltonian with parameters given in tables 4.5 and 4.7, the $B_{\rm hf}$ of each state was calculated using equation (3.44). In these calculations $\langle r^{-3} \rangle$ was taken to be 4.0 au, mid–way between the reasonable limits for $\langle r_Q^{-3} \rangle$ of 3.5 and 4.5 au, and less than the free ion value of $\langle r^{-3} \rangle$. The results of the calculations are given in table 4.8. The component of $B_{\rm hf}$ perpendicular to the z principal axis of the EFG tensor is negligibly small for the three lowest states ($\lesssim 1 \times 10^{-10}$ T). This is consistent with the result that θ=0 found from fitting the 1.3 K and 2.8 K spectra using FUSTOP. It is noted that the temperature variation of $B_{\rm hf}$ is small. In subsequent fits to magnetic spectra, $B_{\rm hf}$ for state (1) was fixed to its low temperature value of 22.3 T, while that for state (2) was fixed to zero. In fits involving state (3), $B_{\rm hf}$ for state (3) was fixed to the negative of that for state (1).

For the three lowest states of the Fe^{2+} ion the energy splittings predicted by diagonalizing the electronic Hamiltonian with the parameter sets given in tables 4.5

$\langle r_Q^{-3} \rangle$ (au)	T (K)	$B_{hf}(1)$ (T)	$B_{hf}(2)$ (T)	$B_{hf}(3)$ (T)
4.5	1.3	22.3	0.9	−25.4
	20.0	22.6	0.7	−25.1
	26.2	23.3	0.3	−24.5
3.5	1.3	22.6	0.9	−25.1
	20.0	22.9	0.7	−24.8
	26.2	23.6	0.3	−24.2

Table 4.8: Theoretical values of the B_{hf} for the three lowest-energy states, calculated for the two parameter sets of tables 4.5 and 4.7 using equation (3.44). The calculations were made assuming that T_{N_1}=27 K. The states are labelled according to their energy at 1.3 K, with state (1) having the lowest energy at 1.3 K.

T (K)	E' (cm^{-1})	E_2 (cm^{-1})	E_3 (cm^{-1})
1.3	−15.9	4.2	31.0
2.8	−15.9	4.2	31.0
4.2	−15.9	4.2	31.0
5.3	−15.8	4.2	31.0
7.5	−15.8	4.2	30.9
10.0	−15.7	4.0	30.7
12.5	−15.4	3.7	30.0
15.0	−14.7	3.1	28.9
17.5	−13.8	2.2	27.0
20.0	−12.3	0.8	24.3
22.5	−10.0	−1.2	20.3
25.0	−7.2	−4.2	14.3
26.2	−4.7	−6.6	9.4
27.0	0.0	−11.3	0.0

Table 4.9: The energies of the three lowest electronic states of Fe^{2+} in $NH_4Co_{1-x}Fe_xCl_3$, which were obtained by diagonalizing the electronic Hamiltonian (3.45), and using the parameters from tables 4.5 and 4.7. E' is the energy of state (1) relative to the energy of state (1) at 27.0 K. E_2 [E_3] is the energy of state (2) [state (3)] minus the energy of state (1). The calculations were made assuming T_{N_1}=27 K.

and 4.7 are shown in table 4.9. The energy differences between these states are identical (within 0.1 cm^{-1}) for the two parameter sets corresponding to $\left\langle r_Q^{-3} \right\rangle$ =4.5 and 3.5 au. The energy levels of the three lowest energy states are plotted in figure 4.10. The next lowest electronic energy level lies approximately 100 cm^{-1} or 140 K higher than state (3), so that in the temperature region below T_{N_1}, states with energy greater than state (3) are ignored.

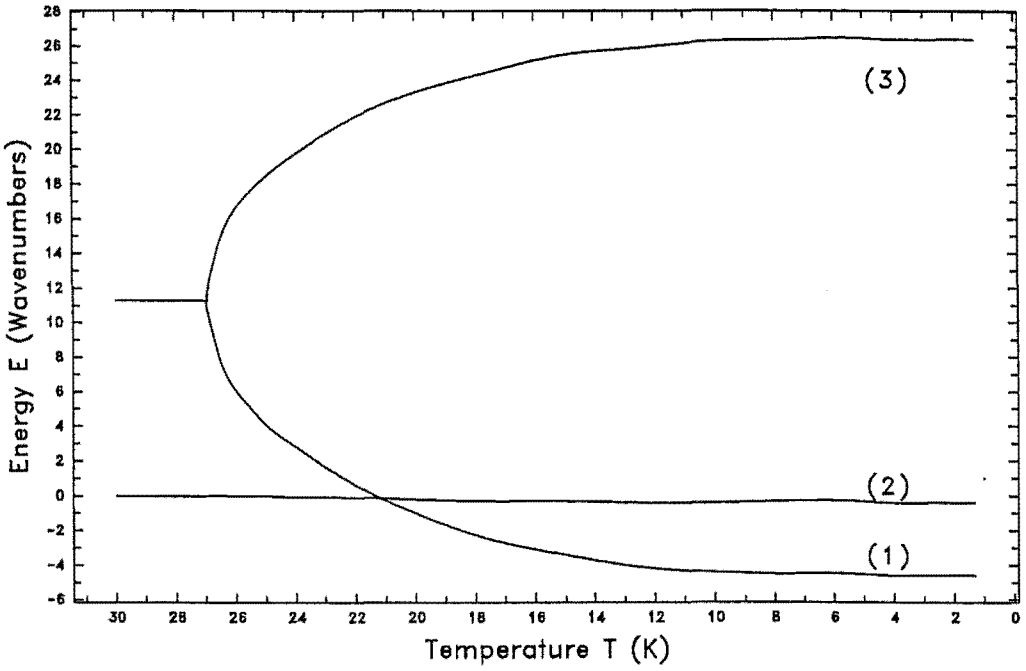

Figure 4.10: The energies of the three lowest electronic states of Fe^{2+} in $NH_4Co_{1-x}Fe_xCl_3$ taken from table 4.9. The number in brackets refers to the label of the state.

In performing fits to the Mössbauer spectra using the 3–level and combined relaxation models, E_3 was fixed to the values found in table 4.9. The values of E_2 in this table are later compared with those found by fitting spectra using the 2–level, 3–level and combined relaxation models.

The parameters from fits to the Mössbauer spectra of absorber E of $NH_4Co_{1-x}Fe_xCl_3$ using the 2–level relaxation model of section 3.2 and the program MOST are shown in table 4.10. In the 2–level relaxation model the spectra taken below T_{N_2} are fitted with relaxation between hyperfine magnetic fields of B and 0 (electronic relaxation), while for spectra taken between T_{N_2} and T_{N_1}, 1/3 of the spectrum features reversal of the magnetic hyperfine field (soliton relaxation), with

the remaining 2/3 relaxing between B and 0 (electronic relaxation).

QS could not be determined accurately from fits to the Mössbauer spectra taken between T_{N_2} and T_{N_1}. At these temperatures, the QS was fixed to values consistent with the QS found above T_{N_1} and below T_{N_2}. At temperatures above 12.5 K, the spectra cannot be fitted with an extra subspectrum, as they could below 10 K. This disappearance of the extra subspectrum coincides with the onset of solitons as shown by the fits of figure 4.8.

T (K)	χ^2	QS (mm s^{-1})	IS (mm s^{-1})	Γ (mm s^{-1})	E_2 (cm^{-1})	e rate (MHz)	sol rate (MHz)
1.3	1.12	-2.303(20)	1.223(11)	0.3^f	2.34(15)	0.32(7)	
2.8	1.13	-2.304(20)	1.222(11)	0.3^f	5.3(2)	1.16(11)	
4.2	1.68	-2.302(20)	1.218(11)	0.3^f	5.0(2)	3.1(2)	
5.3	0.93	-2.295(20)	1.222(11)	0.255^f	5.55(20)	4.5(3)	
7.5	1.16	-2.295(20)	1.216(11)	0.255^f	5.86(20)	8.5(3)	
10.0	1.19	-2.293(20)	1.222(11)	0.255^f	5.74(20)	16.7(7)	
12.5	1.23	-2.3^f	1.219(11)	0.255^f	5.12(20)	36.6(9)	45.9(15)
15.0	1.60	-2.3^f	1.223(11)	0.255^f	3.36(20)	42.8(9)	79(2)
17.5	1.53	-2.29^f	1.190(11)	0.255^f	0.1(3)	46.4(15)	100(7)
20.0	1.38	-2.29^f	1.207(11)	0.255^f	-4.1(4)	42.1(15)	137(7)
22.5	1.63	-2.29^f	1.206(11)	0.255^f	-9.1(5)	44.9(15)	164(7)
25.0	1.25	-2.29^f	1.197(11)	0.255^f	-17.5(20)	41.7(15)	204(7)
26.2	1.49	-2.29^f	1.221(11)	0.255^f	-28(3)	37.8(15)	556(7)

Table 4.10: Parameters obtained from fits to Mössbauer spectra of absorber E of $NH_4Co_{1-x}Fe_xCl_3$ using the 2–level relaxation model of section 3.2 and program MOST. In these fits, the magnetic field B was fixed to the value found from the 1.3 K spectrum, namely 22.3 T. For fits of spectra taken below 10 K, an extra subspectrum was fitted, as described in the text, with a relative area of 5.5 %. For spectra taken above 12.5 K, the relative area of the soliton subspectrum was fixed to 1/3. E rate and sol rate refer to the electronic and soliton relaxation rates respectively. The numbers in brackets indicate the uncertainty in the least significant figure(s).

It can be seen from figure 4.11 that the electronic relaxation rate below 10 K follows a $T^{1.9}$ law, much different from the T^7 law predicted by Raman relaxation in a non-Kramers ion. Thus the choice of direct relaxation for the 3–level relaxation process of section 3.3 is supported for $NH_4Co_{1-x}Fe_xCl_3$.

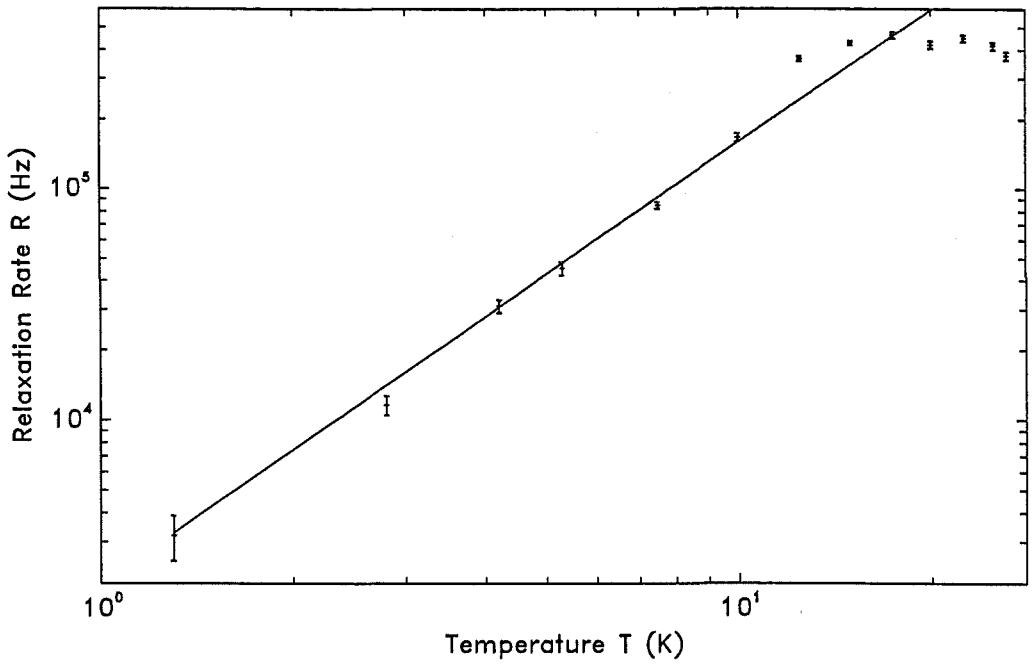

Figure 4.11: Electronic relaxation rates obtained from the fits to the Mössbauer spectra of absorber E of $NH_4Co_{1-x}Fe_xCl_3$ using the 2–level relaxation model and the program MOST. The solid line is a line of best fit to the relaxation rate below 10 K, and has the equation $R = 2000T^{1.9}$.

An estimate of the occupation probability of state (3) can be made from the predicted energies E_3 and E_2 of table 4.9. Using equation (3.27), the occupation of state (3) is 5.6 % at 17.5 K, rising to 11.6 % at 22.5 K, and 16 % at 25 K. Thus, more realistic parameter values might be expected if fits using the 3–level model are performed at temperatures above 17.5 K.

Shown in table 4.11 are the parameters obtained from fits to the Mössbauer spectra of absorber E of $NH_4Co_{1-x}Fe_xCl_3$ using the 3–level relaxation model and the computer program THREL. In the 3–level relaxation model the spectra taken below T_{N_2} are fitted with electronic relaxation between the 3 lowest Fe^{2+} electronic states, while between T_{N_2} and T_{N_1} the Fe^{2+} sites in 1/3 of the chains feature reversal of the magnetic hyperfine field (soliton relaxation) and the remaining 2/3 of the Fe^{2+} sites have 3–level electronic relaxation.

Fits to the spectra taken below 10 K show little difference between the 2 and 3–level relaxation models. This is expected since, given the energy splittings at 10 K in table 4.9, the occupation probability of state (3) is less than 0.8 % at these

T (K)	χ^2	QS (mm s^{-1})	IS (mm s^{-1})	E_2 (cm^{-1})	ω_0 (kHz $(cm^{-1})^{-3}$)	sol rate (MHz)
1.3	1.12	-2.303(20)	1.223(11)	2.3(2)	160(20)	
2.8	1.05	-2.303(20)	1.221(11)	5.2(3)	57(9)	
4.2	1.67	-2.302(20)	1.218(11)	5.0(2)	67(9)	
5.3	0.91	-2.298(20)	1.219(11)	5.5(2)	54(9)	
7.5	1.16	-2.301(20)	1.212(11)	5.9(2)	43(9)	
10.0	1.10	-2.32(20)	1.208(11)	6.1(2)	40(9)	
12.5	1.16	-2.3[f]	1.225(11)	6.4(2)	45(9)	46(2)
15.0	1.49	-2.3[f]	1.230(11)	6.0(3)	35(9)	79(2)
17.5	1.40	-2.29[f]	1.200(11)	4.6(5)	27(9)	95(3)
20.0	1.39	-2.29[f]	1.210(11)	3.3(5)	26(9)	147(4)
22.5	1.54	-2.29[f]	1.213(11)	3.8(5)	32(9)	164(4)
25.0	1.25	-2.29[f]	1.204(11)	5.8(5)	53(15)	202(8)
26.2	1.41	-2.29[f]	1.228(11)	6.0(5)	180(30)	510(40)

Table 4.11: Parameters obtained from fits to the Mössbauer spectra of absorber E of $NH_4Co_{1-x}Fe_xCl_3$ using the 3–level relaxation model and the program THREL. The linewidths were fixed to the same values as those in table 4.10, that is, 0.3 mm s^{-1} for spectra taken below 4.2 K, and 0.255 mm s^{-1} for spectra taken above 5.3 K. B was fixed to 22.3 T, and E_3 was fixed to the values found in table 4.9. ω_0 is the electronic relaxation rate parameter of equation (3.29), and sol rate is the soliton relaxation rate. For fits to spectra taken above 12.5 K, the relative area of the soliton subspectrum was constrained to be 1/3. The QS, IS, Γ, E_2, E_3 and B parameters for the soliton subspectrum were forced to be the same as those for the electronic relaxation subspectrum. The numbers in brackets indicate the uncertainty in the least significant figure(s).

temperatures. There is generally a slight improvement in the fit (χ^2 is slightly less) for fits using the 3–level relaxation model over fits using the 2–level relaxation model to spectra taken at temperatures above 15 K.

The sudden decrease of E_2 from $\approx$ 5.3 cm^{-1} above 2.8 K to 2.34 cm^{-1} at 1.3 K is not predicted in table 4.9. For the purposes of determining the value of J_{eff} in table 4.7, a value of ≈ 4 cm^{-1} was chosen as being a representative splitting.

It is noted that the electronic and soliton relaxation rates from the 2–level relaxation model fits of table 4.10 are of the same order at temperatures between 12.5 K and 17.5 K. Thus in this temperature range, the lineshape for the soliton subspectrum predicted by the combined relaxation model should be more appropriate than

that predicted by the 3–level relaxation model.

Table 4.12 shows the parameters obtained from fitting the Mössbauer spectra of absorber E of $NH_4Co_{1-x}Fe_xCl_3$ above 12.5 K using the combined relaxation model of section 3.4 and the program SOEL. In this model, for temperatures below T_{N_2}, 3–level electronic relaxation occurs in all sites, as for the 3–level relaxation model, so the fitted parameters at these temperatures are not given in table 4.12. At temperatures between T_{N_2} and T_{N_1} field reversal or soliton relaxation occurs at Fe^{2+} sites in 1/3 of the chains and 3–level electronic relaxation occurs in all the Fe^{2+} sites.

T (K)	χ^2	IS (mm s^{-1})	E_2 (cm^{-1})	ω_0 (kHz $(cm^{-1})^{-3}$)	sol rate (MHz)
12.5	1.16	1.219(11)	6.5(2)	46(9)	20(2)
15.0	1.57	1.224(11)	6.1(3)	36(9)	32(3)
17.5	1.50	1.192(11)	4.8(5)	28(9)	33(4)
20.0	1.34	1.207(11)	3.5(5)	27(9)	37(4)
22.5	1.60	1.206(11)	3.7(5)	32(9)	37(5)
25.0	1.26	1.20(1)	5.5(5)	54(15)	28(8)
26.2	1.54	1.221(11)	5.6(5)	170(30)	110(40)

Table 4.12: Fitted parameters for the Mössbauer spectra of absorber E of $NH_4Co_{1-x}Fe_xCl_3$. The combined relaxation model of section 3.4 was used with the program SOEL. The linewidths and QS were fixed to the same values as those in tables 4.10 and 4.11. B was fixed to 22.3 T, and E_3 was fixed to the values found in table 4.9. Sol rate refers to the soliton relaxation rate π_s of table 3.2. The relative area of the soliton subspectrum was fixed at 1/3. The QS, IS, Γ, E_2, E_3 and B parameters for the soliton subspectrum were forced to be the same as those for the electronic relaxation subspectrum. The numbers in brackets indicate the uncertainty in the least significant figure(s).

At temperatures above 12.5 K, the χ^2 parameter obtained from fits using the combined relaxation model shows no significant improvement over that obtained from fits using the 3–level relaxation model. This result indicates that both models have enough parameters to enable the spectra to be fitted well.

For the various models, the energy of state (1) relative to state (2) is plotted in figure 4.12. At temperatures below 10 K fits using the 2–level, 3–level and combined

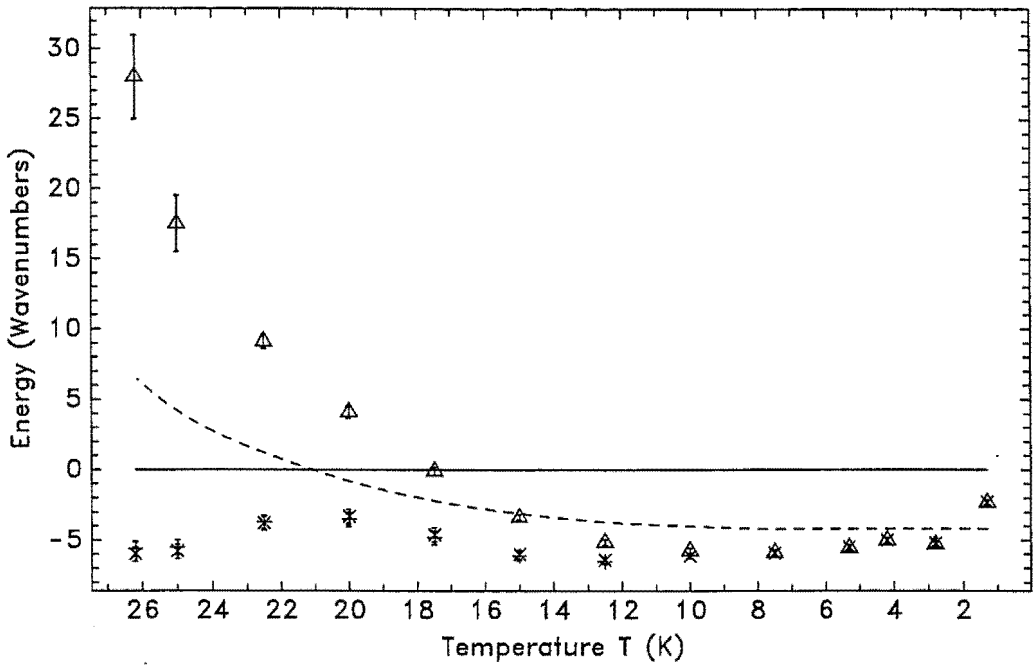

Figure 4.12: The energy of state (1) relative to state (2) (the line at zero energy). The parameter E_2, which is the energy of state (2) minus the energy of state (1), is given by the negative of the energy scale. The dashed curve is taken from table 4.9, the $\triangle$ are from fits using the 2–level relaxation model (table 4.10), the $\times$ are from fits using the 3–level model (table 4.11), and the $+$ are from fits using combined relaxation (table 4.12).

relaxation models yield the same E_2 parameter. This is expected at these temperatures given the low occupation probability of state (3) implied by the value of E_3 in table 4.9.

For fits to spectra taken at temperatures above 17.5 K using the 2–level model, the parameter E_2 is much more negative than predicted in table 4.9. This is consistent with state (3) becoming more populated, since the effect of fast relaxation between a well populated magnetic state (1) and a barely populated magnetic state (3) producing the opposite sign $B_{\rm hf}$, is to reduce the overall splitting of the Mössbauer spectrum by a factor of twice the Boltzmann occupation probability of the upper magnetic state (3). This narrowing of the spectrum can be achieved within the 2–level relaxation model by increasing the population of the non–magnetic state (2), that is, making E_2 more negative. The deviation of the fitted E_2 from the predicted E_2 becomes larger at higher temperatures, when state (3) becomes more populated.

The large values of E_2 of -17.5 cm^{-1} and -28 cm^{-1} at 25 K and 26.2 K respectively from fits using the 2–level relaxation model are considered to be artifacts of the 2–level relaxation model, since they are much larger than the singlet–doublet splitting of 11.3 cm^{-1} found from the crystal field fits of section 4.2.1. Also, there is a large uncertainty for parameters determined from these spectra, since above 25 K the Mössbauer spectra of $NH_4Co_{1-x}Fe_xCl_3$ have a lack of structure.

The energy splitting parameter E_2 obtained from fits using both the 3–level and combined relaxation models is the same within uncertainty. The E_2 parameter of the 3–level and combined relaxation models follows the trend of the E_2 parameter given in table 4.9 up to 20 K. At temperatures of 22.5 K and above, E_2 is much more positive than the prediction of table 4.9. This effect would be produced if E_3 was fixed to a value which was too low. The effect of relaxation between B and $-B$ on the Mössbauer spectrum is to produce a spectrum whose width corresponds to an effective $B_{\rm hf}$ which has a value between B and the average by occupation of B and $-B$ depending on the relaxation rate. Thus increasing the occupation probability of state (3) (which gives a $B_{\rm hf}$ of opposite sign to state (1)), decreases the effective $B_{\rm hf}$, and causes the Mössbauer spectrum to become narrower. To counteract this effect, the occupation probability of the magnetic state (1) is increased, which increases the width of the Mössbauer spectrum by the same argument as for the 2–level relaxation model above. Thus, under the parameter sets of the fits in tables 4.11 and 4.12, at temperatures between 22 K and 26 K, the effect of decreasing E_3 is to increase E_2. That is, in fitting these spectra, the effect of increasing the occupation probability of the higher magnetic state (3) is also to increase the occupation probability of the lower magnetic state (1).

The splitting E_3 of the magnetic states is proportional to $\langle S_{\rm Co}\rangle$ of equation (3.47). Since broadening of the Mössbauer spectra occurs at temperatures up to 60 K in $NH_4Co_{1-x}Fe_xCl_3$, there is short–range ordering along the chains of Co^{2+} ions up to approximately 60 K. This indicates that $\langle S_{\rm Co}\rangle$ is not 0 at T_{N_1} as predicted by equation (3.47), and thus the splitting of the magnetic states at temperatures near T_{N_1} is larger than that predicted by the $S = 1/2$ Brillouin function. This deviation of $\langle S_{\rm Co}\rangle$ from Brillouin function behaviour may account for the low observed value of E_2 above 22 K obtained from fits to the spectra using the 3–level and combined relaxation models shown in figure 4.12, and also supports the hypothesis that E_3

should be fixed to a higher value than that predicted in table 4.9.

The electronic relaxation rate parameter ω_0 (see equation (3.29)) obtained from fits using either the 3–level or combined relaxation models are the same within uncertainties. Assuming that the matrix elements of strain, the density of the crystal, and the speed of sound in the crystal are all independent of temperature, then ω_0 should be independent of temperature. Over the temperature range 2.8 K to 25 K ω_0 obtained from fits using the 3–level and combined relaxation models varies by a factor of ≈ 2. Apart from the above assumptions that ω_0 has no explicit temperature dependence, deviations from constant ω_0 over the range 1.3 K to 15 K could be due either to error in the values of E_2 and E_3, or to a contribution to the electronic relaxation rate other than the direct process (for example the Raman process). This variation may be considered small in comparison to the variations in the electronic relaxation rate obtained from fits using the 2–level relaxation model. These relaxation rates increase by a factor of more than 100 over the temperature range from 1.3 K to 15 K.

At 1.3 K and 26.2 K there is a marked departure of ω_0 from the range 27 to 67 kHz $(\mathrm{cm}^{-1})^{-3}$. The 26.2 K spectrum has a lack of structure, which allows a variety of different parameter sets to be fitted. It is possible that a value of ω_0 of less than 67 kHz $(\mathrm{cm}^{-1})^{-3}$ could be obtained. However, given the uncertainty in the expected values of E_2 and E_3 at this temperature, exhaustive fitting of all possible parameter sets was not attempted. It is also possible, given that the only determination of T_{N_1} is from Mössbauer effect measurements (Amit *et al* 1970) with T_{N_1}=(27±4) K, that at 26.2 K more than 1/3 of the sites are subject to moving domain walls. A determination of T_{N_1} using neutron diffraction may clarify this issue.

The value of ω_0=160 kHz $(\mathrm{cm}^{-1})^{-3}$ at 1.3 K is unexplained, but the high value may be an artefact of the "extra lines", and is affected by the value of E_2 which is anomalously low at this temperature.

Fits without a soliton relaxation subspectrum to the Mössbauer spectra of $NH_4Co_{1-x}Fe_xCl_3$ taken at 12.5 K and 15 K could not be achieved. If, however, a soliton relaxation subspectrum with a relative area fixed to 1/3 is added to any of the 2–level, 3–level or combined relaxation models good fits to the Mössbauer

spectra could be obtained at these temperatures, with B = 22.3 T. This is evidence that some relaxation process in addition to electronic relaxation is occurring at these temperatures, and is consistent with the presence of solitons in 1/3 of the Co^{2+} chains.

For the Mössbauer spectra taken above 17.5 K a marked improvement in fit was apparent when a soliton subspectrum with a relative area of 1/3 was included. Good fits using any one of the 2, 3 or combined relaxation models to the Mössbauer spectra over the range 12.5 K to 26.2 K were obtained, with B fixed to 22.3 T. Although adequate fits to the Mössbauer spectra above 17.5 K could be obtained with no soliton relaxation subspectrum if $B_{\rm hf}$ was allowed to decrease, this solution was discarded for two reasons. Firstly, a soliton relaxation subspectrum was definitely necessary for adequate fits to the 12.5 and 15 K spectra, and a solitons must be present at all higher temperatures (less than the short–range ordering temperature). Secondly, the temperature dependence of B given in table 4.8, calculated from the Fe^{2+} wavefunctions using equation (3.44), showed a slight increase of B with temperature, contrary to the temperature dependence found from fitting the Mössbauer spectra without including a soliton relaxation subspectrum.

When fits to the Mössbauer spectra of $NH_4Co_{1-x}Fe_xCl_3$ taken at temperatures below 10 K were attempted with the relative area of the soliton subspectrum fixed to 1/3, fits could only be obtained when the soliton relaxation rate was very slow (so that the soliton subspectrum had nearly the same shape as the electronic relaxation subspectrum), or very fast (producing 2 quadrupole split lines) with the soliton relaxation rate increasing as the temperature decreased, reflecting sharper absorption lines. These results, and the discontinuity in the soliton relaxation rate between fits made to spectra taken below 10 K and those made to spectra taken above 12.5 K, are taken as evidence that solitons do not persist in $NH_4Co_{1-x}Fe_xCl_3$ at temperatures less than 10 K.

Thus, a consistent set of soliton relaxation rate and B parameters can be obtained using any of the 2–level, 3–level or combined relaxation models if the spectra taken below 10 K are fitted with electronic relaxation only, while the spectra taken above 12.5 K are fitted with 2 subspectra, the soliton relaxation subspectrum with relative area of 1/3, and the electronic relaxation subspectrum with a relative area of 2/3.

The soliton relaxation rates obtained from fitting $NH_4Co_{1-x}Fe_xCl_3$ Mössbauer

spectra using the 2–level, 3–level and combined relaxation models are plotted in figure 4.13. It can be seen that the relaxation rates obtained from fits using the 2–

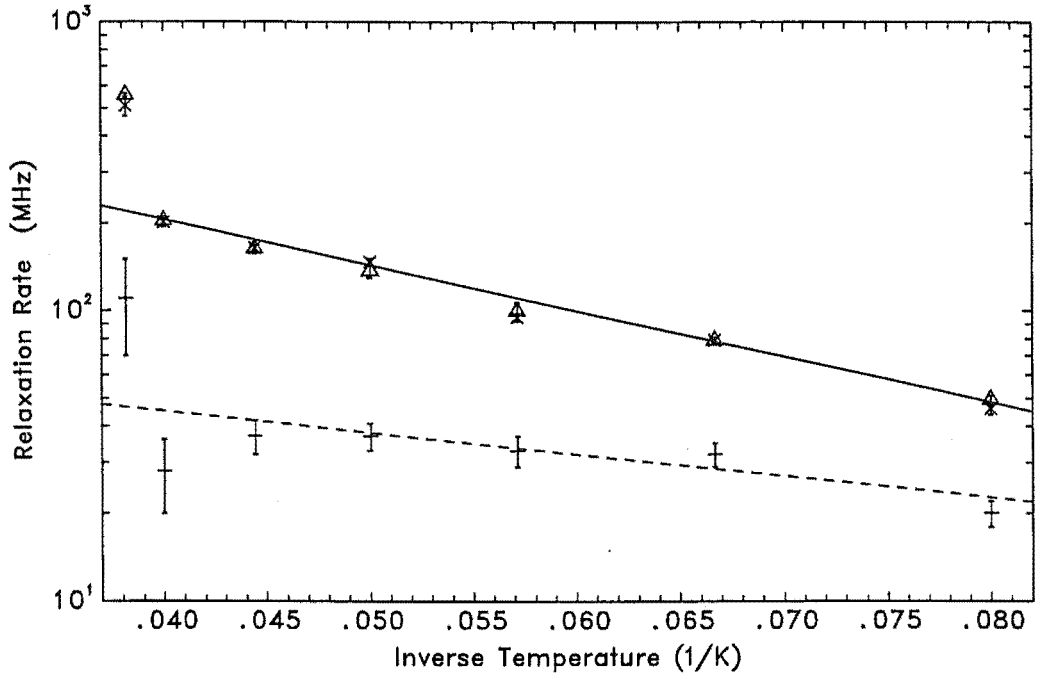

Figure 4.13: The soliton relaxation rates obtained from fits to Mössbauer spectra of $NH_4Co_{1-x}Fe_xCl_3$ using the 2–level (△), 3–level (×), and combined (+) relaxation models. The solid line is a line of best fit to the relaxation rate obtained from the 2–level and 3–level relaxation models. The dashed line is a line of best fit for the relaxation rate obtained from fits using the combined relaxation model.

level and 3–level relaxation models are identical. The only parameter of the soliton relaxation subspectrum which was allowed to vary independently from the electronic relaxation subspectrum was the soliton relaxation rate, so the lineshape of the soliton subspectrum is the same for fits using either of the two models. The goodness of fit is very similar for both models, so the electronic relaxation subspectrum must be very similar. This indicates that the only significant effect of incorporating the third state into the 2–level relaxation model is to change the value of E_2, as seen in figure 4.12.

The soliton relaxation rate obtained by fitting the Mössbauer spectra using the combined relaxation model is less than 1/2 that obtained by fitting the spectra using the 2–level or 3–level relaxation models. This decrease can be understood by the following reasoning. The electronic relaxation subspectrum is broader (width

$\simeq$ 6 mm s^{-1}) than the soliton subspectrum (width $\simeq$ 3 mm s^{-1}), and also has more distinguishable absorption lines than the soliton subspectrum (see figure 4.8). Therefore the lineshape of the electronic relaxation subspectrum is determined at least partially by features of the Mössbauer spectrum which are not affected by the soliton subspectrum. This means that the lineshape of the soliton subspectrum is constrained to be the difference between the spectrum and the relatively well determined lineshape of the electronic relaxation subspectrum. Thus the effect of adding electronic relaxation to the soliton subspectrum will be to reduce the soliton relaxation rate to such a value that the lineshape of the soliton relaxation spectrum is essentially unchanged.

The soliton relaxation rate R can be calculated from the theory for an ideal soliton–gas in a nearly Ising chain (Smit *et al* 1989) as the product of the soliton density and the thermally averaged soliton velocity,

$$R(T) = \frac{8k}{h} T \sinh\left(\frac{2\varepsilon J}{kT}\right) \exp\left(\frac{-J}{kT}\right) \tag{4.1}$$

where J and ε are the Co–Co intra-chain exchange parameters of equation (1.1).

J and ε are taken to be 75 K and 0.12 respectively, the values for $CsCoCl_3$ (Achiwa 1969, Tellenbach 1978, and Yoshizawa *et al* 1981). This assumption is made because the NH_4^+ and Cs^+ ions are considered to act only as spacers between the chains of Co^{2+} ions and their surrounding Cl^- ions. Thus the effect due to the substitution of Cs^+ with NH_4^+ on the intra–chain super–exchange interaction between the Co^{2+} ions is expected to be small. To justify this assumption it is noted that the exchange parameters of the isomorphous salt $RbCoCl_3$ are similar to these values: Lockwood *et al* (1983) measured J and ε using Raman scattering techniques, and obtained approximately 71 K and 0.1 respectively. A further justification of this assumption is that the Néel temperatures for $CsCoCl_3$ and NH_4CoCl_3 are similar.

For J=75 K, and ε=0.12, and in the temperature range 12.5 K to 25 K, a plot of $\ln R(T)$ versus $1/T$ where $R(T)$ is given by equation (4.1) yields a straight line to within 1 %, with R(12.5 K)=1.03$\times 10^4$ MHz, and R(25 K)=1.63$\times 10^5$ MHz. The equation of the straight line which approximates R over this temperature range is

$$R = 2.51 \times 10^6 \exp\left(\frac{-68.8}{T}\right) ,$$

where T is in Kelvin and R is in MHz.

In contrast to the theoretical prediction, the relaxation rates found experimentally were $R(12.5\text{ K})=(46\pm2)$ MHz and $R(25\text{ K})=(202\pm8)$ MHz from fits to the Mössbauer spectra of $NH_4Co_{1-x}Fe_xCl_3$ using the 2 and 3–level relaxation models, and $R(12.5\text{ K})=(20\pm2)$ MHz and $R(22.5\text{ K})=(37\pm5)$ MHz from fits using the combined relaxation model. These results are 2 to 3 orders of magnitude less than the prediction based on the theory of the ideal soliton–gas.

The equation of the line of best fit to the soliton relaxation rate determined from fits using the 2–level and 3–level relaxation models to the Mössbauer spectra of $NH_4Co_{1-x}Fe_xCl_3$ (the solid line in figure 4.13) is

$$R = (880 \pm 200)\exp\left(\frac{-(36 \pm 4)}{T}\right) .$$

The dashed line in figure 4.13 is a line of best fit for the soliton relaxation rate as determined by fits using the combined relaxation model. It has the equation

$$R = (90 \pm 30)\exp\left(\frac{-(17 \pm 7)}{T}\right) .$$

If the ideal soliton–gas model (equation (4.1)) describes the experimentally determined soliton relaxation rates, then the values of J and ε in NH_4CoCl_3 are much less than in $CsCoCl_3$. Given that J and ε are expected to be similar for these two compounds, a more likely explanation is that equation (4.1) does not describe the experimentally determined soliton relaxation rates. It is possible that the soliton relaxation rates determined from the Mössbauer spectra of $NH_4Co_{1-x}Fe_xCl_3$ are not the product of the soliton density and the thermally averaged soliton velocity. This would occur if the calculated electronic relaxation rates were inaccurate (as discussed in section 3.3, and on page 90) since this would in turn affect the soliton relaxation rate determined from the spectrum, or if a certain proportion of the solitons were undetected by the Mössbauer effect, due to the iron–soliton interaction described in section 3.7.

The difference in the rates obtained from equation (4.1) and experiment could also be due to the ideal soliton–gas not applying to solitons in $NH_4Co_{1-x}Fe_xCl_3$. The density of solitons and thermally averaged soliton velocity are calculated in the low–temperature limit, where the solitons are treated as non–interaction quasi–particles. At the temperatures probed in this experiment some deviation from the ideal soliton–gas may be expected because of interactions between solitons. The low

soliton relaxation rates obtained in NMR, μ^+ spin resonance, and NIS experiments on $CsCoCl_3$ provide evidence for a deviation from ideal soliton–gas behaviour (see section 4.3).

In summary, the crystal field, spin–orbit, and magnetic exchange Hamiltonian parameters, and the Fermi contact effective field parameter obtained for Fe^{2+} in $NH_4Co_{1-x}Fe_xCl_3$ provide a framework within which the Mössbauer spectra of $NH_4Co_{1-x}Fe_xCl_3$ taken below 26.2 K could be analysed with three different relaxation models. Good fits to the Mössbauer spectra over the whole temperature range below 26.2 K were obtained using any of the three relaxation models.

The Mössbauer spectra at temperatures between 12.5 K and 26.2 K exhibit extra relaxation consistent with a reversal of the magnetic hyperfine field, presumably due to solitons. The "soliton" relaxation rate is 2–3 orders of magnitude slower than the theoretical prediction. The approximation of the 2 and 3–level relaxation models that the soliton relaxation dominates the electronic relaxation in the frustrated chains is seen to be poor (see table 4.10) at 12.5 K to 17.5 K. Although the combined relaxation model avoids this approximation, the soliton relaxation rate obtained is even slower.

Below 10 K, soliton relaxation is absent from the Mössbauer spectra, but weak "extra" lines are observed. The 1.3 K spectrum has an unusually small splitting between the lower magnetic state and the non–magnetic state. The decrease of this splitting from its value at temperatures above 2.8 K is unexplained, and is not predicted by mean field theory.

4.3 $CsCo_{1-x}Fe_xCl_3$

The parameters of the electronic Hamiltonian of Fe^{2+} in $CsCo_{1-x}Fe_xCl_3$ were obtained in the same way as those of Fe^{2+} in $NH_4Co_{1-x}Fe_xCl_3$ given in section 4.2.1. The energy splittings and magnetic hyperfine fields produced by the three lowest electronic states of Fe^{2+} in $CsCo_{1-x}Fe_xCl_3$ were established. Using these results the Mössbauer spectra taken at temperatures below T_{N_1} were fitted using the 2–level, 3–level, and combined relaxation models, and the results from these fits are compared.

Mössbauer spectra of a powder sample of $CsCo_{1-x}Fe_xCl_3$ with x=0.01 have been

previously recorded in a study in this laboratory (Ward *et al* 1987). The Mössbauer spectra taken above T_{N_1} consist of a quadrupole split pair of absorption lines, similar to those of $NH_4Co_{1-x}Fe_xCl_3$ in its paramagnetic phase.

The unequal intensities of the quadrupole split absorption lines of spectra taken above 80 K enabled a determination of $< \sin^2 \alpha >_{av}$ for the preferentially oriented powder in the absorber. Using the same method as for NH_4FeCl_3 given in section 4.1.1, $< \sin^2 \alpha >_{av} = 0.79 \pm 0.02$, and the sign of V_{zz} is negative. For fits to spectra taken below T_{N_1}, $< \sin^2 \alpha >_{av}$ was fixed to 0.79. Fits to the spectra taken below T_{N_2} confirm the sign of V_{zz}, since these spectra cannot be fitted with $V_{zz} > 0$.

The values of QS for the spectra taken above 25 K were fitted using the same method as for NH_4FeCl_3 (section 4.1.1). The crystal field and spin–orbit parameters given in table 4.13 are the same as those obtained by Ward *et al* (1987). The magnetic parameters J_{eff} and B_c were determined by the method used for $NH_4Co_{1-x}Fe_xCl_3$ in section 4.2.2. J_{eff} in this thesis was obtained using the $S = 1/2$ Brillouin function to describe the magnetisation of the Co^{2+} chains in $CsCo_{1-x}Fe_xCl_3$ (see section 3.5), whereas an $S = 3/2$ Brillouin function was used by Ward *et al* (1987). The two functions have very similar shapes, the main difference being that the $S = 1/2$ function is 1/3 the magnitude of the $S = 3/2$ function. This means that J_{eff} obtained in this work is three times larger than J_{eff} obtained by Ward *et al* (1987).

J_{eff} was chosen so that the energy splitting of the lowest two states at 1.9 K was $E_2 = 2.9$ cm^{-1}, the value found from fits to the 1.9 K Mössbauer spectrum using the 2–level and 3–level relaxation models (see figure 4.17 and table 4.16). The energies of the electronic states of Fe^{2+} in $CsCo_{1-x}Fe_xCl_3$ were calculated by diagonalizing the electronic Hamiltonian with the crystal field, spin–orbit, and magnetic parameters of table 4.13. The effective ordering temperature for the $S = 1/2$ Brillouin function was taken to be T_{N_1}=21.2 K, from a combination of three measurements (Melamud *et al* 1974, Mekata and Adachi 1978, and Yoshizawa and Hirakawa 1979). The results for the three lowest energy states of Fe^{2+} are shown in table 4.14. For fits to the spectra taken below T_{N_1} using the 3–level and combined relaxation models, E_3 was fixed to these values. The next lowest electronic level lies approximately 75 cm^{-1} (105 K) higher than state (3), so that at temperatures below T_{N_1}, states with energy greater than state (3) are not significantly populated and are ignored

parameter	value
B_c^4	-10150^f cm^{-1}
B_0^2	-2400^f cm^{-1}
B_0^4	2650(30) cm^{-1}
λ	-67(3) cm^{-1}
$\langle r_Q^{-3} \rangle$	4.08(30) au
$\langle r^{-3} \rangle$	4^f au
$\frac{1}{2}\|e\|QV_{zz}^{lat}$	-0.41(8) mm s^{-1}
J_{eff}	-34.0(2) cm^{-1}
B_c	-49.5(1) T

Table 4.13: Values of the crystal field, spin–orbit, and magnetic parameters of the Hamiltonian (3.39) for Fe^{2+} in $CsCo_{1-x}Fe_xCl_3$. The values were determined by fitting the QS of Mössbauer spectra of $CsCo_{1-x}Fe_xCl_3$ taken above T_{N_1}. Values which were fixed in the fit to QS are marked with a superscript f. The numbers in brackets indicate the uncertainty in the least significant figure(s).

T (K)	E_2 cm^{-1}	E_3 cm^{-1}
1.15	2.91	37.33
1.9	2.91	37.33
4.2	2.91	37.33
5.5	2.90	37.29
6.4	2.86	37.23
8.6	2.62	36.75
11.0	1.96	35.45
14.6	-0.13	29.61
17.9	-3.91	23.77
20.1	-8.49	14.66
21.2	-15.83	0

Table 4.14: The energy splittings E_2 and E_3 were calculated by diagonalizing the electronic Hamiltonian (3.45), using the S=1/2 Brillouin function and parameters from table 4.13. E_2 [E_3] is the energy of state (2) [state (3)] minus the energy of state (1). The calculations were made assuming that the effective ordering temperature was T_{N_1}=21.2 K.

in the relaxation models used.

The magnetic hyperfine field of the lowest three states, calculated using the above eigenstates and the magnetic parameters B_c and $\langle r^{-3} \rangle$, is in the z (chain) direction. The results are shown in table 4.15, and indicate that a reasonable approximation

T (K)	$B_{hf}(1)$ (T)	$B_{hf}(2)$ (T)	$B_{hf}(3)$ (T)
1.15	24.8	0.3	-26.1
17.0	25.0	0.2	-25.8

Table 4.15: The B_{hf} for the three lowest–energy states of Fe^{2+} in $CsCo_{1-x}Fe_xCl_3$ calculated using equation (3.44) with the parameter set of table 4.13. The calculations were made assuming that the effective ordering temperature was T_{N_1}=21.2 K. The states are labelled according to their order at 1.15 K, with state (1) having the lowest energy at 1.15 K.

for the z component of magnetic hyperfine field for the three lowest–energy states is: 24.8 T (state (1)), 0 T (state (2)), and -24.8 T (state (3)) for all temperatures. This differs from the procedure of Ward *et al* (1987) in which the magnitude of the field for states (1) and (3) was B where B was allowed to vary.

The Mössbauer spectra of $CsCo_{1-x}Fe_xCl_3$ taken at temperatures below T_{N_1} are shown in figures 4.14 and 4.15. No extra lines are visible in any of the spectra of $CsCo_{1-x}Fe_xCl_3$, in contrast with $NH_4Co_{1-x}Fe_xCl_3$ which has extra lines in the spectra taken at temperatures below 10 K. The signal to noise ratio of these spectra is lower than that of the $NH_4Co_{1-x}Fe_xCl_3$ spectra of section 4.2.2 partially as a consequence of attenuation of the gamma rays by the heavy Cs atoms in $CsCo_{1-x}Fe_xCl_3$.

Table 4.16 shows the parameters obtained from fitting the Mössbauer spectra of $CsCo_{1-x}Fe_xCl_3$ taken below T_{N_1} using the 2–level relaxation model of section 3.2 and the program MOST. The temperature variation of the electronic relaxation rates are further displayed in figure 4.16. The 1.15 and 1.9 K Mössbauer spectra show the same anomalous behaviour as the 1.3 K spectrum of $NH_4Co_{1-x}Fe_xCl_3$. Ignoring the 1.15 K and 1.9 K spectra, the electronic relaxation rate below 14.6 K follows a $T^{4.88}$ law, significantly less than the T^7 law predicted by the Raman relaxation process for a non–Kramers ion. Thus electronic relaxation by the direct process of section 3.3 is used in the fitting the $CsCo_{1-x}Fe_xCl_3$ spectra using the 3–level and combined relaxation models.

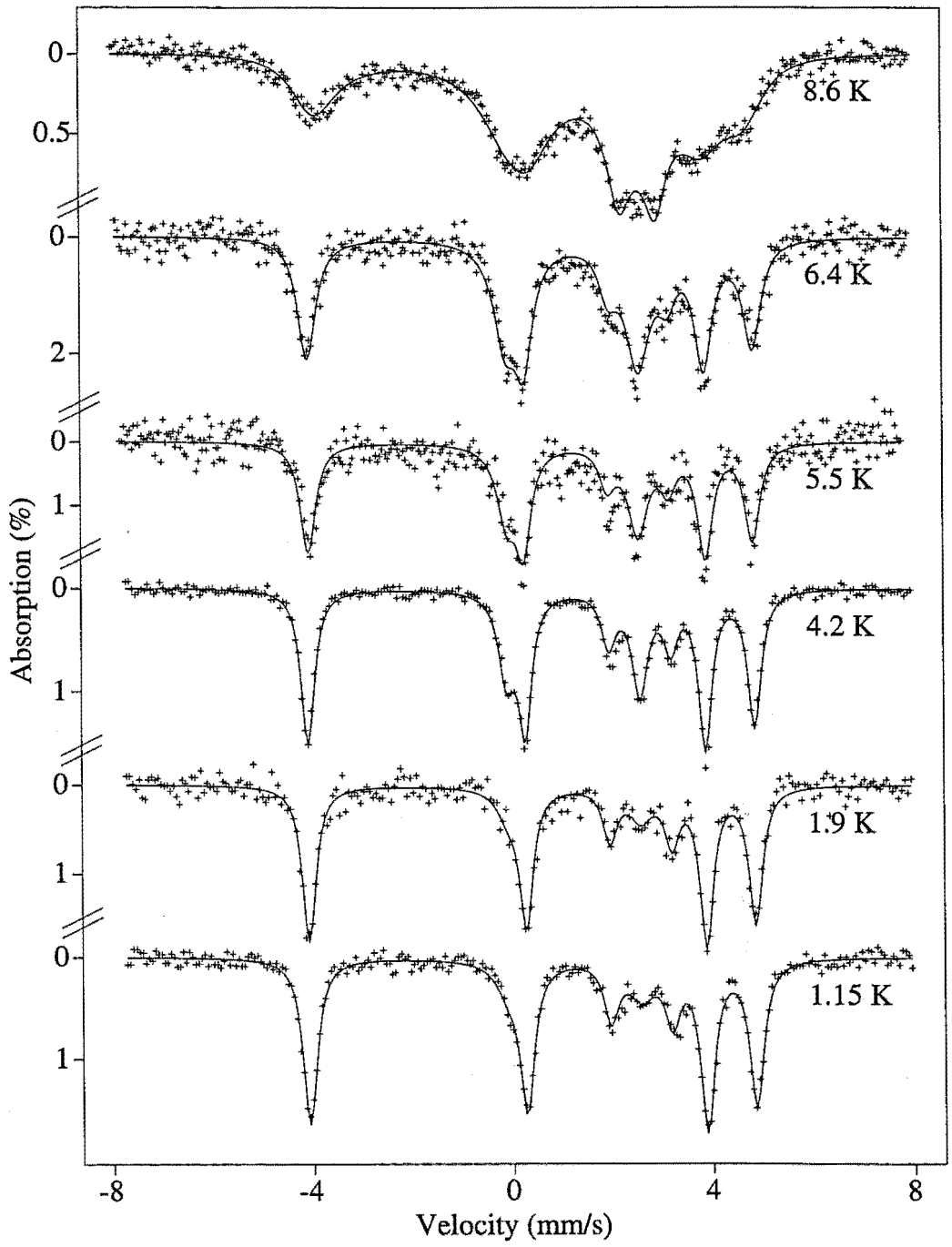

Figure 4.14: Mössbauer spectra of $CsCo_{1-x}Fe_xCl_3$. The fitted curve is that calculated using the 3–level electronic relaxation as for the 3–level relaxation model described in section 3.3.

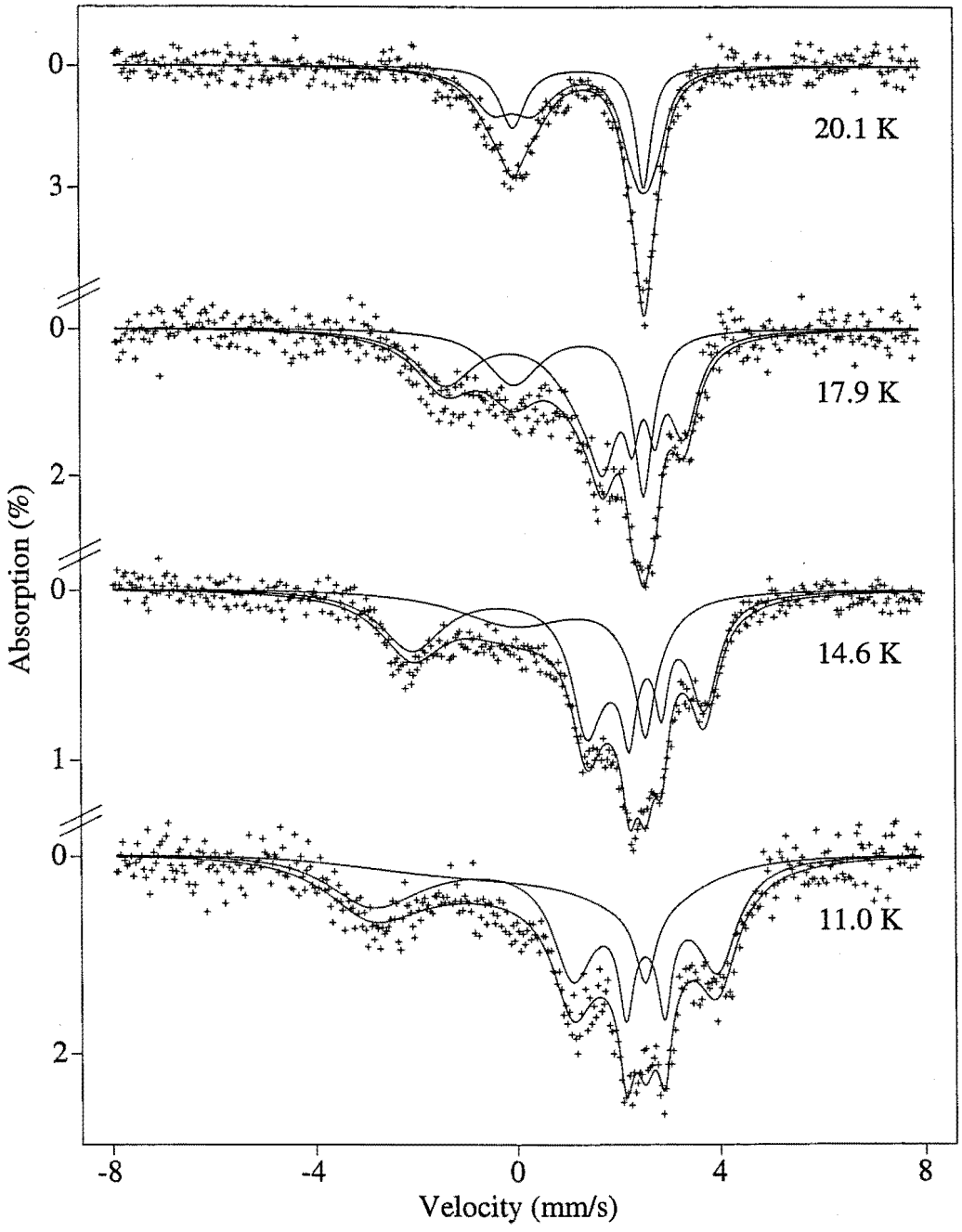

Figure 4.15: Mössbauer spectra of $CsCo_{1-x}Fe_xCl_3$. The fitted curve is the sum of two subspectra calculated according to the combined relaxation model of section 3.4. In this model the electronic relaxation subspectrum is calculated assuming 3–level electronic relaxation, and has a relative area of 2/3. The soliton subspectrum has a relative area of 1/3, and is calculated assuming combined soliton and 3–level electronic relaxation.

T (K)	χ^2	QS (mm s^{-1})	IS (mm s^{-1})	E_2 (cm^{-1})	e rate (MHz)	sol rate (MHz)
1.15	1.03	-2.666(23)	1.239(11)	1.53(15)	0.44(7)	
1.9	1.07	-2.667(23)	1.240(11)	2.7(2)	0.30(7)	
4.2	1.65	-2.669(23)	1.238(11)	3.4(2)	0.22(7)	
5.5	1.25	-2.63(2)	1.236(11)	3.3(2)	0.58(7)	
6.4	1.27	-2.661(23)	1.240(11)	2.9(2)	1.07(16)	
8.6	1.27	-2.64^f	1.235^f	1.8(2)	5.3(4)	
11.0	1.23	-2.63^f	1.23^f	3.2(3)	23(1)	39(1)
14.6	1.32	-2.60(3)	1.23(2)	0.2(3)	41(1)	79(2)
17.9	0.88	-2.57(3)	1.23(2)	-7.3(3)	37(1)	190(4)
20.1	0.93	-2.60(3)	1.24(2)	-25(5)	11(5)	500(20)

Table 4.16: Parameter values obtained from fits to Mössbauer spectra of $CsCo_{1-x}Fe_xCl_3$ using the 2–level relaxation model of section 3.2 and the program MOST. In these fits, the linewidth was fixed to 0.3 mm s^{-1}, and the magnetic hyperfine field B was fixed to the value found from free fits to the spectra taken below 4.2 K, namely 24.8 T. For spectra taken above 11.0 K, the relative area of the soliton subspectrum was fixed to 1/3. E rate and sol rate refer to the electronic and soliton relaxation rates respectively. The parameters QS, IS and B were fixed to be the same in both subspectra. The parameters marked with superscript f were fixed in the fit.

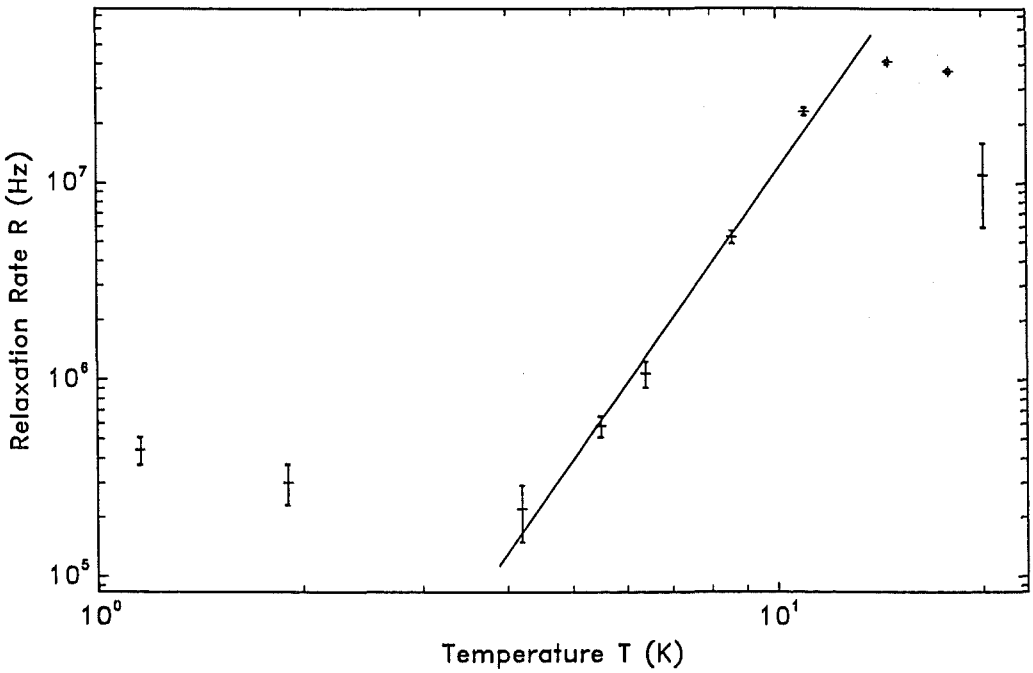

Figure 4.16: Electronic relaxation rates obtained from the fits to the Mössbauer spectra of $CsCo_{1-x}Fe_xCl_3$ using the 2–level relaxation model. The solid line has the equation $R = 240T^{4.88}$.

Using the predicted relative energies of states (1), (2), and (3) given in table 4.14, and equation (3.27), the occupation probability of state (3) is estimated to be 2.6 % at 14.6 K and 5.9 % at 17.9 K. Therefore the parameter values obtained from fits using the 3–level and combined relaxation models should be similar to those obtained from fits using the 2–level relaxation model.

Shown in table 4.17 are the parameters obtained from fits to the Mössbauer spectra of $CsCo_{1-x}Fe_xCl_3$ using the 3–level relaxation model of section 3.3 and the program THREL .

T (K)	χ^2	QS (mm s^{-1})	IS (mm s^{-1})	E_2 (cm^{-1})	ω_0 (kHz $(cm^{-1})^{-3}$)	sol rate (MHz)
1.15	1.03	-2.666(23)	1.239(11)	1.5(2)	410(20)	
1.9	1.07	-2.667(23)	1.240(11)	2.7(2)	56(10)	
4.2	1.65	-2.670(23)	1.238(11)	3.4(2)	85(12)	
5.5	1.25	-2.63(4)	1.236(11)	3.4(2)	14(10)	
6.4	1.27	-2.661(23)	1.240(11)	2.9(2)	25(8)	
8.6	1.13	-2.59(3)	1.237(11)	1.7(2)	73(12)	
11.0	1.27	-2.64^f	1.235^f	3.5(3)	70(12)	39(5)
14.6	1.32	-2.59(4)	1.24(2)	2.0(3)	51(12)	83(7)
17.9	0.88	-2.57(4)	1.24(2)	-2.7(3)	32(8)	181(12)
20.1	0.95	-2.59(4)	1.247(2)	-18(5)	8(2)	600(140)

Table 4.17: Parameters obtained from fitting the Mössbauer spectra of $CsCo_{1-x}Fe_xCl_3$ using the 3–level relaxation model of section 3.3 and the program THREL. In these fits, the magnetic hyperfine field B and Γ were fixed to 22.3 T and 0.255 mm s^{-1} respectively, and E_3 was fixed to the values shown in table 4.14. For spectra taken above 11.0 K, the relative area of the soliton subspectrum was fixed to 1/3. ω_0 is the electronic rate parameter and sol rate refers to the soliton relaxation rate. The parameters QS, IS, E_2, E_3 and B were constrained to be the same for both subspectra. The parameters marked with superscript f were fixed in the fit, and the numbers in brackets indicate the uncertainty in the least significant figure(s).

The electronic and soliton relaxation rates from fits using the 2–level relaxation model at 11.0 K and 14.6 K (table 4.16) are of the same order of magnitude. Under these conditions, the combined relaxation model should be appropriate. Table 4.18 shows the parameters obtained from fitting $CsCo_{1-x}Fe_xCl_3$ Mössbauer spectra above 11.0 K using the combined relaxation model and the program SOEL.

T (K)	χ^2	QS (mm s^{-1})	IS (mm s^{-1})	E_2 (cm^{-1})	ω_0 (kHz $(cm^{-1})^{-3}$)	sol rate (MHz)
11.0	1.23	-2.63^f	1.235^f	3.5(3)	73(12)	14(3)
14.6	1.29	-2.58(3)	1.25(2)	2.1(3)	52(12)	27(4)
17.9	0.88	-2.57(3)	1.23(2)	-2.8(3)	32(8)	42(5)
20.1	0.94	-2.59(3)	1.24(2)	-18(5)	7(2)	80(30)

Table 4.18: Parameters obtained from fitting the Mössbauer spectra of $CsCo_{1-x}Fe_xCl_3$ using the combined relaxation model of section 3.4 and the program SOEL. The relative area of the soliton subspectrum was fixed to 1/3. The parameters QS, IS, E_2, E_3 and B were constrained to be the same for both subspectra. In these fits, the magnetic hyperfine field B was fixed to the value found from free fits of spectra taken below 4.2 K, namely 24.8 T, and E_3 was fixed to the values shown in table 4.14. ω_0 is the electronic rate parameter and sol rate refers to the soliton relaxation rate. The parameters marked with superscript f were fixed in the fit and the numbers in brackets indicate the uncertainty in the least significant figure(s).

The QS and IS parameters could not be accurately determined from the fits using the 2–level, 3–level or combined relaxation models to the 11.0 K spectrum. For this spectrum QS and IS were constrained to reasonable values. The value of χ^2 increased slightly as a result of this constraint. All other parameters obtained from the fits to the 11.0 K spectrum were not significantly affected by fixing QS and IS to the values shown.

The goodness of fit parameter χ^2 is similar for fits using the 2–level, 3–level and combined relaxation models, indicating that all these models have sufficient parameters to enable the spectra to be fitted well. For the 2–level and 3–level relaxation models the only significantly different parameter is E_2 determined from spectra taken at temperatures above 14.6 K. The energy of state (1) relative to state (2) obtained by using the various relaxation models is plotted in figure 4.17. As expected from the low occupation probability of state (3) below 11 K, at these temperatures the parameter E_2 is the same for fits using the 2–level and 3–level relaxation models. At 1.15 K and 1.9 K the value of E_2 is smaller than its value for temperatures above 4.2 K. This anomalous behaviour was also observed in fits to the Mössbauer spectra of $NH_4Co_{1-x}Fe_xCl_3$ at 1.3 K, and is unexplained.

The decrease of E_2 at 8.6 K to 1.7 cm^{-1}, below its value of 3.5 cm^{-1} at 11 K, may be due to the possible presence of solitons at 8.6 K. Good fits to the 8.6 K Mössbauer

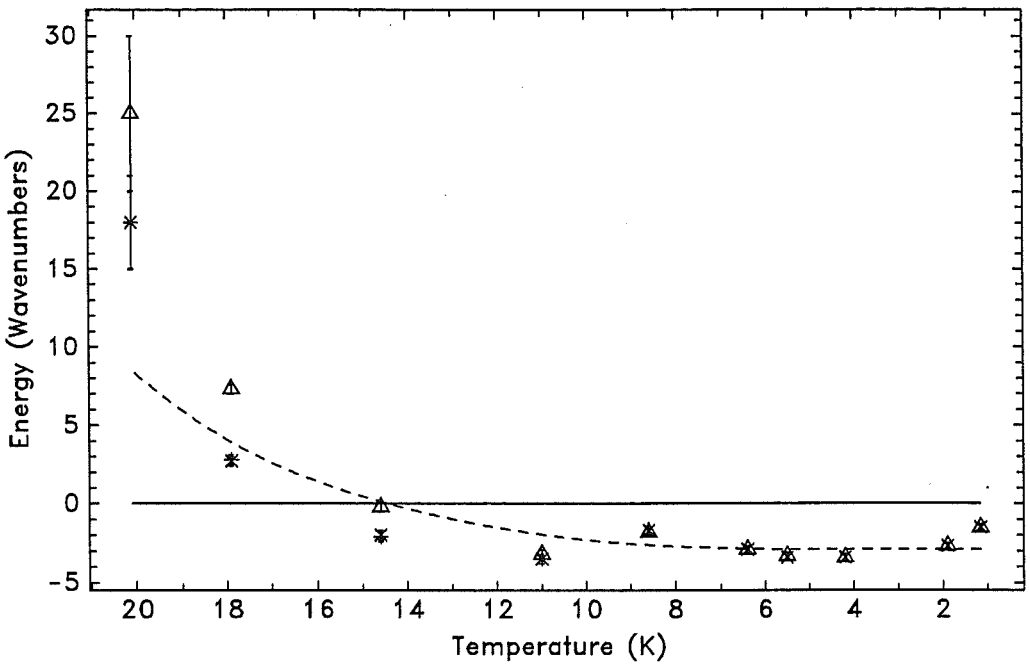

Figure 4.17: The energy of state (1) relative to state (2) (the line at zero energy). The parameter E_2, which is the energy of state (2) minus the energy of state (1), is given by the negative of the energy scale. The dashed curve is the prediction from table 4.9 based on the S=1/2 Brillouin function, the $\triangle$ are from fits using the 2–level model (table 4.10), the $\times$ are from fits using the 3–level model (table 4.11), and the + are from fits using combined relaxation (table 4.12).

spectrum could be obtained using just electronic relaxation as shown in tables 4.16 and 4.17, or using electronic and soliton relaxation subspectra, as for fits performed above 11.0 K. The reported fit to the 8.6 K spectrum is that obtained without soliton relaxation, since the relaxation model with electronic relaxation only is simpler. However, it can be seen that the soliton relaxation subspectra of figure 4.15 increase the absorption in the region of the quadrupole–split absorption lines of non–magnetic $CsCo_{1-x}Fe_xCl_3$. Hence, if a relaxation model with only electronic relaxation is used to fit the 8.6 K spectrum, and if some soliton relaxation was present, then a better fit would be obtained if the occupation probability of the non–magnetic state was allowed to increase. Thus the decrease of E_2 for the 8.6 K spectrum is consistent with the presence of some soliton relaxation at this temperature. Ward *et al* (1987) fitted the 8.6 K spectrum with the relative area of the soliton relaxation subspectrum as a free parameter, and obtain a relative area of the soliton relaxation subspectrum of 10 %, less than the relative area of 1/3 which is expected for the partially disordered

phase.

At temperatures above 14.6 K, the E_2 parameter follows the trend of the prediction in table 4.14 based on the S=1/2 Brillouin function with an effective ordering temperature of 21.2 K. The values of E_2 from fits using the 3–level and combined relaxation models are lower than for fits using the 2–level relaxation model. This effect is more accentuated for $NH_4Co_{1-x}Fe_xCl_3$, and a possible reason for it is discussed on page 88 of section 4.2.2.

The uncertainty of E_2 determined from the 20.1 K Mössbauer spectrum is very large, due to the lack of structure of this spectrum. The large negative value of E_2 at this temperature may not be significant.

The electronic relaxation rate parameter ω_0 obtained from fits using the 3–level relaxation model and the program THREL shows great variability compared to the values of ω_0 obtained from $NH_4Co_{1-x}Fe_xCl_3$. Disregarding the "anomalous" 1.19 K and the unreliable 20.1 K values of ω_0 still leaves a variation in the value of ω_0 of more than a factor of 3 for $CsCo_{1-x}Fe_xCl_3$. The source of this variability may be the poor signal to noise ratio of the Mössbauer spectra of $CsCo_{1-x}Fe_xCl_3$. For noisy spectra χ^2 is inherently insensitive to the precise value of ω_0, since changing the value of ω_0 by a factor of ≈ 2 results mainly in changing the linewidths, which are more difficult to determine from a noisy spectrum than the positions of the absorption lines. The 5.5, 6.4, and 11.0 K spectra in particular are of very poor quality, with a signal to noise ratio for the deepest lines of approximately 2.3, 3.2, and 3.4 respectively, compared to a ratio greater than 4.5 for the other spectra of $CsCo_{1-x}Fe_xCl_3$ taken below T_{N_1}. Other causes of the deviation from constant ω_0 could be due either to error in the values of E_2 or E_3, or to a contribution to the electronic relaxation rate other than the direct process.

The values of ω_0 obtained from fits using the combined relaxation model are the same as those obtained from fits using the 3–level relaxation model.

For all the relaxation models, the spectra taken at temperatures below 8.6 K could be fitted equally well with purely electronic relaxation, or with an additional soliton relaxation subspectrum of relative area 1/3. The spectra at temperatures above 11.0 K could not be fitted with just one electronic relaxation site, and an additional site with a reversing field was necessary to enable satisfactory fits.

The soliton relaxation rates obtained from fits for the various models are shown

in figure 4.18. The solid line is a line of best fit to the soliton relaxation rates

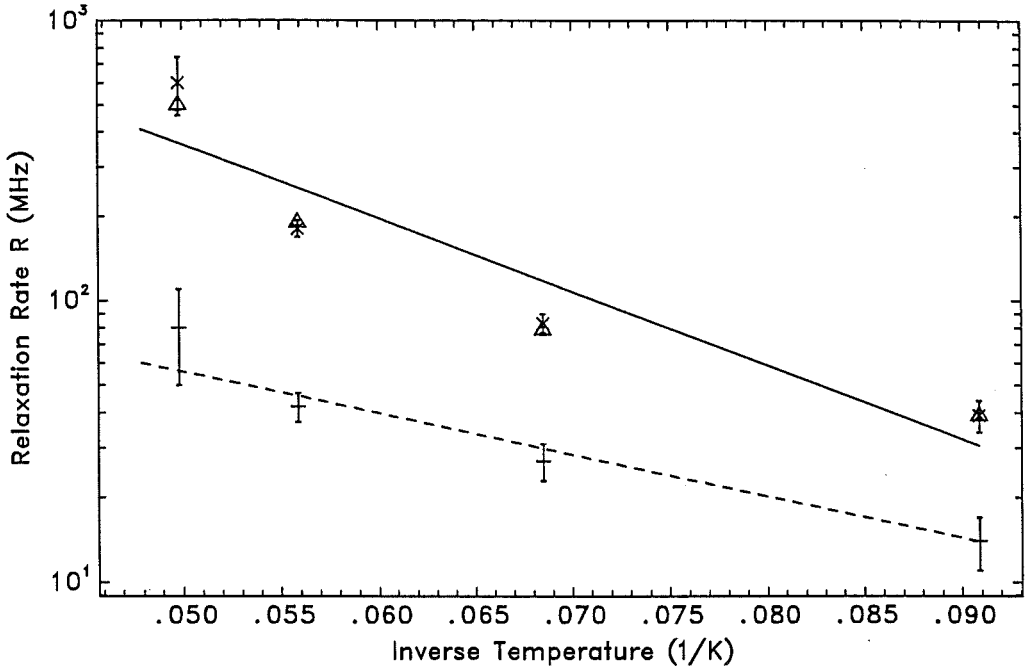

Figure 4.18: The soliton relaxation rates obtained from fits using the 2–level (△), 3–level (×), and combined (+) relaxation models. The solid line is a line of best fit to the soliton relaxation rates obtained from the 2 and 3–level relaxation models and the dashed line is a line of best fit for the relaxation rate obtained from the combined relaxation model.

determined from fits to the Mössbauer spectra of $CsCo_{1-x}Fe_xCl_3$ using the 2–level and 3–level relaxation models, and is given by the equation

$$R = (2.3 \pm 0.6) \times 10^4 \exp\left(\frac{-(70 \pm 20)}{T}\right)$$

where the soliton relaxation rate R is in MHz, and the temperature T is in K.

The dashed line is a line of best fit to the soliton relaxation rate obtained from fits for the combined relaxation model. Its equation is

$$R = (300 \pm 100) \exp\left(\frac{-(34 \pm 8)}{T}\right) .$$

The calculated relaxation rate based on the theory of an ideal soliton–gas (equation (4.1)) with J=75 K and ε=0.12 is well approximated by

$$R = 2.51 \times 10^6 \exp\left(\frac{-68.8}{T}\right) .$$

The predicted relaxation rate for an ideal soliton–gas is at least a factor of 100 faster than the rates determined in this experiment. The soliton relaxation rates obtained from fits using the combined relaxation model are much slower than the rates obtained from the 2–level and 3–level relaxation model fits. The cause of this slower soliton relaxation rate is expected to be the same as that discussed for $NH_4Co_{1-x}Fe_xCl_3$ in section 4.2.2 on page 92.

The soliton relaxation rates in $CsCoCl_3$ obtained from NIS (Boucher *et al* 1985), ^{133}Cs NMR and μ^+ spin resonance (Mekata 1990) fall in the range 10^3 to 2×10^4 MHz at 20 K. These results lie between the relaxation rates found in this experiment (80 to 600 MHz at 20 K) and the predictions of the ideal soliton–gas theory (8×10^4 MHz at 20 K). A comparison of these relaxation rates provides evidence that the ideal soliton–gas predicts a soliton relaxation rate which is too high. The relaxation rate obtained from the Mössbauer spectra of $CsCo_{1-x}Fe_xCl_3$ is lower than that found using the other experimental techniques, due to a combination of either the soliton relaxation rate in $CsCo_{1-x}Fe_xCl_3$ being lower than it is in $CsCoCl_3$, or to fits to the Mössbauer spectra of $CsCo_{1-x}Fe_xCl_3$ not giving the soliton relaxation rate (the product of the soliton density and the mean soliton velocity), as discussed for $NH_4Co_{1-x}Fe_xCl_3$ in section 4.2.2 on page 94.

To summarise, good fits to the Mössbauer spectra of $CsCo_{1-x}Fe_xCl_3$ taken below 21.2 K could be obtained using any of the three relaxation models. It was necessary to include a "soliton" relaxation subspectrum in order to fit the spectra taken at 11.0 K and above. The measured soliton relaxation rates were 2 to 3 orders of magnitude slower than the theoretical prediction of the ideal soliton–gas. The approximation of the 2–level and 3–level relaxation models that the soliton relaxation dominates the electronic relaxation in the frustrated chains is seen to be poor at 11.0 and 14.6 K (see table 4.16). Although the combined relaxation model avoids this approximation, the soliton relaxation rate obtained is even slower.

At temperatures below 8.6 K, the Mössbauer spectra could be fitted with or without a soliton relaxation subspectrum. Above 11 K good fits could only be obtained if 2 subspectra were included; one subspectrum with electronic relaxation only, and the other including soliton relaxation.

The Mössbauer spectra of $NH_4Co_{1-x}Fe_xCl_3$, with better signal to noise ratios, and a larger temperature range for the partially disordered phase, provide a more

stringent test of the various relaxation models than do the Mössbauer spectra of $CsCo_{1-x}Fe_xCl_3$. Both series of spectra show remarkably similar results.

The "extra lines" observed in spectra of $NH_4Co_{1-x}Fe_xCl_3$ below 10 K were not observed in those of $CsCo_{1-x}Fe_xCl_3$. The 1.15 K and 1.9 K spectra of $CsCo_{1-x}Fe_xCl_3$ show a similar decrease in the splitting of the two lowest electronic states of Fe^{2+} to that observed in $NH_4Co_{1-x}Fe_xCl_3$.

Although the combined relaxation model allows the Mössbauer spectra of $NH_4Co_{1-x}Fe_xCl_3$ and $CsCo_{1-x}Fe_xCl_3$ to be fitted with consistent parameter values throughout the magnetically ordered temperature range (except at temperatures below 1.9 K), several refinements to the model may be necessary before reliable soliton relaxation rates can be obtained.

- Increasing the "effective ordering temperature" for the $S = 1/2$ Brillouin function in the calculation of the magnetisation of the Co^{2+} chains (equation (3.47)), so that at temperatures above T_{N_1} there are short–range correlations along the chains of Co^{2+} ions, in accord with the broadening of the absorption lines of the Mössbauer spectra of $NH_4Co_{1-x}Fe_xCl_3$ above T_{N_1}. Increasing the "effective ordering temperature" may yield more realistic energy splittings of the 3 lowest energy electronic states of Fe^{2+}, and hence give a more accurate determination of the electronic relaxation rate parameter. These different electronic relaxation rates would in turn affect the soliton relaxation rate obtained. The "effective ordering temperature" for the $S = 1/2$ Brillouin function is unknown, but is probably in the range 30 K to 50 K for $NH_4Co_{1-x}Fe_xCl_3$, and 25 to 50 K for $CsCo_{1-x}Fe_xCl_3$.

- The electronic relaxation rate parameter ω_0 is dependent upon the states involved in the electronic transition. The explicit transition dependence of ω_0 should be calculated and incorporated in the combined relaxation model. Part of this calculation was performed in section 3.3.

- The effect of the passage of a soliton on the electronic transitions in the Fe^{2+} ion should be calculated, according to the theory of section 3.7.

There are difficulties in obtaining the parameters for all three calculations, so none of the above approaches were pursued further.

Chapter 5

Conclusions

In this thesis relaxation models were developed which enabled the determination of soliton and electronic relaxation rates from the Mössbauer spectra of powder absorbers of $CsCo_{1-x}Fe_xCl_3$ and $NH_4Co_{1-x}Fe_xCl_3$. Crystals of $NH_4Co_{1-x}Fe_xCl_3$ and NH_4FeCl_3 were synthesised. The Mössbauer spectra of $NH_4Co_{1-x}Fe_xCl_3$ were analysed as for $CsCo_{1-x}Fe_xCl_3$, whilst those of NH_4FeCl_3 were taken mainly as a check on the effect of doping Fe^{2+} into NH_4CoCl_3.

The Mössbauer spectra of NH_4FeCl_3 show some unusual features. These include the presence of a distribution of magnetic hyperfine fields at up to 6.0 K, well above the Néel temperature of 1.7 K, and the presence of a non–magnetic subspectrum with a relative area of (28±1) % at 1.3 K. The relative area of the non–magnetic subspectrum is inconsistent with partial disorder occurring in NH_4FeCl_3 since if the non–magnetic subspectrum was caused by the disordered chains in a partially disordered phase, the relative area of the non–magnetic subspectrum would be 33 %. The broadening of the absorption lines at temperatures up to 10 K is expected to be due to intra–chain magnetic correlations, as found in the similar crystal $RbFeCl_3$ at temperatures up to 20 K (T_N for $RbFeCl_3$ is 2.55 K).

The 3–level relaxation model was developed by extending the 2–level relaxation model of Ward *et al* (1987) to include the third electronic state of Fe^{2+} in $NH_4Co_{1-x}Fe_xCl_3$ and $CsCo_{1-x}Fe_xCl_3$. The electronic relaxation rates determined from the Mössbauer spectra of $NH_4Co_{1-x}Fe_xCl_3$ and $CsCo_{1-x}Fe_xCl_3$ using the 2–level relaxation model were found to increase with temperature much slower than expected if the electronic relaxation was by the Raman process. Thus it was assumed

that the electronic relaxation evident in the Mössbauer spectra of Fe^{2+} in these salts occurs by the direct orbit–lattice process. This assumption allowed the number of independent electronic relaxation rate parameters in the 3–level relaxation model to be reduced to one.

The combined relaxation model is an extension of the 3–level relaxation model, allowing Mössbauer spectra to be calculated when two relaxation processes (for example soliton and electronic relaxation) occur at the same site. The combined relaxation model was used in fitting $CsCo_{1-x}Fe_xCl_3$ and $NH_4Co_{1-x}Fe_xCl_3$ Mössbauer spectra, where both electronic and soliton relaxation occur at Fe^{2+} sites in the frustrated chains. Comparisons were made between the parameters obtained from fitting the Mössbauer spectra of $CsCo_{1-x}Fe_xCl_3$ and $NH_4Co_{1-x}Fe_xCl_3$ using the 2–level, 3–level and combined relaxation models.

For $NH_4Co_{1-x}Fe_xCl_3$, the absorption lines of the Mössbauer spectra in the paramagnetic temperature regime are increasingly broadened below ≈ 40 K, as they are in the Mössbauer spectra of $CsCo_{1-x}Fe_xCl_3$. The absorption line broadening above T_{N_1} is attributed to intra–chain magnetic correlations. The onset of magnetic splitting in the Mössbauer spectra of $NH_4Co_{1-x}Fe_xCl_3$ occurs at ≈ 27 K, in agreement with T_{N_1} being (27±4) K.

At temperatures above T_{N_1}, the crystal field and spin–orbit parameters of the Fe^{2+} ion were obtained by fitting the temperature variation of the quadrupole splitting. The fitted values of the parameters were similar to those for Fe^{2+} in $CsCo_{1-x}Fe_xCl_3$. With these parameters the electronic energy levels of the Fe^{2+} ion consist of a ground singlet and a low lying doublet, with the next lowest energy states approximately 140 K higher, so that at temperatures less than T_{N_1} the electronic system is very well approximated by only the three lowest energy electronic states.

From fits of the 1.3 K and 2.8 K Mössbauer spectra it was found that the magnetic hyperfine field of the Fe^{2+} ion was parallel to the EFG principal axis, consistent with $NH_4Co_{1-x}Fe_xCl_3$ being an Ising–like system, as is $CsCo_{1-x}Fe_xCl_3$.

Regardless of the relaxation model used, it was necessary to include a soliton relaxation subspectrum in fitting the Mössbauer spectra of $NH_4Co_{1-x}Fe_xCl_3$ taken above 12.5 K. For spectra taken below 10 K, it was not possible to include a soliton relaxation subspectrum in the fit. It was concluded that for $NH_4Co_{1-x}Fe_xCl_3$,

$T_{N_2} = (11 \pm 2)$ K.

The results obtained from fitting the Mössbauer spectra of magnetically ordered $CsCo_{1-x}Fe_xCl_3$ and $NH_4Co_{1-x}Fe_xCl_3$ are similar. Good fits to the Mössbauer spectra were obtained using all the relaxation models over the whole temperature range up to T_{N_1} with constant magnetic hyperfine field. The only significant differences between fits using the different models are described below.

- The values of E_2 obtained from fits for the 2–level relaxation model differ from the values obtained from fits for the 3–level and combined relaxation models. E_2 obtained from fits for the 2–level relaxation model increased to unrealistic values near T_{N_1}. This increase was expected, and is presumably due to occupation of the third energy level. The unrealistic increase of E_2 did not occur in fits for the 3–level and combined relaxation models, which account for the occupation of the third energy level.

- The values of the soliton relaxation rate obtained for fits of the combined relaxation model were less than half those obtained from the 2 and 3–level relaxation model fits.

The soliton relaxation rates obtained in this thesis for $CsCo_{1-x}Fe_xCl_3$ and $NH_4Co_{1-x}Fe_xCl_3$ are generally 2 to 3 orders of magnitude slower than the theoretical prediction based on an ideal soliton–gas for pure $CsCoCl_3$, and the results of the NIS experiment performed by Boucher *et al* (1985). This discrepancy may be due to further inadequacies in the relaxation models used, namely that the electronic relaxation rate is assumed to be independent of which states the relaxation occurs between, and it is assumed that the passage of a soliton always causes a field reversal if a magnetic Fe^{2+} state is occupied. Both these assumptions were examined in this thesis, but computation of the effects was hampered by lack of information about the coupling coefficients and phonon matrix elements of the strain tensor, and difficulties in calculating coefficients of fractional parentage for more than half–filled shells.

Another possibility is that the soliton relaxation rate is slower in $CsCo_{1-x}Fe_xCl_3$ and $NH_4Co_{1-x}Fe_xCl_3$ than in the pure compounds. This possibility could be examined experimentally by performing NIS experiments on the Fe^{2+} doped salts, and comparing the results with those obtained for the pure salts. Further work

on $NH_4Co_{1-x}Fe_xCl_3$ and NH_4CoCl_3 using the techniques of neutron diffraction may yield a more accurate determinations of T_{N_1} and T_{N_2} than were obtained in this work.

In conclusion, 3–level and combined relaxation models were developed enabling the fitting of the Mössbauer spectra of $NH_4Co_{1-x}Fe_xCl_3$ and $CsCo_{1-x}Fe_xCl_3$. Although these models are an improvement over the original 2–level relaxation model, the soliton relaxation rates obtained were 2 to 3 orders of magnitude lower than expected. The assumptions within the 3–level and combined relaxation models were examined. However, quantitative calculations which obviate these assumptions were impossible due to lack of data.

$NH_4Co_{1-x}Fe_xCl_3$ was demonstrated to have similar magnetic properties to $CsCo_{1-x}Fe_xCl_3$, with solitons existing in the partially disordered phase.

Acknowledgements

I would like to thank the following people:

- My supervisor Dr Valda McCann for her professional advice and guidance, as well as the time and energy she has spent on my behalf.
- Dr Quentin Pankhurst of Liverpool University for taking the low temperature Mössbauer spectra.
- Drs Geoff Stedman and Phil Butler for their help and sharing their expertise in the fields of perturbation theory and multi–electron systems.
- Dr Vicki McKee for performing and analysing the X–ray diffraction.
- The technical staff of the Physics and Astronomy Department, in particular C Rowe, R Ritchie, T Walker, R Flygenring, B Bradshaw, W Smith and S Hemmingson for their assistance.
- John Laban, who occupied the desk next to mine, for many discussions and ideas.

References

Abragam A (1961) *The Principles of Nuclear Magnetism.* Oxford University Press, London p.447

Abragam A, Bleaney B (1970) *Electron Paramagnetic Resonance of Transition Ions.* Clarendon Press, Oxford, p.563

Achiwa N (1969) J. Phys. Soc. Japan **27** 561

Adachi K, Hamashima M, Ajiro Y, Mekata M (1979) J. Phys. Soc. Japan **47** 780

Adachi K, Takeda K, Matsubara F, Mekata M, Haseda T (1983) J. Phys. Soc. Japan **52** 2202

Ajiro Y, Kikuchi H, Okita T, Chiba M (1989) J. Phys. Soc. Japan **58** 390

Amit M, Zodkevitz A, Makovsky J (1970) Israel J. of Chem. **8** 737

Asch L, Friedt J M, Lupiani C, Tornero J (1973) Chem. Phys. Lett. **21** 595

Baines J A, Johnson C E, Thomas M F (1983) J. Phys. C **16** 3579

Ballhausen C J, (1962) *Introduction to Ligand Field Theory.* McGraw-Hill, New York, p.103

Blatt J M, Weisskopf V F (1952) *Theoretical Nuclear Physics* Wiley, New York

Blume M (1968) Phys. Rev. **174** 351

Blume M, Orbach R (1962) Phys. Rev. **127** 1587

Blume M, Tjon J A, (1968) Phys. Rev. **165** 446

Bocquet S (1987) PhD thesis, Department of Physics, University of Canterbury.

Boucher J P, Renard J P (1980) Phys. Rev. Let. **45** 486

Boucher J P, Benner H, Devreux F, Regnault L P, Rossat–Mignod J, Dupas C, Renard J P, Bouillot J, Stirling W G (1982) Phys. Rev. Let. **48** 431

Boucher J P, Regnault L P, Rossat–Mignod J, Henry Y, Brouillot J, Stirling W G (1985) Phys. Rev. B **31** 3015

Boucher J P, Regnault L P, Benner H (1987) Springer Series in Solid–State Sciences, Eds. A R Bishop, D K Campbell, P Kumar, and S E Trullinger, Springer–Verlag Berlin, **69** 24

Bradbury M I, Newman D J (1968) Chem. Phys. Lett. **2** 495

Bradbury M I, Newman D J (1971) J. Phys. Chem. Solids **32** 627

Clauser M J, (1971) Phys. Rev. B **3** 3748

Davidson G R, Eibschütz M, Cox D E, Minkiewicz V J (1971) AIP Conf. Proc. **5** 436

Davidson G R, Eibschütz M, Guggenheim H J, (1973) Phys. Rev. B **8** 1864

Dirac P A M (1929) Proc. Roy. Soc. **A123** 714

Dunlap B D, Shenoy G K (1976) Phys. Rev. B **13** 18

Eibschütz M, Davidson G R, Cox D E (1973) AIP Conf. Proc. number 18, 386

Eibschütz M, Lines M E, Sherwood R C (1975) Phys. Rev. B **11** 4595

Elmassalami M, Smit H H A, Thiel R C, de Jongh L J (1989) Physica B **154** 267

Euler W B, Garrett B B (1981) J. Phys. Chem. Solids **42** 7

Euler W B, Long C, Moulton W G, Garrett B B (1978) J. Mag. Res. **32** 33

Fraleigh J B, (1967) *A First Course in Abstract Algebra.* Addison-Wesley, Reading, Massachusetts, p.106

Freeman A J, Watson R E (1963) Phys. Rev. **131** 2566

Grandjean F (1988) *The Time Domain in Surface and Structural Dynamics.* ed G.J. Long and F. Grandjean, Kluwer Academic Publishers, p.287

Greenwood N N, Gibb T C (1971) *Mössbauer Spectroscopy,* Chapman and Hall Ltd, London, p.74

Handbook of Chemistry and Physics (1990), CRC Press, Inc.

Harrison A (1993) Private communication.

Harrison A, Stager C V, Visser D (1991) J. Appl. Phys. **69** 5998

Harrison A, Visser D (1989) Phys. Let. **137A** 79

Harrison A, Visser D (1992) J. Phys.: Condens. matter **4** 6977

Iio K, Hyodo H, Nagata K (1980) J. Phys. Soc. Japan **49** 1336

Ingalls R L (1971) *An Introduction to Mössbauer Spectrocopy,* ed L. May, Plenum Press, New York, p.109

Ingalls R (1977) Phys. Rev. B **133** 189

Jackson J D (1969) *Classical Electrodynamics*, Wiley, New York

Johnson C E (1984) *Mössbauer Spectroscopy Applied to Inorganic Chemistry*, Ed. G J Long, Plenum Publishing Corporation, **1** 619

Kittel C (1976) *Introduction to Solid State Physics,* Wiley and Sons inc., New York, p.438

Kjems J K, Steiner M (1978) Phys. Rev Let. **41** 1137

Laban J A (1994) Ph.D. thesis, University of Canterbury, in preparation

Lamb W E (1939) Phys. Rev. **55** 190

Levy P M (1969) Phys. Rev. **177** 509

Lehmann W P, Breitling W, Weber R (1981) **14** 4655

Lines M E (1974) Phys. Rev. B **9** 3927

Lines M E, Eibschütz M (1975) Phys. Rev. B **11** 4583

Lockwood D J, Johnstone I W, Labbe H J, Briat B (1983) J. Phys. C: Solid State Phys. **16** 6451

Long G J, Cranshaw T E, Longworth G (1983) Mössbauer Effect Data Reference Journal **6** 42

Matsubara F (1982) J. Phys. Soc. Japan **51** 2424

McCann V H, Laban J A, Sheen N I (1992) Hyperfine. int. **71** 1363

Mekata M (1990) J. Magn. Magn. Mat. **90 & 91** 247

Mekata M, Adachi K (1978) J. Phys. Soc. Japan **44** 806

Mekata M, Tatsumi T, Nakashima T, Adachi K, Ajiro Y (1987) J. Phys. Soc. Japan **56** 4544

Melamud M, Pinto H, Makovsky J, Shaked H (1974) Phys. Status Solidi B **63** 699

Merzbacher E (1970) *Quantum Mechanics.* John Wiley and sons, New York, p.450

Mikeska H J (1978) J. Phys. C: Solid St. Phys. **11** L29

Mikeska H J (1980) J. Phys. C: Solid St. Phys. **13** 2913

Montano P A, Shechter H, Cohen I, Makovsky J (9174) Phys. Rev. B **9** 1066

Mössbauer Effect Data Index (1976) Eds. Stevens J G, Stevens V E IFI–plenum, New York

Nagler S E, Buyers W J L, Armstrong R L, Briat B (1983) Phys. Rev. B **27** 1784

Nielson C W, Koster G F (1963) *Spectroscopic Coefficients for the p^n, d^n, and f^n Configurations.* The M.I.T. Press, Cambridge, Massachusetts

Ohta H, Imagawa S, Motokawa M, Ikeda H (1993) J. Phys. Soc. Japan **62** 2481

Orbach R (1961) Proc. R. Soc. London **A 264** 458

Petitgrand D, Hennion B (1981) Physica **107B** 75

Pollard R J, McCann V H, Ward J B (1982) J. Phys. C **15** 6807

Price D C (1978) Aust. J. Phys. **31** 397

Putnik C F, Cole G M, Garrett B B, Holt S L (1976) Inorg. Chem. **15** 826

Rotenberg M, Bivins R, Metropolis N, Wooten J K jr (1959) *The 3-j and 6-j Symbols.* The Technology Press, Massachusetts Institute of Technology

Sheen N I, McCann V H, Pankhurst Q A (1994) To be published in Hyperfine Interactions.

Shiba H (1980) Prog. Theor. Phys. **64** 466

Shiba H (1982) Solid State Comm. **41** 511

Sidgewick N V (1950) *The Chemical Elements and Their Compounds.* Clarendon Press, Oxford II 1327

Singwi K S, Sjolander A (1960) Phys. Rev. **120** 1093

Smit H H A, de Groot H J M, Elmassalami M, Thiel R C, de Jongh L J (1989) Physica B **154** 237

Snodgrass W A (1993) Undergraduate Project Report, Physics and Astronomy Department, University of Canterbury.

Soling H (1968) Acta Chem. Scand. **22** 2793

Stedman G E, Newman D J (1971) J. Phys. C **4** 884

Steiner P, Gerdau E, Hautsch W, Steenken D (1968) *Hyperfine Structure and Nuclear Radiations*, Eds. E. Matthias and D.A. Shirley, North Holland Publishing Company, Amsterdam, p.364

Sugano S, Tanabe Y, Kamimura H (1970) *Multiplets of Transition Metal Ions in Crystals.* Academic Press, New York

Suzuki N (1978) J. Phys. Soc. Japan **45** 1791

Suzuki N (1983) J. Phys. Soc. Japan **52** 1002

Swanson H E, McMurdie H F, Morris M C, Evans E H (1968) U. S. Nat. Bur. Stand., monogr 25, section 6, p.5

Tellenbach U (1978) J. Phys. C: Solid State Phys. **11** 2287

Trees R E (1951) Phys. Rev. **82** 683

Villain J (1975) Physica **79** 1

Visser D, Harrison A (1992) J. magn. magn. mater. **116** 80

Wada N, Ubokoshi K, Hirakawa K (1982) J. Phys. Soc. Japan **9** 2833

Ward J B, McCann V H, Pankhurst Q A, Hasset W L, Price D C (1987) J. Phys. C **20** 1689

Watson R E, Freeman A J (1963) Phys. Rev. **131** 250

Weissbluth M (1978) *Atoms and Molecules.* Academic Press, New York

Wertheim G K (1964) *Mössbauer Effect: Principles and Applications.* Academic Press, New York, p.70

Witteveen H T, van Veen J A R (1973) J. Chem. Phys. **58** 186

Woodgate G K (1970) *Elementary Atomic Structure.* McGraw-Hill, London, p.73

Yoshizawa H, Hirakawa K, (1979) J. Phys. Soc. Japan **46** 448

Yoshizawa H, Hirakawa K, Satija S K, Shirane G (1981) Phys. Rev. B **23** 2298